Title
Complementary 4D-Flow and CFD Analysis Methods for Investigating Pathological Hemodynamics

Author
Kao, Evan I-Tai

Publication Date
2017

Peer reviewed|Thesis/dissertation

Complementary 4D-Flow and CFD Analysis Methods for Investigating Pathological Hemodynamics

by

Evan I Kao

A dissertation submitted in partial satisfaction of the requirements for the degree of

Joint Doctor of Philosophy

with University of California, San Francisco

in

Bioengineering

in the

Graduate Division

of the

University of California, Berkeley

Committee in charge:

Professor David Saloner, Chair

Professor Mohammad Mofrad

Professor Per-Olof Persson

Summer 2017

Abstract

Complementary 4D-Flow MR and CFD Analysis Methods for Investigating Pathological Hemodynamics

by

Evan I Kao

Joint Doctor of Philosophy in Bioengineering

University of California, Berkeley

Unviersity of California, San Francisco

Professor David Saloner, Chair

The pathology of many cardiovascular diseases is believed to be heavily tied to local hemodynamics. A positive feedback loop of remodeling and unhealthy flow conditions can lead to blood vessel abnormalities, such as aneurysms, stenoses, and plaques. Doctors use medical imaging techniques to visualize vascular disease within patients. However, while treatments based on these images for some diseases have been well-established, there is room for improvement. Many treatment decisions are based on simplified criteria and incomplete data, and our understanding behind the pathophysiology of many of these diseases remains woefully incomplete. A stronger grasp of the relationship between disease and hemodynamics can help clinicians plan better treatment outcomes or help prevent some complications from occurring.

4D-Magnetic Resonance (MR) Imaging can be a powerful tool for quantifying the flow field within the cardiovasculature, but remains difficult to integrate for clinical use due to the involving process required to convert noisy magnetic resonance image data from a set of symbols to an easily digestible image. Treatment decisions are based on standardized practices, but no standardization for the processing and interpretation of 4D-MR images exist. Computational Fluid Dynamics (CFD) can simulate patient hemodynamics with much finer temporal and spatial resolution than 4D-MR. However, computational methods must still use boundary conditions obtained from imaging data, which means CFD results can only be as accurate as the images they are based upon. Additionally, the logistics of performing CFD, which require extensive training and time, is a strong barrier against its adoption in a clinical setting.

This thesis presents a model for using *in vivo* (live) and simulated flow data as complementary methods to explore potential mechanisms of pathophysiology and aid the treatment of cardiovascular diseases. We developed pipelines for processing 4D-MR images and for building patient-specific CFD simulations. We first attempted to measure the experimental error in 4D-Flow MRI within a cerebral aneurysm phantom and explored how that error might propagate into CFD results based on those MR measurements. We used those results to predict how this sensitivity would affect the treatment of aneurysms based on their hemodynamics. We then used both 4D-MR and CFD methods to characterize a rarely explored vascular territory, the cerebral venous outflow tract (CVOT). 4D-Flow MR was used to categorize geometries and flows in the CVOT. CFD was used to investigate a potential association between flow and symptoms in a subcategory of internal jugular vein geometries.

Contents

List of Figures

List of Tables

Chapter 1

Introduction

The pathology of many cardiovascular diseases is believed to be heavily tied to local hemodynamics. A positive feedback loop of remodeling and unhealthy flow conditions can lead to blood vessel abnormalities, such as aneurysms, stenoses, and plaques. Doctors use medical imaging techniques to visualize vascular disease within patients. However, while treatments based on these images for some diseases have been well-established, there is room for improvement. Many treatment decisions are based on simplified criteria and incomplete data and our understanding behind the pathophysiology of many of these diseases remain woefully incomplete. A stronger grasp of the relationship between disease and hemodynamics can help clinicians plan better treatment outcomes or help prevent some complications from occurring.

This thesis presents a model for using *in vivo* (live) and simulated flow data as complementary methods to explore potential mechanisms of pathophysiology and aid the treatment of cardiovascular diseases. We limit our scope specifically to analyses derived from Magnetic Resonance (MR) images and focus on a rarely explored vascular neighborhood: The Cerebral Venous Outflow Tract (CVOT). We also test these flow analysis methods on a phantom of a cerebral aneurysm, an abnormality found in the Circle of Willis (COW). This chapter presents a brief overview of these vasculatures as well as the relevant imaging modalities and simulation methods.

1.1 Physiology

1.1.1 Cerebral Anerusysms

Cerebral aneurysms or intracranial aneurysms (IA) are pathological distensions of blood vessel arising within the cerebral arterial vasculature, often in the Circle of Willis, the major blood circuit within the brain (Figure 1.1). These distensions occur due to a weakening of the vessel wall. A healthy vessel wall consists of 3 layers: intima, media, and adventitia (Figure 1.2), but the aneurysm wall lacks the media, which contains smooth muscle cells. This loss of structural integrity can eventually lead to rupture and subsequent bleeding into the surrounding brain space (subarachnoid hemorrhage), which results in stroke, brain damage, or death.

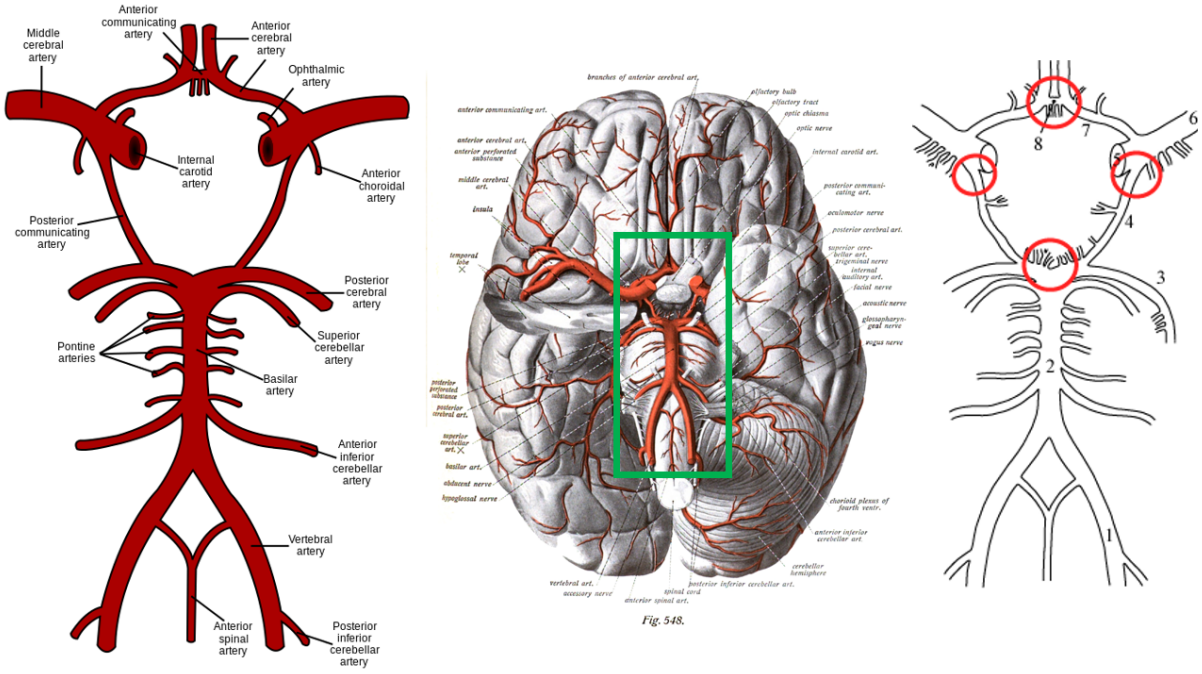

Figure 1.1: Images depiciting the Circle of Willis, where most intracranial aneuryms develop. (*Left*) The overall Circle of Willis. (*Middle*) The location of the COW in relation to the brain. (*Right*) The location of most IA appearances.

The two major types of cerebral aneurysms are *saccular* or *fusiform* (Figure 1.3). Saccular aneurysms, which make up about 80-90% of all aneurysms, involve distensions along only a portion of the vessel wall, which results in a pouch or a sac. Fusiform aneurysms involve distension all around the vessel.

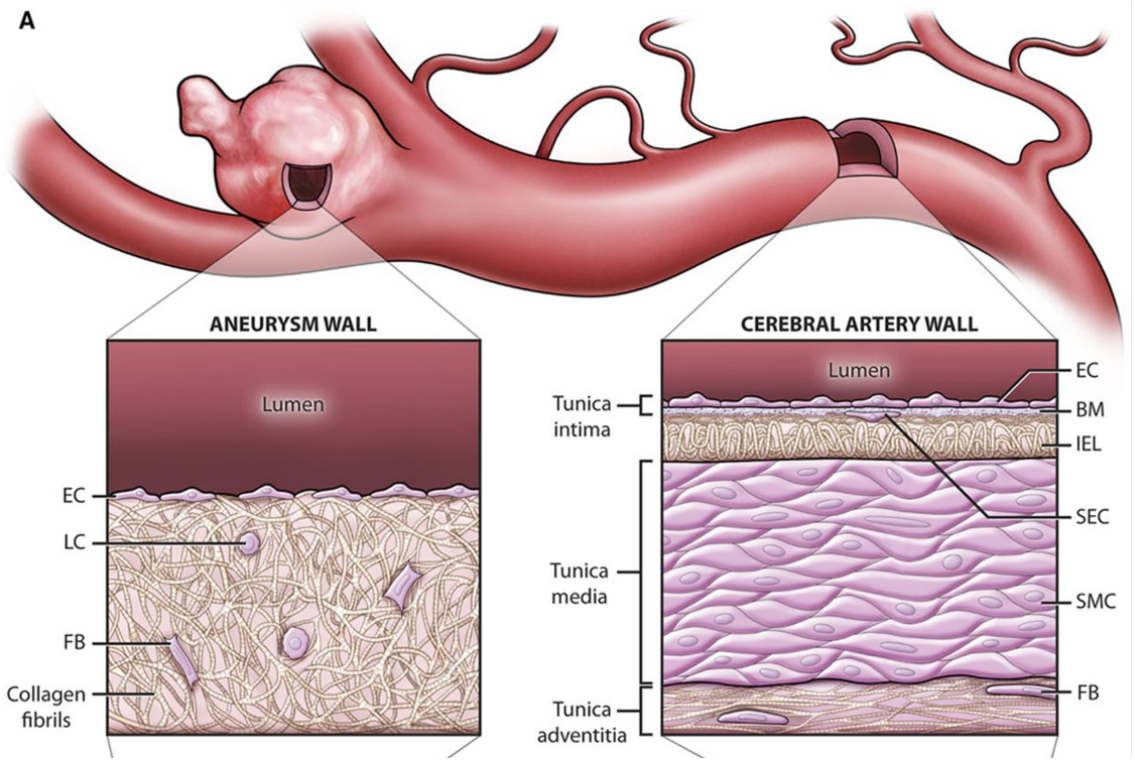

Figure 1.2: Differences in the wall structure between a cerebral artery and cerebral aneurysm. Reprinted from Etminan et al. 2014 [1] with permission from Wolters Kluwer Health, Inc..

Two prominent correlators of rupture are aneurysm size and growth. Morita et al. 2012 found that the rupture rate for aneurysms increased nonlinearly with diameter (0.36% for 3-4mm vs. 4.37% for 10-24mm and 33% for >25mm) [3]. Villablanca et al. 2013 determined that rupture rate for growing aneurysms was 12 times greater than that of stable aneurysms (2.4% vs. 0.2%) [4].

Clinically, the decision to perform surgery usually depends only on the aneurysm diameter measured by a two-dimensional projection of an angiogram. The drawbacks behind this approach include the fact that the anerysms are not perfectly spherical and that the projection may not fully capture the aneurysm's geometry, which can lead to incorrect assessments of aneurym size. Because treatment options carry a mortality risk that ranges from 1 to 10% [5][6][7], these uncertainties are problematic. Treatment decisions may be improved if we can find better correlators with growth or rupture than projected aneurysm diameter. This provides the impetus to use 4D flow and CFD methods to measure or estimate these correlators and predict risk on a patient-specific basis.

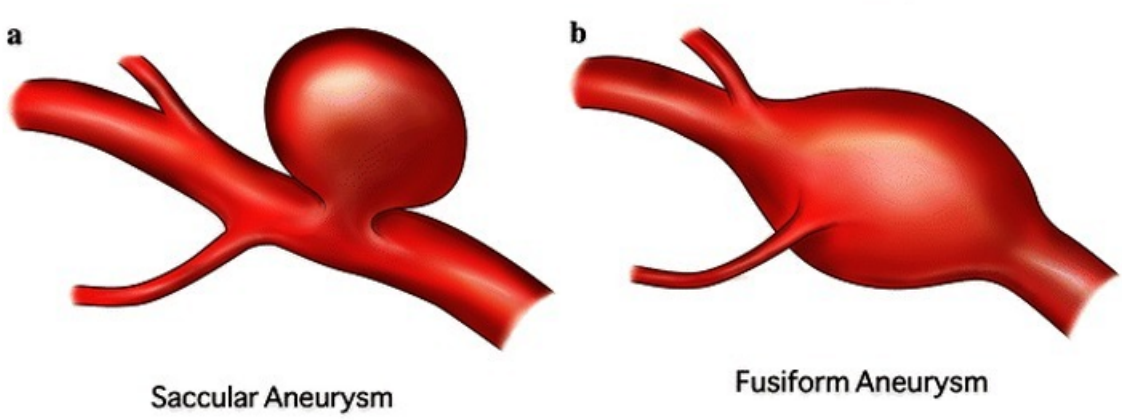

Figure 1.3: Saccular vs fusiform aneurysms. Source: Withers et al. 2013 [2]

1.1.2 Cerebral Venous Outflow Tract

The CVOT is a portion of venous cerebral vasculature draining deoxygenated blood from the brain. It consists of the sigmoid sinus (SS) and the internal jugular vein (IJV) (Figure 1.4). The junction between the SS and IJV has a dilated caliber and is labeled the jugular bulb (JB). Unlike the intracranial arterial anatomy, the cerebral venous vasculature, including the CVOT, is highly variable. Geometric abnormalities in the CVOT have been suggested to be related to a few symptoms or diseases, but no concrete link has been established. This is partially due to the many different types of vascular geometries found in the CVOT.

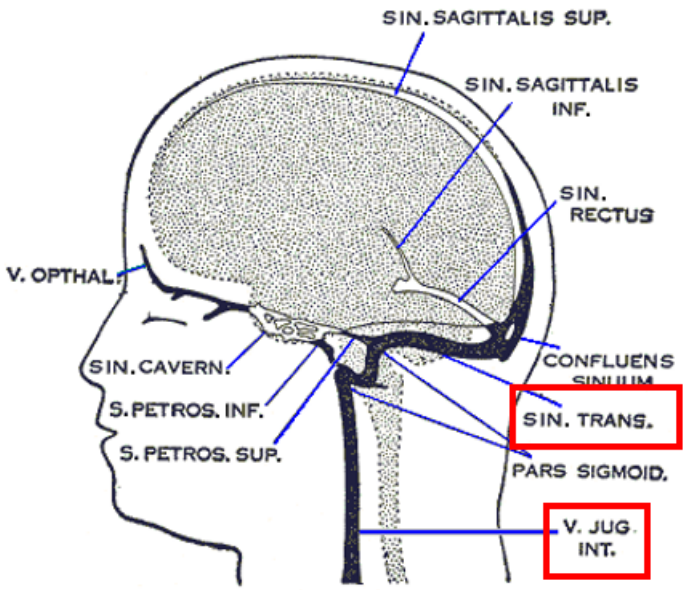

Figure 1.4: Diagram of the CVOT, with the most relevant structures boxed in red.

1.2 Relevant Medical Imaging Modalities for 4D Flow analysis and CFD

In this section, we review the most relevant imaging modalities for 4D-MR based flow analysis and CFD in this thesis: Contrast-Enhanced Magnetic Resonance Angiography (CE-MRA), for geometric visualization; 2D Phase-Contrast MRI (2D-PC MRI), for extracting flow time-profiles; and 4D Phase-Contrast MRI (4D-PC MRI), for obtaining the full velocity field over time.

1.2.1 Contrast-Enhanced MR Angiography

CE-MRA visualizes blood vessels with the aid of a contrast agent that enhances the magnetization signal within the blood (Figure 1.5). CE-MRA provides a reasonable image resolution (about 0.7 x 0.7 x 0.7 mm) but carries no temporal information; the geometry is a composite over the cardiac cycle. Because the diastolic phase (heart-filling, low pressure) dominates the cardiac cycle, geometries obtained by CE-MRA may be assumed to be the diastolic (least-distended) state. This distinction matters less for the cerebral vasculature, where vessel distension is limited by the surrounding

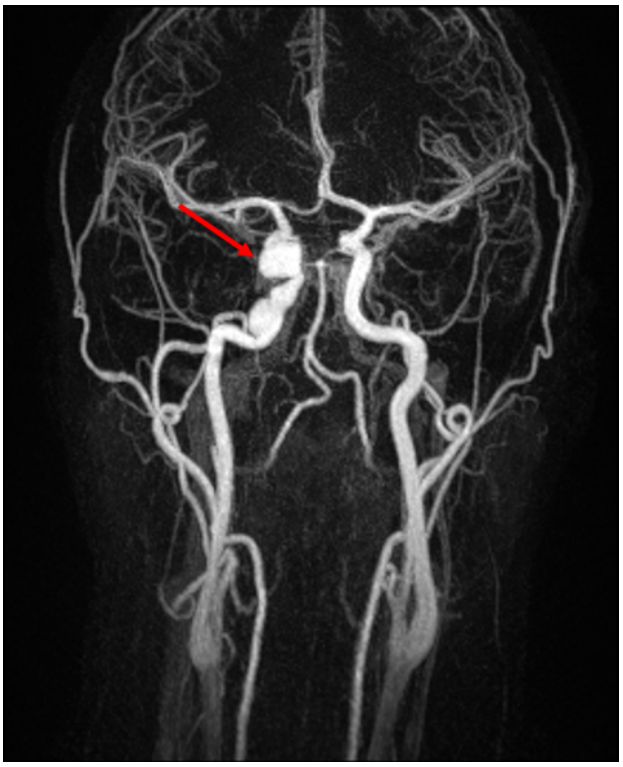

Figure 1.5: Example of a maximum intensity projection (MIP) from a 3D CE-MRA image of a cerebral aneurysm (Red Arrow).

brain tissue. However, the geometric difference between systole (high-pressure) and diastole may be an issue in other vascular systems and complicates the analysis.

1.2.2 2D cine PC-MRI

Phase-Contrast MRI is an imaging technique that enables us to measure velocities (Figure 1.6). Essentially, an atom's response to a medical scanner's magnetic field and applied radio-frequency pulses is quantified by its *phase-shift*, which is proportional to its velocity. For 2D cine PC-MRI, an imaging plane is selected and the velocity component normal to the plane is measured. For the most relevant results, the imaging plane should be placed orthogonal to the blood vessel of interest. Velocity measurements may be compromised by experimental sources of error, including partial voluming effects (when a voxel contains molecules from both the stationary vessel wall or air and the moving blood) and intravoxel phase dispersion (when a voxel contains molecules with varying velocity magnitudes and directions, such as during turbulent flow, which usually manifests as a reduced signal).

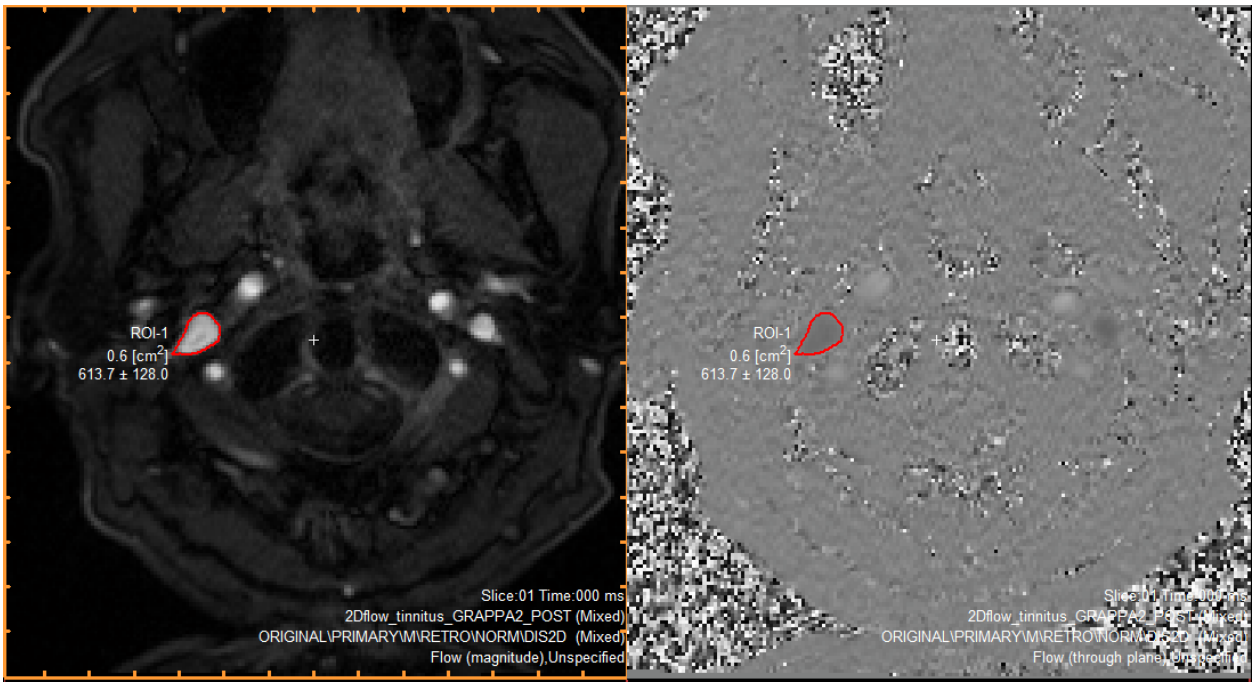

Figure 1.6: A representation of the magnitude (Left) and phase (Right) images from a 2D PC-MR velocimetry aquisition as depicted in the flow quantification software Segment. The cross-section of one vessel of interest is outlined in red. The magnitude provides a reference for the anatomy, while the phase encodes the velocity. Flow and other parameters can be calculated from this region of interest.

1.2.3 4D PC-MRI

As its name suggests, 4D-MR provides velocity data over time in a volume of interest (Figure 1.7). The obvious advantage of 4D-MR over 2D PC-MR is a much greater field of coverage, which allows one to measure flows without being limited to a plane. However, this comes at the cost of much longer acquisition times, which must be balanced against patient tolerance.

Recording the full 3D-vector field over time allows us to visualize secondary flow patterns that cannot be represented in 2D. This overcomes the intravoxel phase dispersion errors, though 4D-MR data is still subject to partial voluming effects (explored in more detail in Chapter 3).

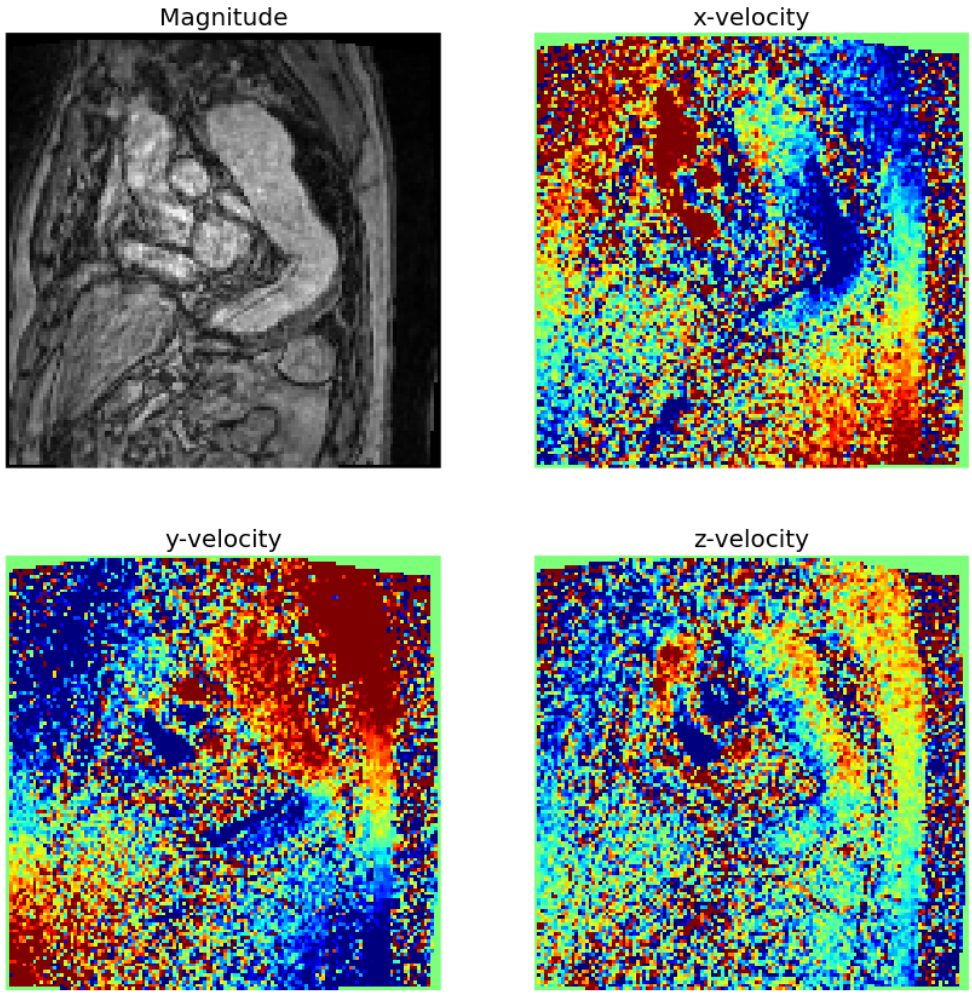

Figure 1.7: A representation of the information provided by a 4D-MR acquisition for a single image slice at a single time point. As with 2D-MR, the magnitude provides a reference anatomy, while each phase image encodes one of the three orthogonal velocity directions.

1.3 Previous Work

1.3.1 Role of 4D-Flow in Medicine and Research

4D-MR can be a powerful tool for quantifying the flow field within the cardiovasculature, but remains difficult to integrate for clinical use due to the involving process required to convert noisy MR image data from a set of symbols to an easily-digestible image. Recently, commercial software has been developed to simplify the process, but they are still in their developmental stages and their licenses are expensive. Additionally, even given a set of clear flow images, we have yet to bridge the gap between the wealth of 4D-flow images from patients and actual use of those images in clinical practice. Treatment decisions are based on standardized practices, but no standardization for the processing and interpretation of 4D-MR images exist.

1.3.1.1 Flow patterns and disease

Currently, groups are investigating the link between flow patterns and disease in various vascular territories. Frydrychowicz et al. 2007 looked at the flow patterns in healthy and diseased thoracic aorta [8]. Sigovan et al. 2011 posited that flow eccentricity could be a marker for aortic valve disease [9]. Bolger et al. 2007 used 4D-Flow to compare intraventricular flow in healthy and diseased hearts [10].

As an extension of these efforts, we applied a similar analysis to jugular veins (Chapter 4).

1.3.1.2 Advanced hemodynamical metrics

Recently there have been ambitious attempts to extract advanced hemodynamical information directly from experimentally-measured flow, such as wall-shear stress (WSS) and turbulence. Multiple groups have tried their hand at measuring WSS *in vivo* directly from 4D-MR data [11][12][13][14]. However, Boussel et al. 2009 compared their 4D-MR-derived WSS and maximum shear stress (MSS) results to CFD results in patient cerebral aneurysms and concluded that the 4D-Flow measurements were inaccurate [15]. A similar study was performed by Petersson et al. 2012, which compared MRI-derived WSS with numerical simulations of blood flow in a simple phantom [16]. They concluded that the current realistic resolution of 4D-MR made it impossible to capture high WSS, though low and medium areas of WSS could possibly be distinguishable.

Other parameters currently under investigation include Pulse Wave Velocity (which characterize the stiffness of a blood vessel) [17], turbulent kinetic energy [18], and pressure field extraction [19].

1.3.2 Role of CFD in Medicine

To complement information obtained from blood flow quantification, we use computational fluid dynamics (CFD). CFD is a set of numerical methods used to solve the Navier-Stokes equations, which describe fluid flow. CFD allows us to quantify the flow field in much greater spatial and temporal resolution without noise, which provides more reliable calculations of derivative values like gradients or shear stress that would otherwise be difficult or impossible to calculate using MR. However, computational methods must still use boundary conditions obtained from imaging data, which means CFD results can only be as accurate as the images they are based upon. The sensitivity of the CFD results to its boundary conditions is still under investigation within the field. Additionally, the logistics of performing CFD, which require extensive training and time, is a strong barrier against its adoption in a clinical setting.

1.3.2.1 CFD applied to cerebral aneurysms

CFD studies have attempted to elucidate the connection between IA growth and WSS. However, even now the results remain inconclusive or conflicting. Boussel et al. 2008 performed patient-specific CFD simulations for 7 human subjects and determined a correlation between low WSS and aneurysm dome growth [20]. This corresponded with a study by Jou et al. 2008, which correlated low WSS and aneurysm rupture in 26 patients [21]. On the other hand, Castro et al. 2009 did a similar analysis on 26 aneurysms and found a correlation between high WSS and rupture [22].

Mut et al. 2011 proposed several flow-related metrics for assessing IA health, such as volumetric kinetic energy, viscous dissipation, and vorticity, in addition to previously-established metrics such as WSS, wall shear stress gradient (WSSG), and oscillatory shear index (OSI), but it remains to be seen how these metrics are clincially relevant [23].

1.3.2.2 CFD applied to CVOT

In contrast to cerebral aneurysms, few CFD simulations have been applied to venous vasculatures, much less the CVOT specifically. In fact, only one recent study

attempted to investigate the relationship between the sigmoid sinus and intracranial hypertension [24]. Hence, there is clear need for additional experimental and computational studies.

1.4 Objectives and Overview of Thesis

Our objective in this thesis is to build a pipeline for complementary 4D-MR and CFD analysis and to apply them to relevant questions in cardiovascular disease in ways that could not be addressed by either 4D-MR or CFD alone; this pipeline is explained in detail in Chapter 2. We first attempted to measure the experimental error in 4D-Flow MRI and explored how that error might propagate into CFD results based on those MR measurements (Chapter 3). We then used 4D-Flow MR to categorize geometries and flows in the CVOT (Chapter 4), and then finally used CFD to investigate a potential association between flow and symptoms in a subcategory of internal jugular vein geometries (Chapter 5).

Chapter 2

Methods

This chapter details the major steps in obtaining and processing MR imaging and simulation data, which are referenced in later chapters.

2.1 Image Processing

2.1.1 Extracting Velocity from Image Data

Imaging data in general is stored in the Digital Imaging and Communications in Medicine (DICOM) format. In order to facilitate the storage and transfer of medical imaging data, the DICOM standard specifies that contextual information (e.g., patient name, acquisition-type, orientation) are stored together as headers with the raw pixel or voxel data (unfortunately what information is stored in each header attribute is not standardized between vendors).

In MR imaging, signal is generated by a magnetization vector and data is aquired as complex numbers with a real and imaginary component. This can then be reconstructured as the magnitude and phase of the vector. Flow quantification sequences, like 2D-MR or 4D-MR, store data as both magnitude and phase. The magnitude data provides an image of the anatomy; it does not provide any meaningful information about the velocity magnitude. With the correct design of the MR flow sequence, the phase data encodes the individual components of the velocity of the blood and tissue (though often tissue movement is negligible relative to blood), which is stored as a matrix of positive integers. Using information from the DICOM headers, these values are then converted to phase values ($\phi \in [-\pi, \pi]$), which in turn are converted into velocity units using the following equation:

$$\text{Velocity} = \text{Phase} * \frac{\text{Venc}}{\pi} \tag{2.1}$$

where Venc (colloquially pronounced "Venk") is the **encoding velocity**. The Venc, which is determined by adjusting the strength of the magnetic field gradients, is set by the MR scanner operator and stored within the DICOM headers during acquisition. The choice of Venc plays an important role in balancing image detail with processing workload. As can be inferred from equation 2.1, the Venc sets the maximum value for each individual velocity component. If the Venc is set too low, then signal intensities from the blood representing velocities higher than the Venc will "wrap" around and provide an incorrect value, an issue called **velocity aliasing** (Figure 2.1). Correcting aliasing errors is non-trivial and generally it is simply easier to calibrate the scanner settings to avoid aliasing issues. However, there are also reasons to avoid setting the Venc too high. The noise relative to Venc remains the same regardless of the value of the Venc set. Therefore, higher values of Venc will result in obscuring a greater proportion of low velocity values with noise. Overly conservative (high) Venc values can lead to useless imaging results, particularly since regions of low flow are often of great interest because they occur in abnormal conditions, like aneurysms and post-stenotic recirculation zones.

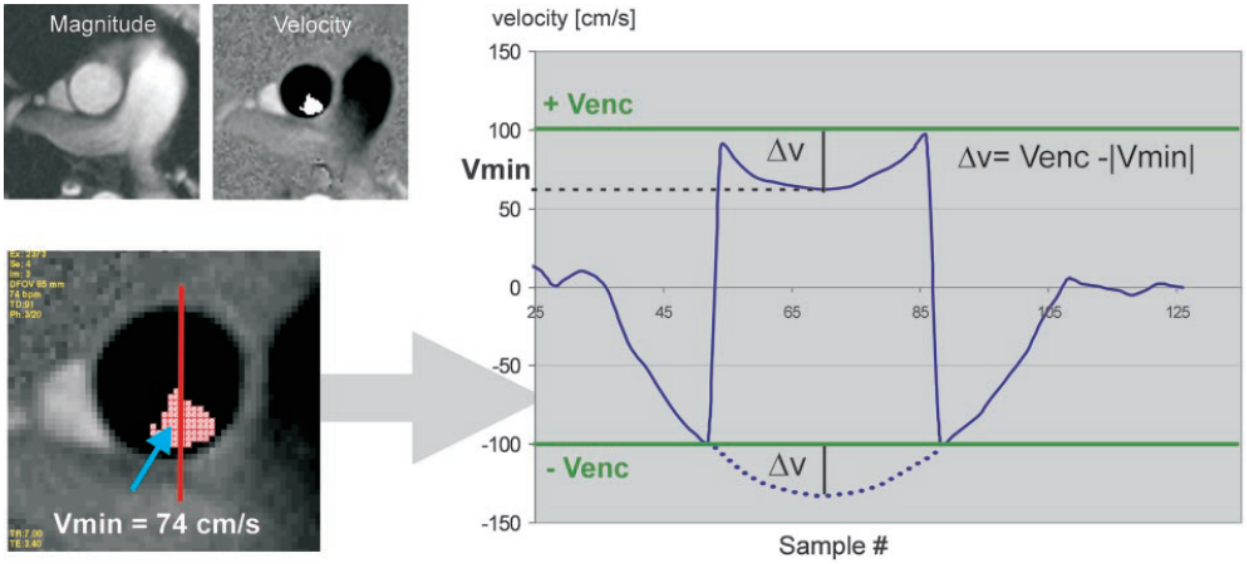

Figure 2.1: A depiction of the effect of velocity aliasing due to low Venc (reprinted from Lotz et al. 2002 [25] with the permission of the Radiological Society of North America). The velocity profile taken across the cross section appears discontinuous because the velocity magnitudes lower than negative Venc "wrap" around and are interpreted as values near positive Venc.

2.1.2 Background Correction

The physics of 4D-MR imaging require multiple, overlapping magnetic fields with linear gradients in orthogonal directions. The application of magnetic field gradients induce secondary currents, or *eddy currents*, in the metallic components of the scanner system, and these currents in turn generate unwanted magnetic fields. These add undesirable contributions to the measured phases and are termed **phase offsets** [26] [27]. As seen in the previous section, errors in phase will result in errors in velocity and will subsequently affect the extracted flow features. In 3D, errors in the individual velocity components can lead to velocity vectors that are misaligned with the blood flow, which often results in errant streamlines or pathlines.

From Figure 2.2, we can see that phase offsets are spatially-varying but not random. These errors can be mitigated by a process called **background correction**, which estimates the contribution of the phase offsets errors to the velocity measurements by fitting it to a polynomial function [26]. The procedure is as follows:

1. For each voxel j, compute the standard deviation of its velocity (v_j) over time, $SD_{v,j}$.

2. Calculate a weighting term w_j based on the voxel's magnitude value m_j and $SD_{v,j}$, which provides an estimation of the error at each voxel:

$$w_j = \frac{m_j}{(SD_{v,j})^p} \tag{2.2}$$

   where p dictates the contribution of SD_v to the weighting term. In practice, p was set to 2.

3. Fit the phase offset contributions to a polynomial by performing a weighted least-squares fit:

$$\min_{a_i} \sum_{j=1}^{n} (w_j(v_j - \mathbf{B}_{ij}a_i))^2 \tag{2.3}$$

   The term $\mathbf{B}_{ij}a_i$ is a matrix index representation of a polynomial function sampled on a discrete lattice (the image coordinates). For a trilinear polynomial sampled at voxel j with coordinates (x_j, y_j, z_j),

$$\mathbf{B}_{ij}a_i = a_0 + a_1x_j + a_2y_j + a_3z_j \tag{2.4}$$

As suggested in [26], a linear fit is inadequate for fitting phase offset errors, and instead we use a second-order polynomial, which introduces cross-terms:

$$\begin{aligned}\mathbf{B}_{ij}a_i = a_0 + a_1 x_j + a_2 y_j + a_3 z_j + a_4 x_j^2 + a_5 y_j^2 + a_6 z_j^2 \\ + a_7 x_j y_j + a_8 x_j z_j + a_9 y_j z_j\end{aligned} \tag{2.5}$$

4. Evaluate the fitted polynomial at all locations to estimate the phase offset contribution to the velocity (the *correction term*).

$$v_{j,\text{ phase offset}} = \mathbf{B}_{ij}a_i \tag{2.6}$$

5. Subtract the estimated contribution from the velocity measurement to get the "corrected" velocity.

$$v_{j,\text{ corrected}} = v_j - v_{j,\text{ phase offset}} \tag{2.7}$$

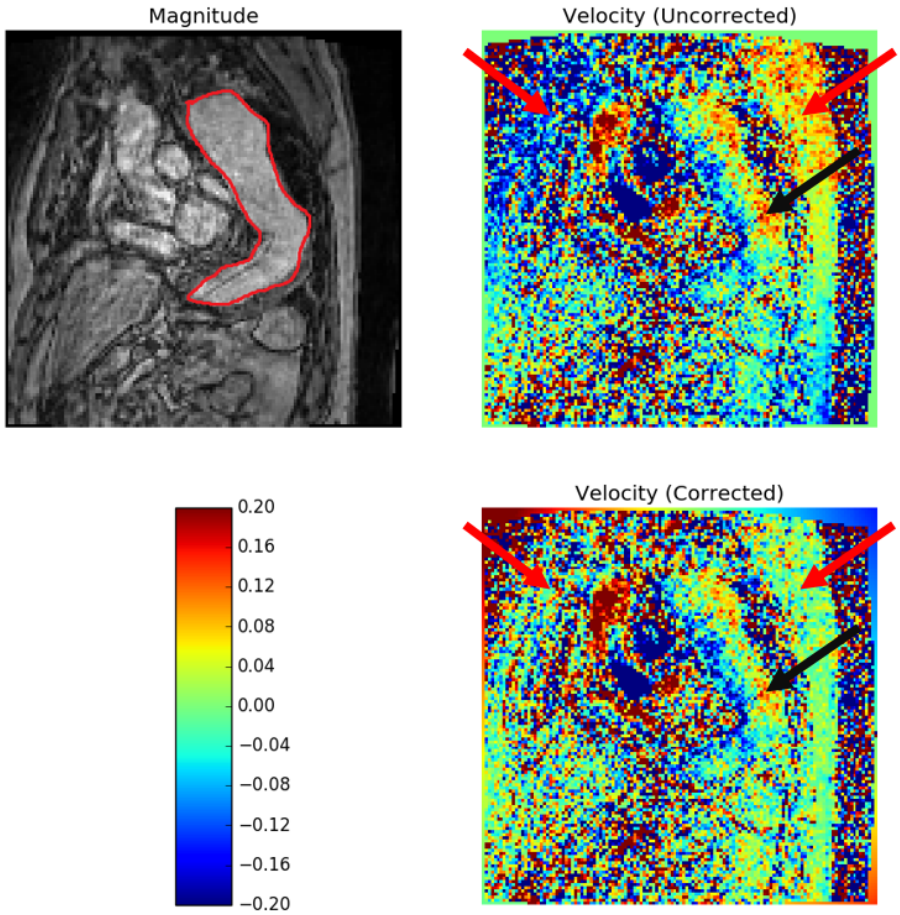

Figure 2.2: An example of the effects of background correction on velocity in an image slice of a 4D-flow acquisition of a patient's aorta (outlined in red in the Magnitude image, *Upper Left*). (*Upper Right*) The corresponding uncorrected velocity magnitude. (*Bottom Right*) The corrected velocity magnitude. The red arrows point to areas that should be zero (green), but are either significantly nonzero (red or blue) due to phase offset errors. After the background correction, we can see that velocity in these areas have been set to zero. The black arrows point to velocity values in the aorta, which has also been changed to a lesser extent by the background correction.

2.1.3 Segmentation

Segmentation is the process of extracting relevant geometrical features from images. It would be extremely difficult to analyze 4D-MR data without segmentations that define the relevant region of interest.

Segmentation on its own is an extensive field of research, but here we focus on the most common methods used in our research, which are the ones primarily implemented by our segmentation tool of choice, the Vascular Modelling Toolkit (VMTK) (Orobix; Bergamo, Italy).

2.1.3.1 Threshold segmentation

Threshold segmentation simply involves a binary separation of the voxels into two sets: Voxels whose associated scalar values are above a chosen threshold, and voxels with values below the threshold (Figure 2.3AB).

The most obvious drawback of threshold segmentation is that there is no quantitative scaling factor in MRI acquisitions. Furthermore, MR of flowing blood typically has variations in signal intensity values that are related to flow-related effects. It is therefore challenging to select an intensity value to uniquely differentiate between flowing blood and adjacent tissue. The geometry of the vessels may therefore vary with the chosen threshold, which may affect subsequent measurements including flow quantification (since flow is calculated as $\textit{mean velocity} \cdot \textit{area}$). There are no established criteria for choosing the threshold that best represents the true geometry, so the choice of threshold will often vary between segmentation trials and observers.

Additionally, depending on the data, threshold segmentation may be insufficient for isolating the region of interest and may require more processing steps and effort.

2.1.3.2 Level-Set Segmentation

Level-set segmentation can help avoid some of the issues related to threshold segmentation by automatically refining the segmentation toward specific criteria. For segmentation of cardiovascular structures, the criteria are vessel edges, which are defined to be areas of greatest image gradient magnitude. In practice, this means that given an initial contour of the vessel, the level-set segmentation will "push" the contour so that it best coincides with the vessel edge.

Level-set segmentation assumes that the contour of interest C is the 0-level set of an implicit surface represented by an arbitrary scalar function ϕ. Put another

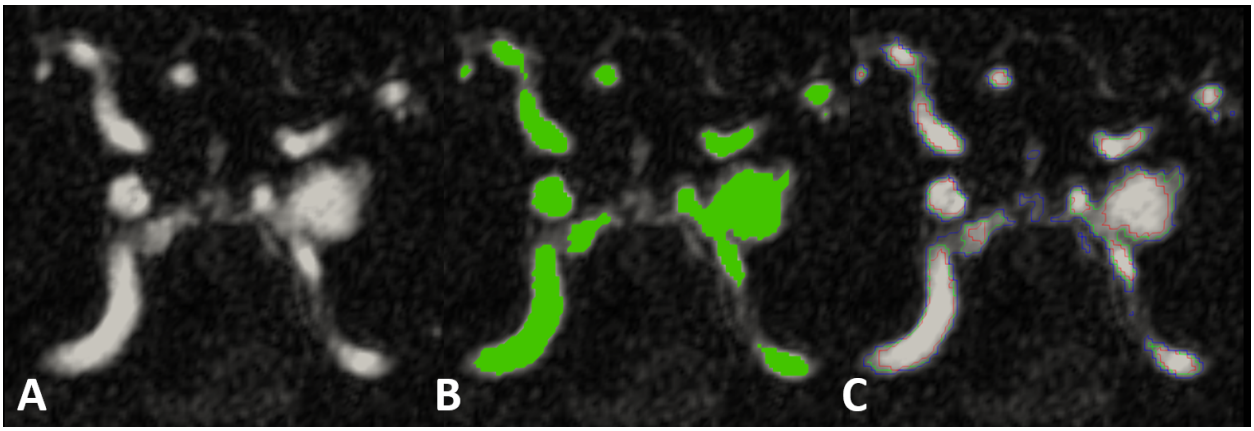

Figure 2.3: Demonstration of threshold segmentation. (**A**) A 2D cross-section of a CE-MRA image of a cerebral aneurysm aligned with the vessel axis. This is atypical as 2D-cross sections are usually taken transverse to the vessel axis and is for visualization purposes only. (**B**) Threshold segmentation based on choosing a specific gray-level. (**C**) Multiple contours (red, green, blue) representing segmentations at different thresholds.

way, C is the set of all points where $\phi = 0$:

$$C = \{(\mathbf{x}, t) | \phi(\mathbf{x}, t) = 0\} \tag{2.8}$$

or equivalently:

$$\phi(C(t), t) = 0 \quad \forall t \tag{2.9}$$

The parameter t is not physical and represents the dimension over which the refinement takes place. The images that we segment are typically not time-dependent, i.e., they are three-dimensional, not four-dimensional. ϕ is defined such that its value at any point in the image is the signed distance from the contour, where values from inside the contour are negative and values outside the contour are positive (or vice versa):

$$\phi(\mathbf{x}, t) = d \tag{2.10}$$

By taking the time-derivative of 2.10 and applying the chain rule, we can derive the evolution equation for ϕ:

$$\frac{\partial \phi}{\partial t} = -v \|\nabla \phi\| \tag{2.11}$$

where $v = v(\mathbf{x})$ is the "speed" of the evolution of ϕ in the direction normal to C. v controls how much a surface evolves for after each "time step" or iteration of the

algorithm. A positive value of speed will push the contour outward and a negative value will push the contour inward. If the speed is zero at a location, then the contour will not advance at all and the refinement effectively ends.

Consequently, for vessel segmentation we would like the speed to be zero at the vessel edges, where the magnitude of the image gradient ∇I is greatest. Then an appropriate expression for v is:

$$v(\mathbf{x}) = \frac{1}{1 + \lambda \|\nabla I(\mathbf{x})\|} \tag{2.12}$$

where λ adjusts the costs of encountering an edge. More sophisticated level-set segmentation methods modify the denominator to depend on more than the image gradient, such as contour smoothness. Equation 2.11 can be discretized using an upwind scheme in space and forward difference in time to provide a numerical expression for ϕ at position i for the next iteration, $n + 1$ (presented in 1-D for simplicity):

$$\phi_i^{n+1} = \phi_i^n - (max(v_i, 0) D_x^- \phi_i^n + min(v_i, 0) D_x^+ \phi_i^n) \tag{2.13}$$

where $D_x^- \phi_i^n$ and $D_x^+ \phi_i^n$ are the forward and backward difference discretizations of the spatial gradient:

$$D_x^+ \phi = \frac{u_{i+1} - u_i}{\Delta x} \tag{2.14}$$

$$D_x^- \phi = \frac{u_i - u_{i-1}}{\Delta x} \tag{2.15}$$

In summary, a segmentation of the vessel can be semi-automatically extracted from an image by providing an initial contour C, embedding it into a hypersurface ϕ, and evolving ϕ by applying equations 2.12 and 2.13, using the image gradient ∇I to guide the refinement such that the contour aligns with the vessel edges (Figure 2.4). The initialization can be provided by a threshold segmentation, or through other methods, such as fast marching.

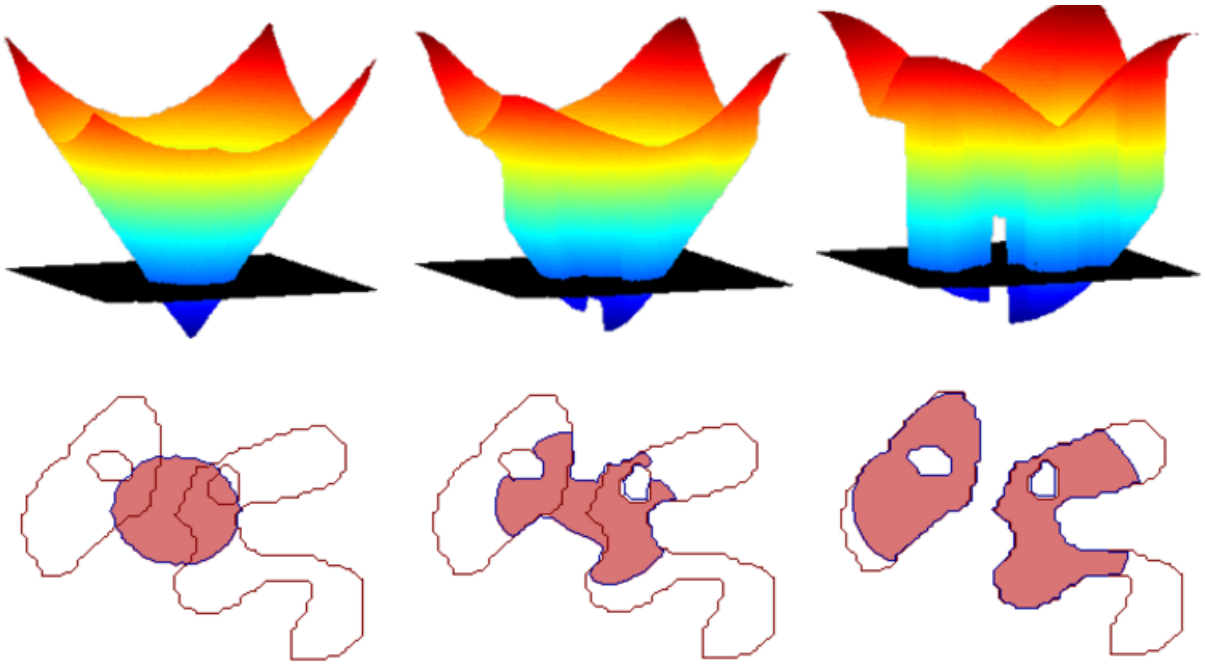

Figure 2.4: A visualization of the contour evolution of level set segmentation in 2D (provided by [28]). The top row reveals how the level set function ϕ evolves in time to fit the desired shape on the zero-level plane, which is depicted in the bottom row by the red contour. The bottom row shows the correponding evolution of the zero-level contour.

2.1.4 Flow Visualization

After the segmentation has been completed, it can be used to "mask" the velocity data (Figure 2.5).

Flow patterns are often qualitatively visualized by calculating streamlines or pathlines (Figure 2.6). In practice, streamlines and pathlines are calculated by numerically solving the following differential equations from an initial set of seed points, x_{P0}, and the velocity field u_0:

$$\frac{d\mathbf{x}_P}{dt} = \nabla \mathbf{u}_P(\mathbf{x}_P, t)\mathbf{x}_P, \quad \mathbf{x}_P(t_0) = \mathbf{x}_{P0} \tag{2.16}$$

In any simulation post-processing software, Equation 2.16 is solved by Runge-Kutta methods, specifically explicit fourth-order (RK4), though other types may be available.

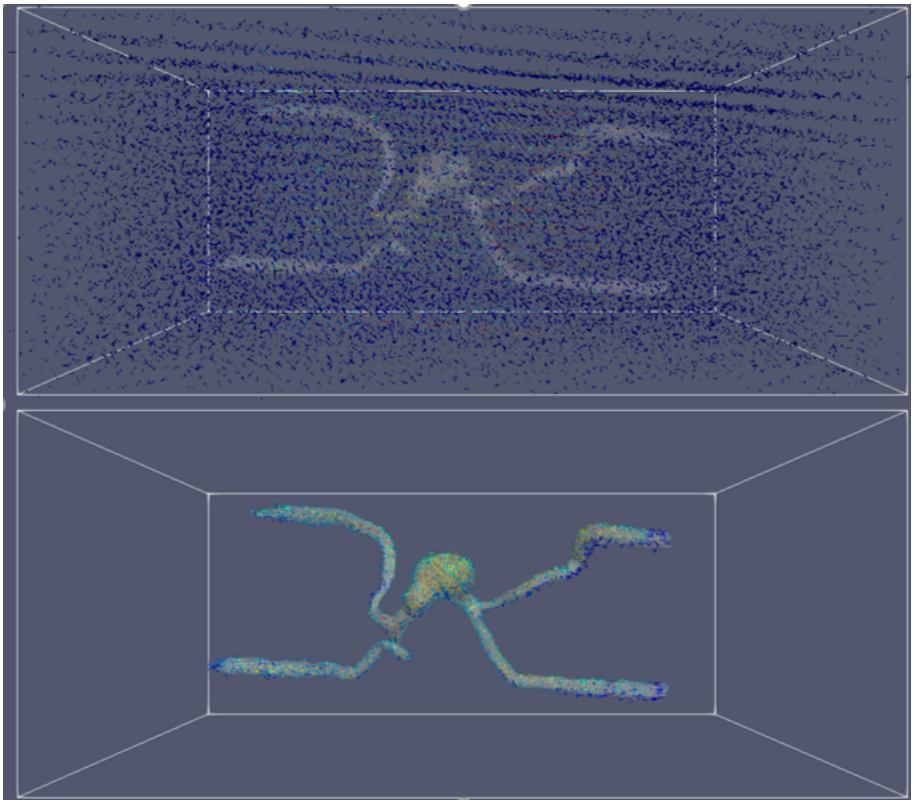

Figure 2.5: It is difficult or impossible to obtain meaningful results from the entire image slab (top). A segmentation can be used such that only the velocity data within the region of interest is seen (bottom). The two have different density settings for the velocity vector glyphs.

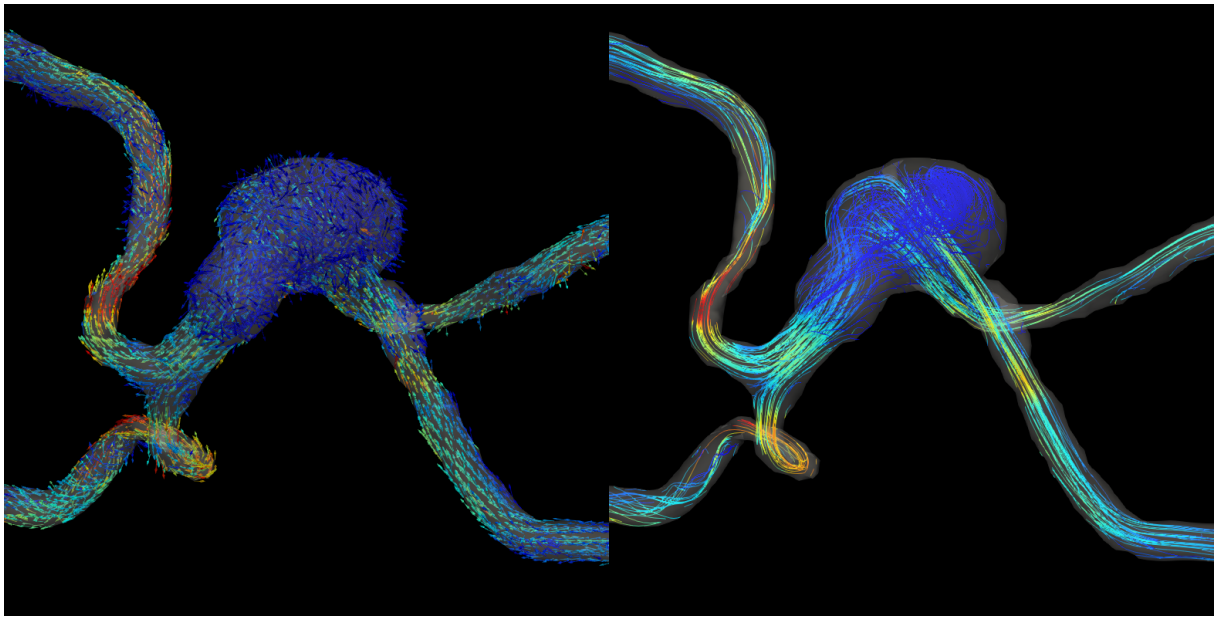

Figure 2.6: Example of flow visualization using masked velocity vectors, and the streamlines representing the velocity field.

2.1.5 Flow Quantification

Flow (Q) is defined as:

$$Q = \int_A \mathbf{u} \cdot \mathbf{n} dA \tag{2.17}$$

where A is the cross-sectional area, and $\mathbf{n}$ is its normal. Flow quantification from 2D PC-MRI is simplified by the fact that the imaging plane is assumed to be perpendicular to the direction of flow. Then Equation 2.17 reduces to simply:

$$Q = nwh \sum_i^n v_i \tag{2.18}$$

where w and h are the pixel edge sizes, and v_i is the velocity measured by the pixel.

Extracting the flow from 4D-MRI is complicated by the fact that velocity is fully 3D and that vessels are tortuous, so that the flow plane changes at every point along the vessel. The following sequence is used to calculate flow from 4D-MRI sequences:

1. A surface is extracted from the segmentation.
2. A centerline is calculated from the surface using VMTK, which was developed and implemented by Luca Antiga [29] (Figure 2.7A).
3. Lumenal cross-sections orthogonal to the vessel are obtained, using planes defined by the tangent vectors of the centerline. (Figure 2.7B).
4. For each cross-section, the flow is calculated according to Equation 2.17 (Figure 2.7C).
5. To avoid issues due to noise (explored in Chapter 3), flow values from multiple cross sections are averaged.

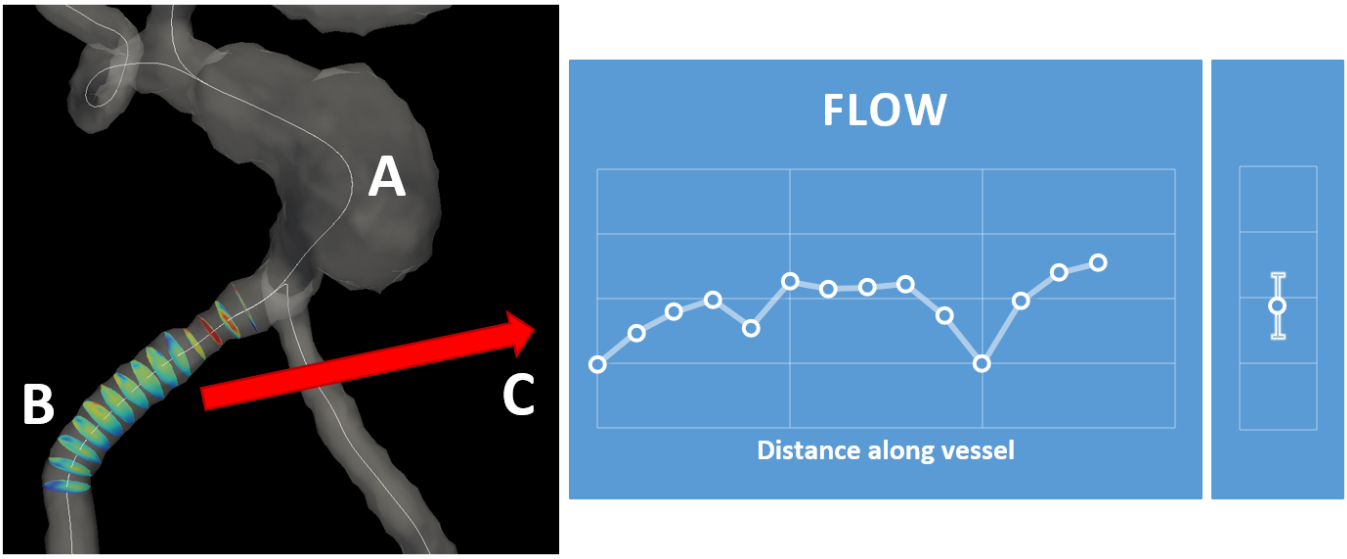

Figure 2.7: Representation of flow calculation procedure for 4D-MR images. (*Left*) Centerlines and vessel cross sections extracted from the angiogram and 4D-flow data. (*Middle*) For each cross section, flow is calculated as the area integral of the normal velocity component. (*Right*) The average and standard deviation of the flow values are calculated.

2.2 Simulation

This section details the major steps required to build a patient-specific computational fluid dynamics (CFD) simulation that reasonably represents *in vivo* physiological conditions. The primary tool for CFD analysis used in this thesis is the commercial computational package FLUENT (ANSYS, Canonsburg, PA), which is based on the Finite Volume Method (FVM).

Figure 2.8 shows the generalized pipeline for building patient-specific CFD analyses from medical images. Each step will be explained in more detail in the following subsections.

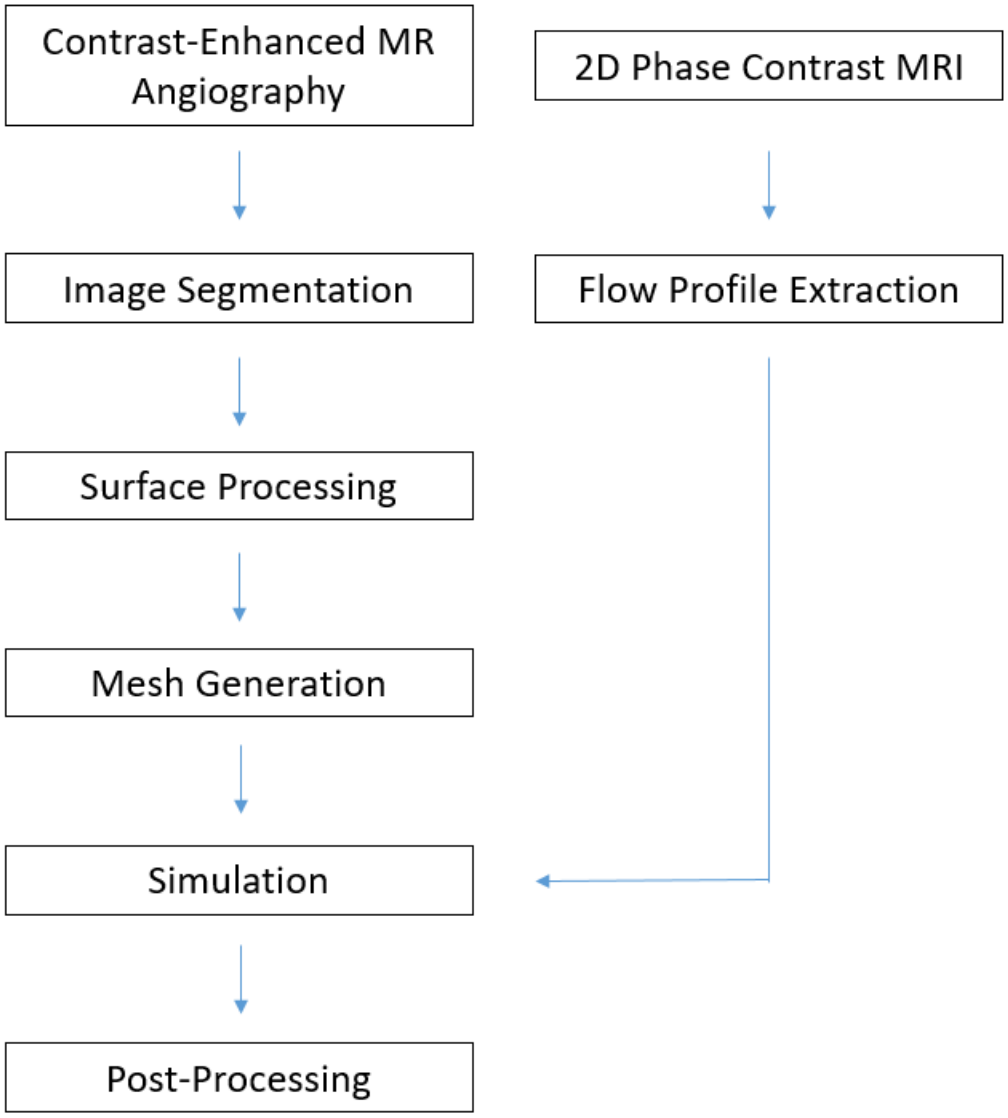

Figure 2.8: Pipeline from image acquisition to simulation analysis.

2.2.1 Geometry

Building a simulation begins with extracting the vascular geometry from a set of medical images (Figure 2.9). This can be achieved by first performing a segmentation using the same methods as described in Section 2.1.3. A polygonal (triangular) mesh representation of the vessel isosurface can be extracted from the segmentation usng the Marching Cubes algorithm.

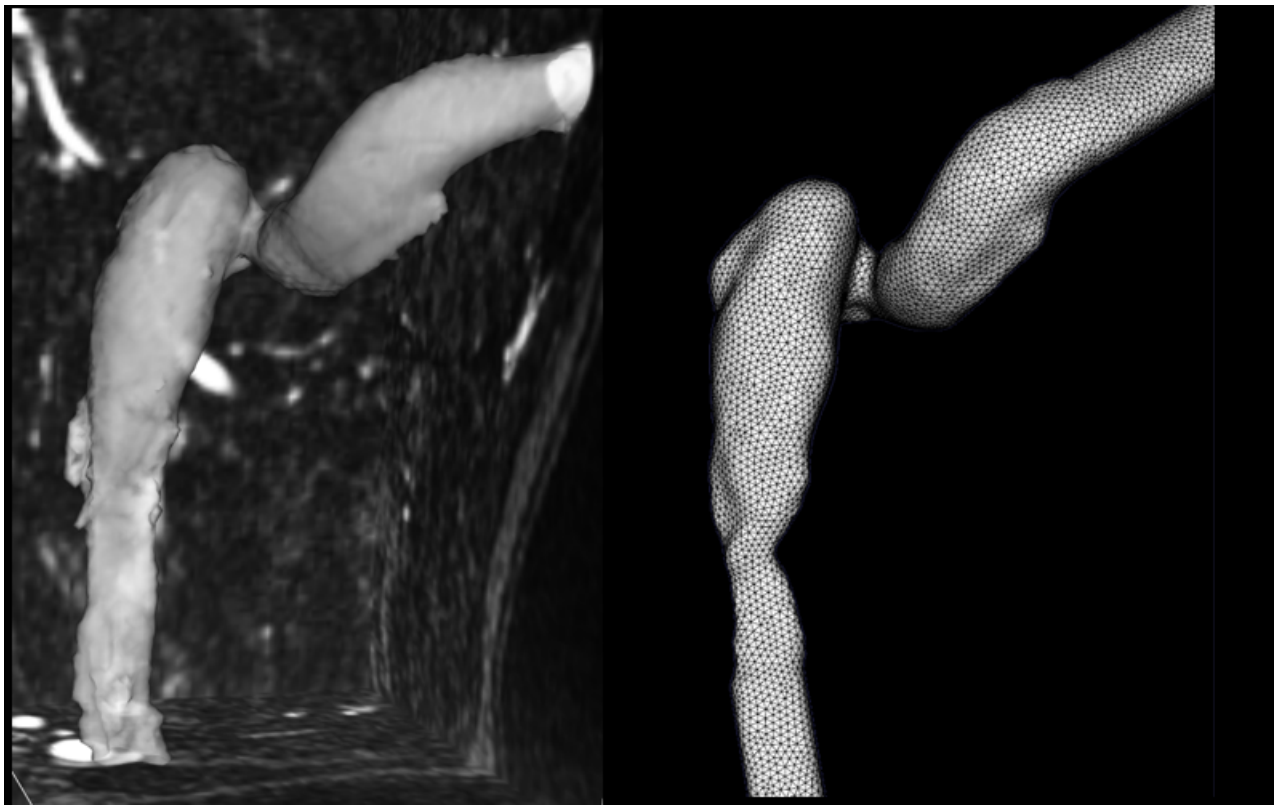

Figure 2.9: The extraction of the simulation geometry from the MR angiogram. The left shows how the surface in relation the image volume. The right shows the resulting mesh, after processing.

Generally, the surface will require minor additional smoothing and editing to make it suitable for meshing. The surface should represent a continuous domain with reasonable surface curvature to avoid any numerical difficulties. The surface should also be clipped orthogonally at the inlets and outlets. Flow extensions are often added at the inlets in order to ensure that the flow is developed and properly mimics the physiological flow profile. This is particularly important if the inlet boundary conditions provided are spatially-constant (as described in section 2.2.3.1).

2.2.2 Meshing

Meshing discretizes the fluid volume into cells in order to prepare it for simulation. One can choose between unstructured meshes, which are made of tetrahedral elements, or structured meshes, which are formed from hexahedral elements (or a mixture of the two). Structured meshes are preferable because they provide reasonable element density and neat data interpolation from the node or cell centers. However, constructing structured meshes for the tortuous, diverging geometries of the cardiovascular geometry is non-trivial. Additionally, vessel bifurcations can often lead to elements of poor quality. Thus, we generally use unstructured meshes, which can be generated quickly and semi-automatically. With suitable tools, unstructured meshes may take about 10-30 minutes to generate, while unstructured meshes may take hours or longer.

While meshes can be generated quickly, care must be taken so that simulations performed with these meshes must be accurate. Mesh density must be tuned to balance accuracy and computational time. Finer meshes are more accurate but take longer to simulate. Usually convergence tests are performed in order to choose the best mesh density. Meshes of multiple element densities are generated and used in simulations. For each simulation, certain parameters like maximum velocity are measured. The coarsest density for which simulation results remain relatively unaffected is chosen.

For fluid simulations, a boundary layer is particularly important, especially if one is investigating wall-dependent fluid descriptors, such as wall shear stress (WSS), or is attempting to simulate turbulence. As we mainly concern ourselves with laminar simulations, our boundary layer density was chosen based on mesh convergence tests.

2.2.3 Boundary Conditions

2.2.3.1 Inlets

Simulations are highly dependent on inlet boundary conditions. Multiple types are available (fluid velocity, mass flow, pressure); for our purposes, velocity appears to be the most convenient. To mimic a patient's hemodynamics accurately, the inlet values are based on MR measurements, usually from 2D-MR. This flow profile can then be prescribed by one of two ways: Either by interpolating the flow waveform onto the nodal points of the mesh, or by prescribing an integral value onto the entire inlet and allowing flow to develop. The latter is easier but obviously less accurate. However, a flat flow profile in a pipe will eventually develop into parabolic flow that resembles

physiological flow. Hence, the simplest approach is to add flow extensions to allow flow to develop.

2.2.3.2 Outlets

By assuming rigid walls for our CFD calculations, we minimize the effects of absolute pressure on the wall since flow is driven by the pressure gradient, as seen in the Navier-Stokes equations (2.2.4.1). For both simplicity and ease of numerical convergence, we simply prescribe zero-pressure at the outlets.

2.2.4 Computation of Fluid Physics

2.2.4.1 Fluid Mechanics

To describe fluid motion, we begin with the equations of conservation of mass and momentum:

$$\rho \nabla \cdot \mathbf{v} = \mathbf{0} \tag{2.19}$$

$$\rho(\dot{\mathbf{u}} + \mathbf{u} \cdot \nabla \mathbf{u}) = -\nabla p + \nabla \cdot \boldsymbol{\tau} \tag{2.20}$$

Blood under physiological conditions is generally considered to be incompressible and isothermal, which translates to divergence-free flow and constant viscosity.

In this thesis, blood has been modeled as a Newtonian fluid, for which viscous stresses are related to the velocity gradient by a viscosity tensor. This assumption may be inaccurate for regions of slow flow, where clotting or the mechanics of whole blood cells complicates the strain-stress relationship, but physiological validation of parameters that depend the most on the fluid material like wall-shear stress is not yet possible and potentially irrelevant in a clincial context, where measurement uncertainty is large and relationships between variables are more important than absolute values.

Assuming the fluid is also homogeneous and isotropic, the viscosity tensor reduces to a constant, and the constitutive equation for deviatoric stress can be related to the fluid velocity gradient as:

$$\boldsymbol{\tau} = \mu(\mathbf{u} + \mathbf{u}^T) \tag{2.21}$$

Substituting for $\boldsymbol{\tau}$ in Equation 2.20 gives us one form of the Navier-Stokes equations:

$$\rho(\dot{\mathbf{u}} + \mathbf{u} \cdot \nabla \mathbf{u}) = -\nabla p + \mu \Delta \mathbf{u} \tag{2.22}$$

2.2.4.2 Finite Volume Method

Simulations in this thesis were performed with the computational package ANSYS FLUENT, which employs the finite volume method (FVM) to calculate the physical properties of interest (generally pressure and velocity). FVM is ideally suited for fluid simulations because it separates the domain into control volumes or cells. Average values for each cell are calculated by computing fluxes through the cell faces. Conservation of physical properties hold because FVM schemes force fluxes into the cell to be equal to fluxes coming out of the cell.

Derivation of FVM equations begin with the integral form of a conservation law. For a generic property ϕ, its conservation equation is:

$$\dot{\phi} + \nabla \cdot \mathbf{q}_\phi = 0 \tag{2.23}$$

where $\mathbf{q}_\phi$ is the flux of ϕ. For each cell i, we integrate Equation 2.23 over its volume, v_i:

$$\int_{v_i} \dot{\phi} \mathrm{d}v + \int_{v_i} \nabla \cdot \mathbf{q}_\phi \mathrm{d}v = 0 \tag{2.24}$$

By the divergence theorem, the second term on the left-hand side is converted into a surface integral:

$$\int_{v_i} \dot{\phi} \mathrm{d}v + \oint_{S_i} \mathbf{q}_\phi \cdot \mathbf{n} \mathrm{d}S = 0 \tag{2.25}$$

The integral in the first term provides the cell average of the time derivative $\bar{\dot{\phi}}_i$, which is stored geometrically at the cell center:

$$\bar{\dot{\phi}}_i v_i + \oint_{S_i} \mathbf{q}_\phi \cdot \mathbf{n} \mathrm{d}S = 0 \tag{2.26}$$

Finally, the surface integral can be represented as the sum of the fluxes through each cell face f, which when slightly rearranged provides:

$$\bar{\dot{\phi}}_i = -\frac{1}{v_i} \sum_f \mathbf{q}_{\phi,f} \cdot \mathbf{n}_f A_f \tag{2.27}$$

where A_f is the area of the cell face and $\mathbf{n}_f$ represents the cell face normal. Equation 2.27 can then be used to evolve in ϕ_i in time. For first-order time integration, the cell value at the next time step $n+1$ can represented as:

$$\phi_i^{n+1} = \phi_i^n + \Delta t \dot{\phi}_i^{n^*} \tag{2.28}$$

The superscript for the time derivative term (n^*) is a placeholder for either n or $n+1$ depending on whether the time integration is implicit or explicit (implicit integration would require an iterative solution). In practice, the blood flow simulations performed in this thesis work best with coupled pressure-based solvers, which require implicit time integration.

The FVM form of the continuity and momentum equations can be found by substituting density ρ or momentum per unit mass $\rho\mathbf{u}$ for ϕ.

2.2.4.3 Derived Fluid Descriptors

In this study, there are two established descriptors used to analyze fluid flow. The first is wall shear stress (WSS), which links fluid mechanics to biochemistry:

$$\boldsymbol{\tau}_{\text{wall}} = \mu \frac{\partial \mathbf{u}}{\partial \mathbf{n}} \tag{2.29}$$

where the term $\partial\mathbf{u}/\partial\mathbf{n}$ is the directional derivative of the fluid velocity near the wall relative to the wall normal.

The second is Swirling Strength, which is used to quantify and visualize vortex strength (Figure 2.10). Mathematically, swirling strength is the complex eigenvalue of the velocity gradient. Conceptually, this is because swirling occurs at points that can be considered sources and sinks, i.e., the streamlines emanating from a point can be described by a complex exponential (Figure 2.11). The complex eigenvalue is then associated with two complex eigenvectors that together span the plane of swirling, while the real eigenvector represents the swirling axis. The swirling strength is then a measure of how quickly streamlines spiral around that point (Figure 2.12).

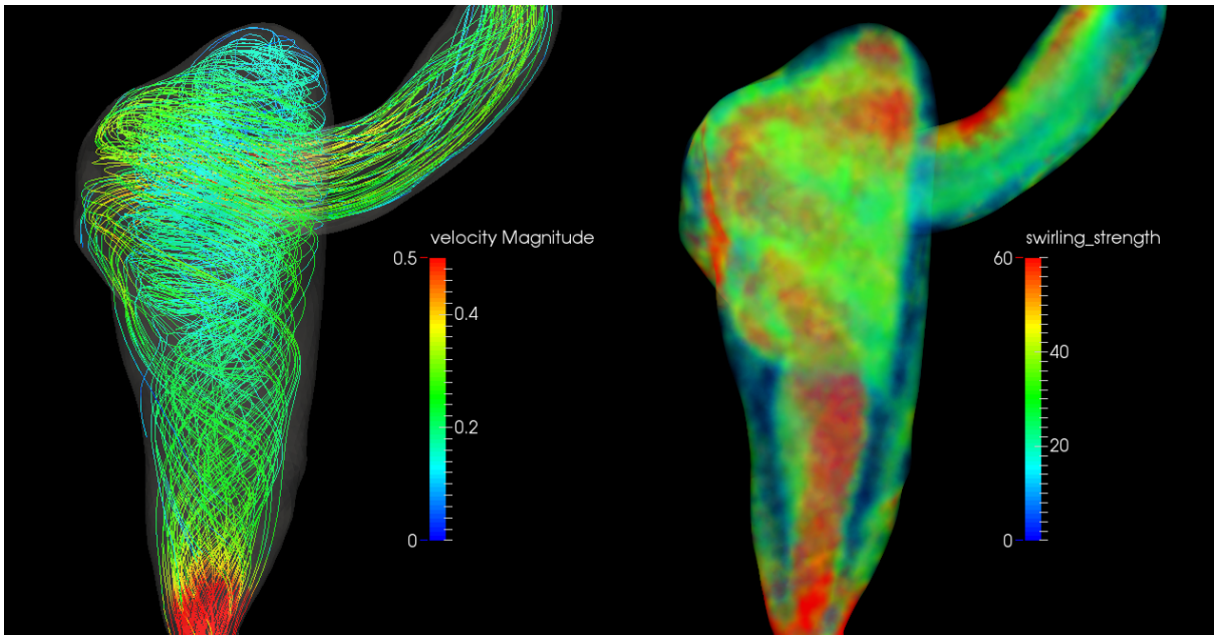

Figure 2.10: An example of applying swirling strength to an analysis of cardiovascular CFD results, specifically of a patient's internal jugular vein.

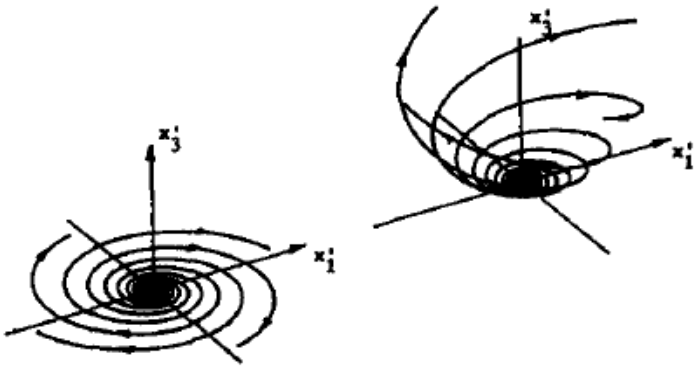

Figure 2.11: Spiraling streamline trajectories representing complex solutions to Equation 2.16 (adapted from Chong et al. 1990 [30], with permission from AIP Publishing).

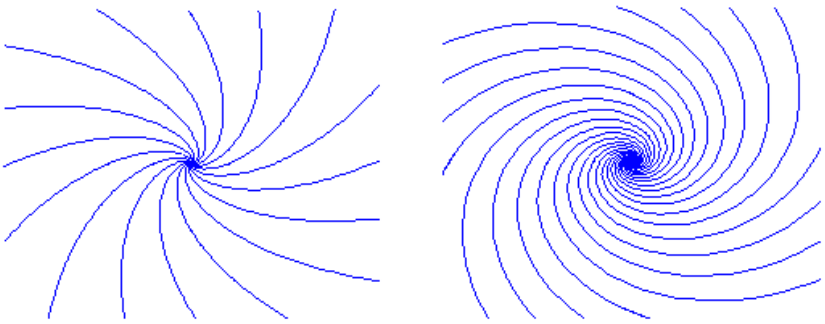

Figure 2.12: Visual comparison of "lower" swirling strength on the left and "greater" swirling strength on the right.

Chapter 3

Error estimation in a cerebral aneurysm phantom

3.1 Introduction

In section 1.3.1.2, we briefly mentioned that the current practical imaging resolution for 4D-flow imaging (about 1.3mm isotropic) is too coarse for reliable calculations of potential biomechanically-relevant parameters like WSS. This is especially true for the small blood vessels in the cerebral vascalature, which may often have single voxel or sub-voxel resolution diameters. Therefore, part of our motivation for using CFD for evaluating cardiovascular pathologies is to obtain data in greater temporal and spatial resolution than can be measured from imaging methods. However, these simulations still rely on accurate blood flow measurements from MR velocimetry (MRV) and can be affected by system imperfections, such as magnetic field gradient non-linearities and eddy currents. These imperfections can affect the results differently depending on the acquisition type (2D, 3D) or acquisition position (the distance from the isocenter of the MR scanner). In this chapter, we investigate how these errors might affect the flow quantification by:

1. Constructing a flow model with a highly structured velocity field from a patient cerebral aneurysm.

2. Comparing flow measurements obtained from 2D-MR and 4D-MR acquisitions to a known experimentally-measured flow value.

3. Comparing the velocity fields between a 4D-MR measurement and a CFD simulation.

4. Estimating the effect of the flow measurement uncertainty on the hemodynamics within the aneurysm.

3.2 Methods

3.2.1 Image acquisition and flow analysis

A silicone phantom of a large cerebral basilar aneurysm was constructed using a 3D-printer and a patient data set (Figure 3.1). This particular geometry was chosen because of its highly structured velocity field (see Figure 3.2). The phantom was attached to a flow apparatus, where flow was driven by a gravity-fed pressure head that provided constant flow.

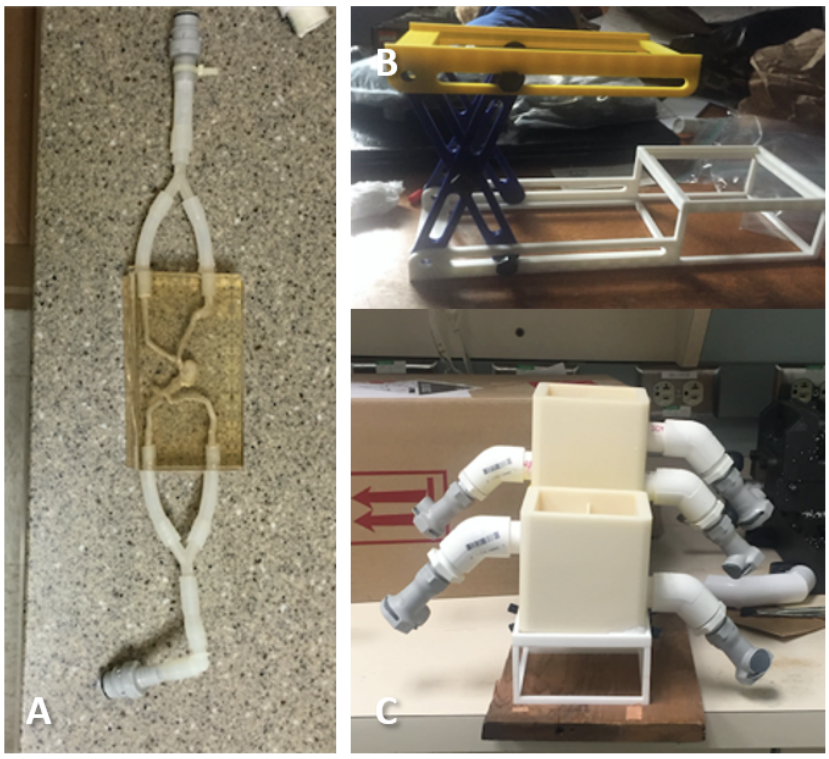

Figure 3.1: A view of the phantom.

4D-MR acquisitions of the phantom were obtained under three conditions:

1. Cine-MR at the isocenter of the scanner for 5 time points.
2. Continuous measurement at the isocenter.

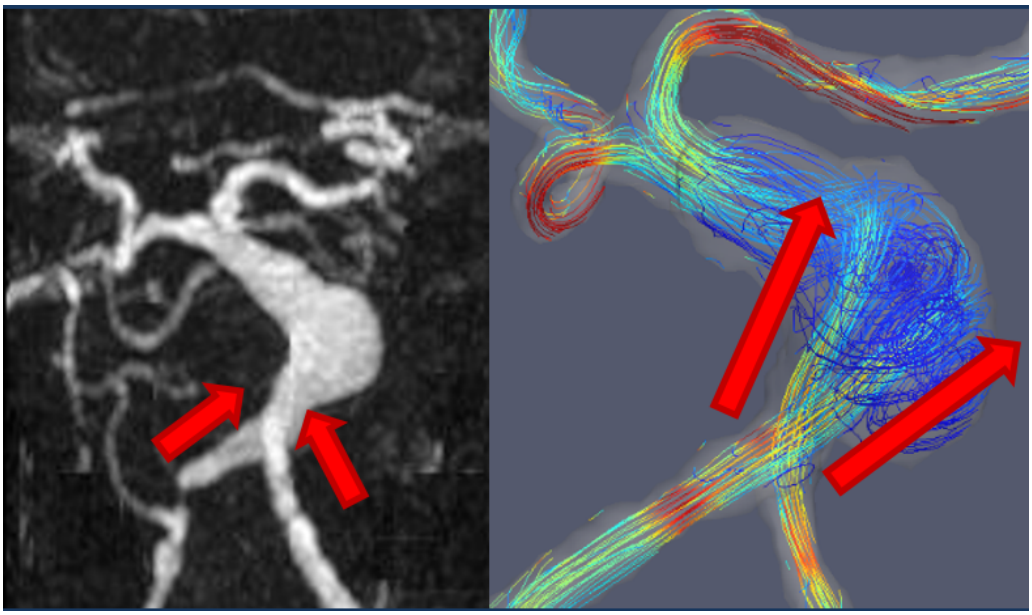

Figure 3.2: *Left*: Patient MIP view of the cerebral aneurysm used as the basis of the phantom. *Right*: Streamline visualization of the velocity field within the phantom emphasizing the jets from the two inlets.

3. Continuous measurement at 10cm offset from the isocenter.

2D-MR acquisitions were obtained at 5 locations along each inlet (Figure 3.3). Total flow through the phantom was determined experimentally by measuring the volume of fluid flow out of the model into a graduated cylinder and recording the time of collection. This measurement was considered to be the ground truth. A CE-MRA image was also acquired to capture the geometry, which was used for both imaging analysis and simulations.

For each acquisition condition, flow was quantified from the 4D-MR and 2D-MR images using the methods and tools detailed in Chapters 2 and 3. The "true" flow through each individual inlet was determined by estimating the flow ratios from the flows measured from 4D-MR and multiplying by the experimentally measured total flow:

$$Q_{\text{inlet1, 4DMR}} = f_{\text{inlet1, 4DMR}} \cdot Q_{\text{total, true}} \tag{3.1}$$

$$Q_{\text{inlet2, 4DMR}} = f_{\text{inlet2, 4DMR}} \cdot Q_{\text{total, true}} \tag{3.2}$$

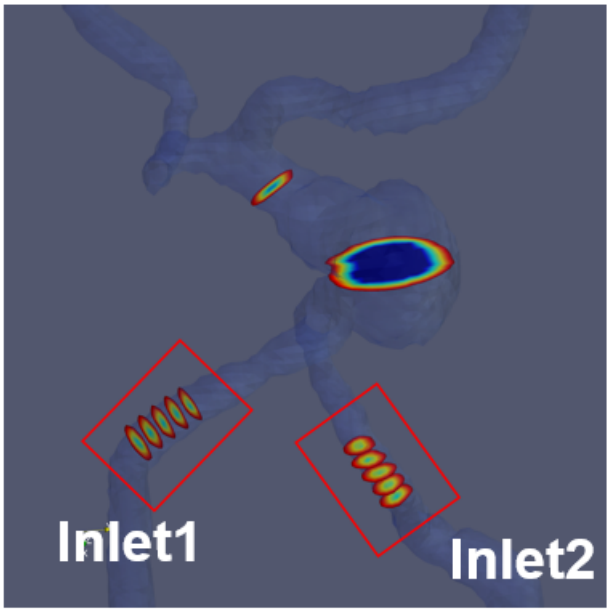

Figure 3.3: Locations at which 2D-MR acquisitions were obtained.

3.2.2 Simulation

The phantom geometry was extracted by segmenting the CE-MRA image using VMTK. Tetrahedral meshes with prismatic boundary layers were generated. Mesh resolution tests were performed to determine the optimal cell-size for balancing simulation accuracy with computational time, which in this case was 0.6mm target edge-length and 0.075mm target boundary sublayer height. Simulations were performed using FLUENT. A coupled solver was used with 2nd-order pressure and 2nd-order momentum discretization.

For comparison with 4D-MR measurements, a simulation was performed using experimentally-measured flow rates for both inlets as described in the previous chapter. To examine the effect of flow measurement uncertainty on simulation results, 2 sets of simulations were performed: one varying the total flow rate while holding the flow ratio constant, the other varying the flow ratio while holding the total flow rate constant. The simulation parameters are summarized in Table 3.1.

3.2.3 Simulation uncertainty analysis

The key metric we used to assess the effect of different flow conditions on overall wall shear stress on the anuerysm dome is the *area of low WSS* (Figure 3.4, where "low

Simulation	Condition	Total Flow (mLs^{-1})	Inlet1 Flow Fraction
1	Measured Flow, Measured Ratio	3.1	0.56
2	Low Flow, Measured Ratio	2.58	0.56
3	High Flow, Measured Ratio	3.64	0.56
4	Measured Flow, Low Ratio	2.58	0.46
5	Measured Flow, High Ratio	2.58	0.66

Table 3.1: Summary of inlet boundary conditions for a set of simulations used for estimating the effect of flow uncertainty on simulation results. Simulations 1, 2, and 3 form a set of simulations that vary flow, while keeping the flow ratio between inlets 1 and 2 constant. Simulations 1, 4, and 5 form a set of simulations that vary the flow ratio while holding the total flow constant. The choice of "high flow" and "low flow" are extracted from the flow quantification results described in Section 3.3.2. When varying the flow ratio, we simply decreased and increased the flow ratio through inlet1 by 10%.

WSS" is defined to be below 0.3 Pa based on preliminary simulation and morphological data that suggested aneurysm growth was most apparent in areas where WSS was below 0.3 Pa (Figure 3.5).

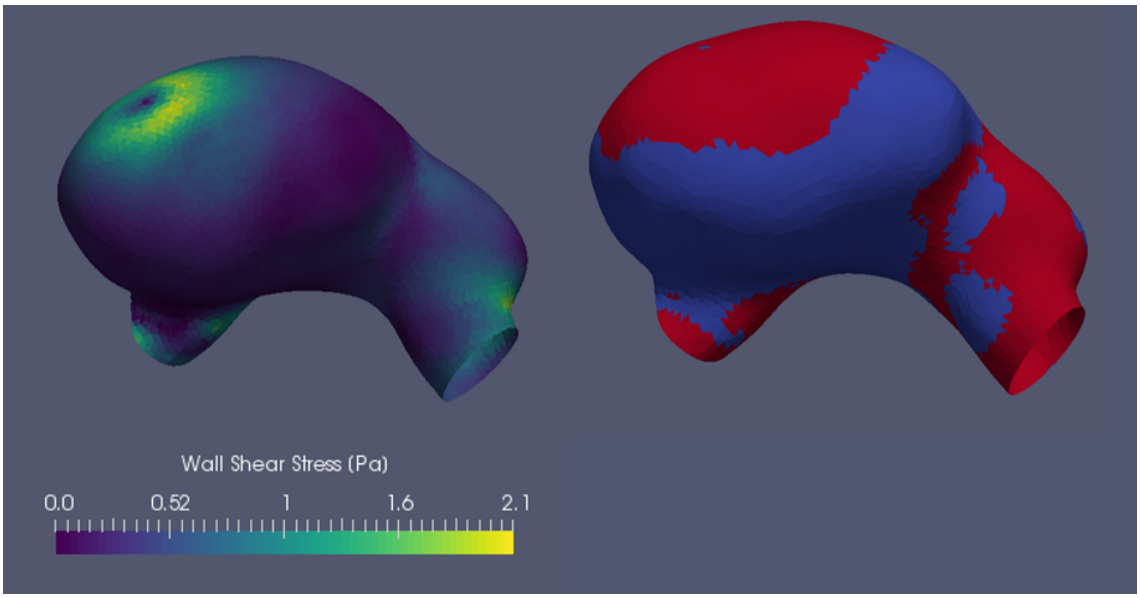

Figure 3.4: A visual explanation of the low WSS threshold. The right image depicts the separation of the aneurysm wall into regions below 0.3 Pa (blue) and those above (red). This area is quantified by summing the area of wall cells below the threshold.

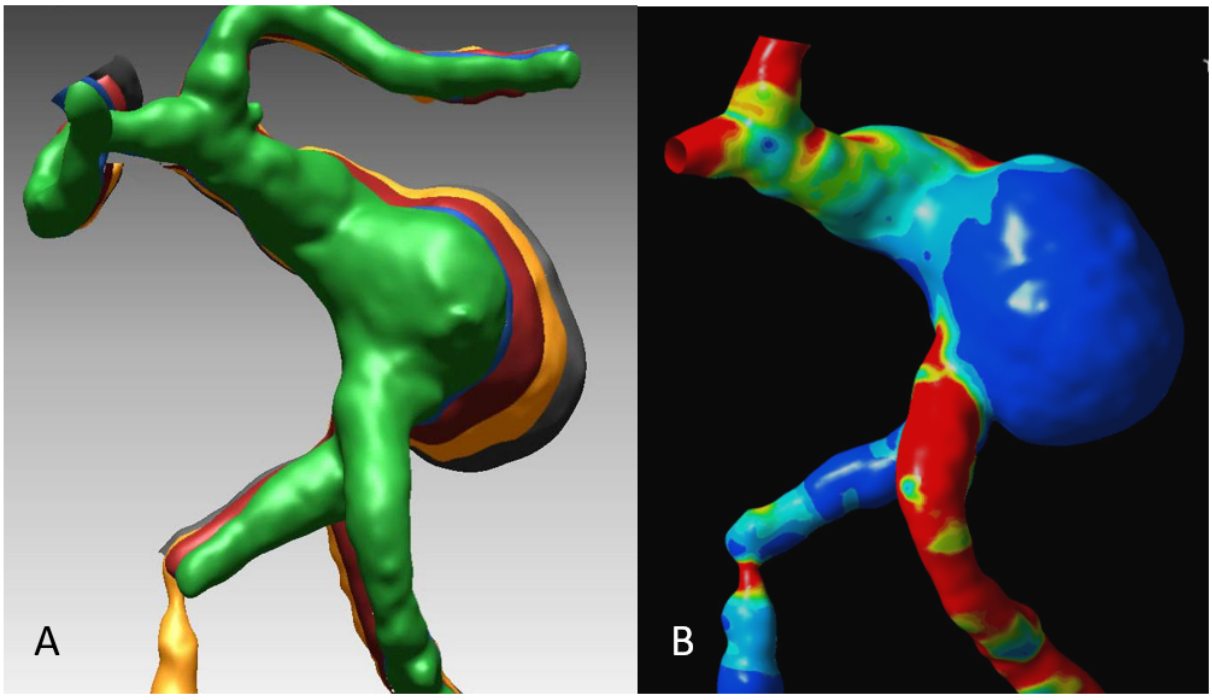

Figure 3.5: Preliminary results to support the use of 0.3 Pa as a threshold for low WSS. (**A**) Geometric results showing the growth of the aneurysm over 4 time points. (**B**) CFD results depicting the WSS distribution at one time point, where blue = 0.3 Pa).

3.3 Results

3.3.1 Positioning Effects on Flow Measurements

Figure 3.6 compares the streamlines extracted from 4D-MR for two continuous measurement acquisitions taken at two different positions: At the scanner isocenter and 10cm offset from the isocenter. The overall flow patterns appear similar in magnitude and shape, but there are regions within which the velocities measured at 10cm offset are noticeably lower than the corresponding velocities at 0cm offset, particularly wherever jets are found. This is supported quantitatively by Figure 3.7, which shows the flow measurements taken along the inlets. Also included in Figure 3.7 are flow measurements from a cine acquisition taken at the isocenter.

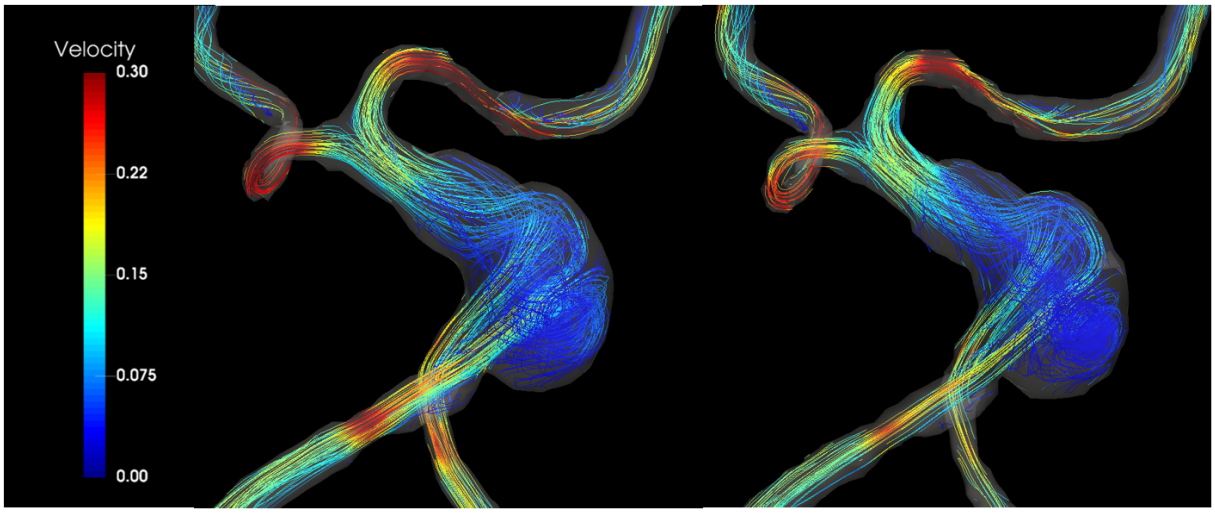

Figure 3.6: Comparison of streamlines for two 4D-MR results. (*Left*) Taken at the scanner isocenter. (*Right*) 10cm offset from the isocenter. The measured velocities for the 10cm offset data are most noticeably lower in regions of highest velocity.

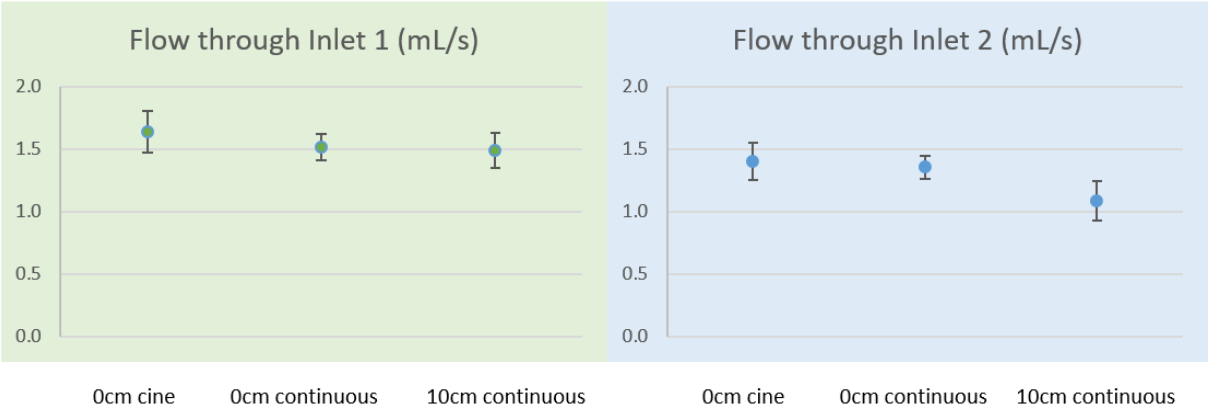

Figure 3.7: Plot of measured flow through each inlet. The standard deviation represents variations in positioning along the vessel centerline.

3.3.2 Comparison of Flow Measurements from 2D and 4D-MR

Table 3.2 depicts the total flow rates measured by three different methods. Both 4D-MR and 2D-MR appear to overestimate the flow relative to the true flow rate. The standard deviation between 2D and 4D-MR are comparable, though the number of slices used to obtain the average flow rate is much greater for 4D-MR than for the 2D-MR acquisition (about 30 vs. 5).

	Measured	2D	4D
Inlet1		1.95 ± 0.09	2.04 ± 0.06
Inlet2		2.07 ± 0.11	1.6 ± 0.13
Total	3.1	4.03 ± 0.14	3.64 ± 0.14

Table 3.2: Flow rates in units of mLs^{-1} obtained from 2D and 4D-MR data and compared to the flow rate directly measured using a graduated cylinder and stopwatch, which is assumed to be the ground truth.

3.3.3 Comparison of 4D-MR vs CFD

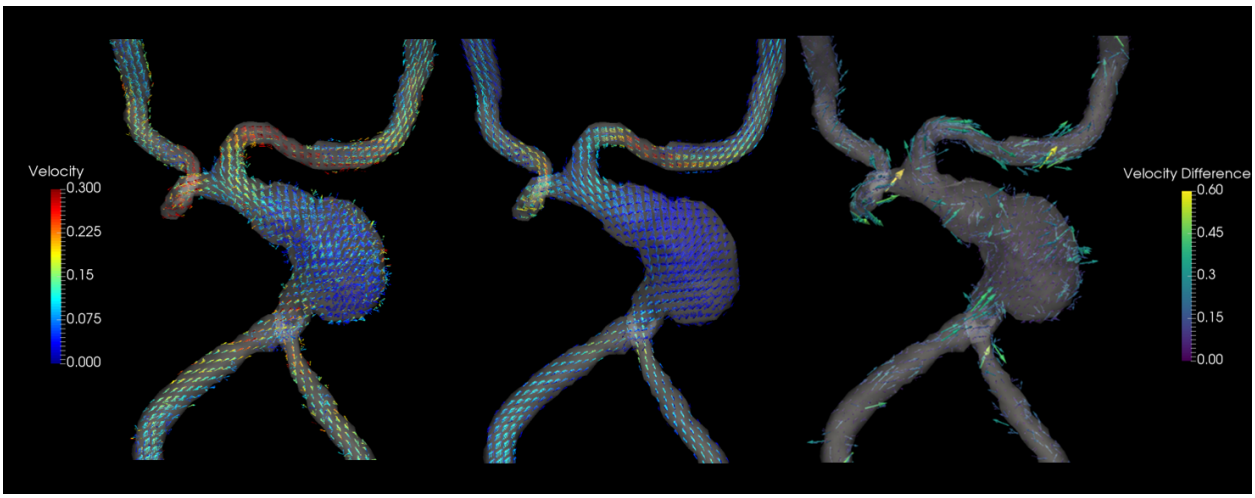

Figure 3.8: Comparison of velocity fields between 4D-MR data taken at 0cm offset and CFD results using the inflow rates and flow ratios specified by Simulation 1 in 3.1. (*Left*) 4D-MR velocity field. (*Middle*) CFD velocity field. (*Right*) Vector velocity difference map.

Figure 3.8 compares the 4D-MR derived velocity field to simulation results run using 4D-MR extracted flow ratios and the true flow rate of 3.1 mLs^{-1}. Overall, the velocities found from the CFD simulations were much lower, which is to be expected,

since the true total flow rate is lower than the rate determined from 4D-MR (3.61 mLs^{-1}). Additionally, we see from the velocity difference vector map that the 4D-MR and CFD data disagree most strongly at the vessel walls.

3.3.4 Effect of flow error on WSS

Figures 3.9 and 3.10 show the streamlines and WSS distribution patterns for a set of simulations in order of *decreasing* total flow, as well as the corresponding regions of low WSS. Table 3.3 quantitatively presents the areas of low WSS for each inflow condition and the changes to those values relative to the measured condition. As expected, overall WSS decreases with decreasing flow. A change of about 17% in the total flow leads to a change of about 12% in the total area of low WSS.

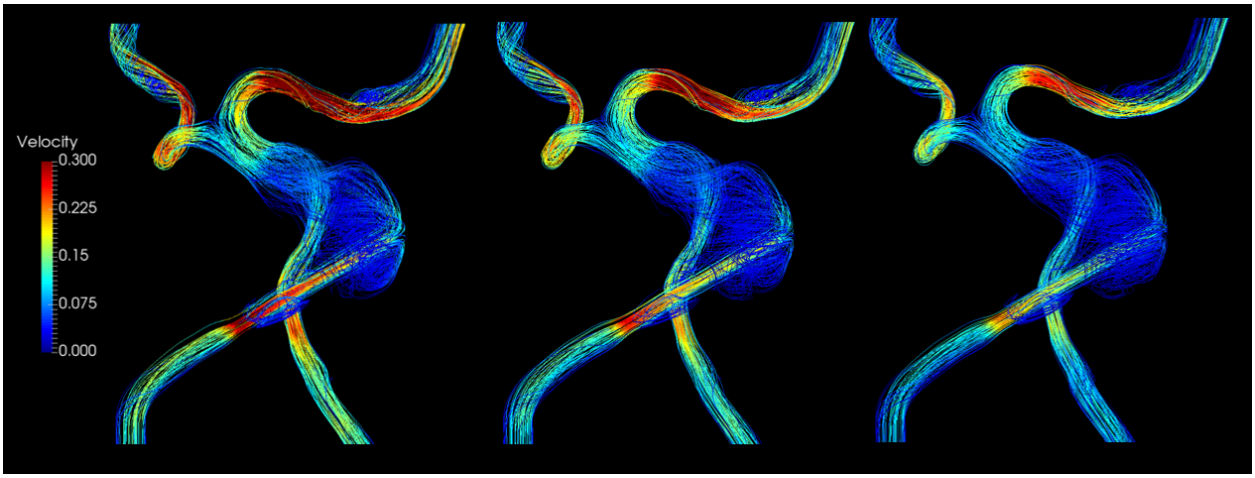

Figure 3.9: Streamlines of simulations shown in order of decreasing total flow from left to right, with the flow ratio between the two inlets kept constant. The flow rates applied can be found in Table 3.3.

Figures 3.11 and 3.12 show the streamlines and WSS distribution patterns for a set of simulations that varied inlet flow ratio, holding the total flow constant. Table 3.4 presents the changes in area of low WSS relative to the measured condition. However, due to offsetting contributions from the two jets, the overall $A_{\text{low WSS}}$ remains almost the same for the simulation conditions. Instead, it is more appropriate to look at the regions that remained classified as low WSS for all simulated conditions, as presented in Figure 3.13 and Table 3.5.

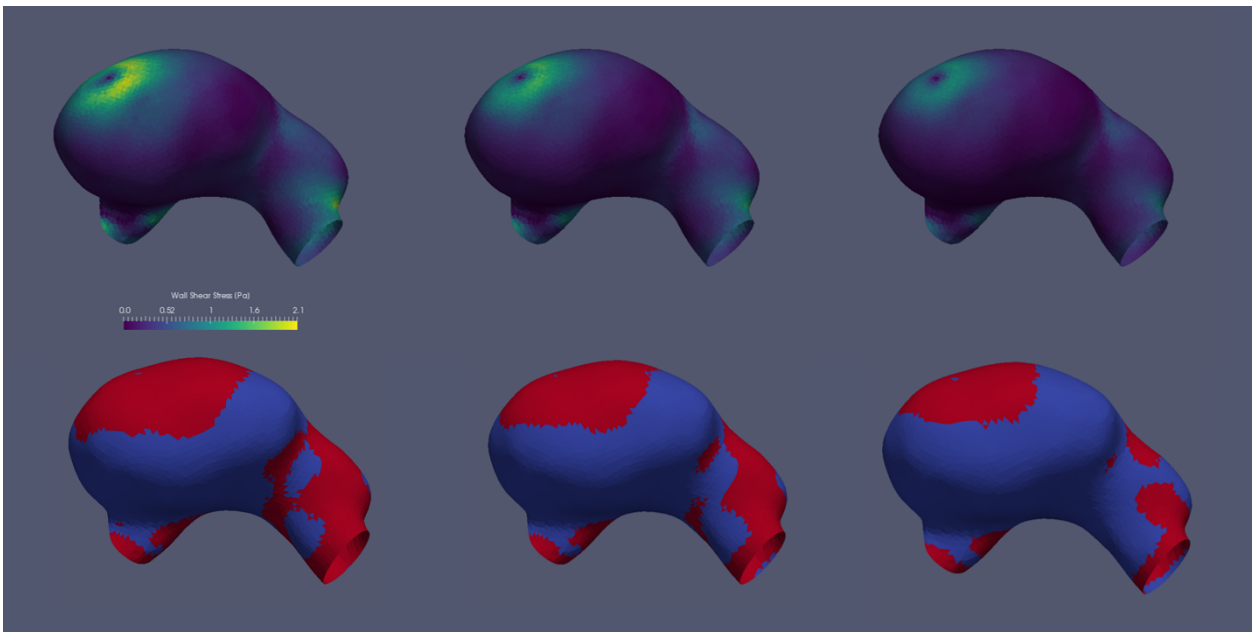

Figure 3.10: WSS distributions and regions of low WSS (blue) for simulations in order of decreasing total flow from left to right, corresponding to the flow patterns displayed in Figure 3.9. (*Top Row*) WSS distributions. (*Bottom Row*) Binary separation in areas of low and non-low WSS.

Condition	Flow (mLs^{-1})	ΔFlow (%)	$A_{\text{low WSS}}$ (mm)	$A_{\text{low WSS}}/A_{\text{Total}}$	ΔArea (%)
Low	2.58	-17.4	997.0	.816	12.1
Measured	3.10		888.7	.728	
High	3.64	17.4	789.9	.646	-11.3

Table 3.3: Changes in the total area low WSS ($A_{\text{low WSS}}$) as a result of changes in Total Flow.

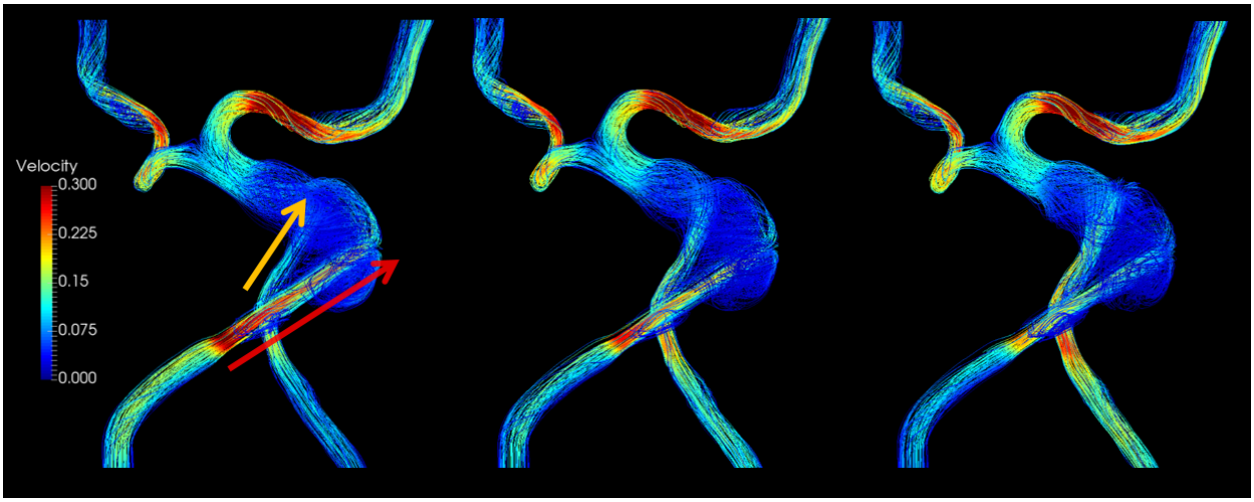

Figure 3.11: Streamlines for simulations with varying flow ratio, in order of decreasing flow through "Inlet 1", represented by the red arrow, and increasing flow through "Inlet 2", represented by the orange arrow.

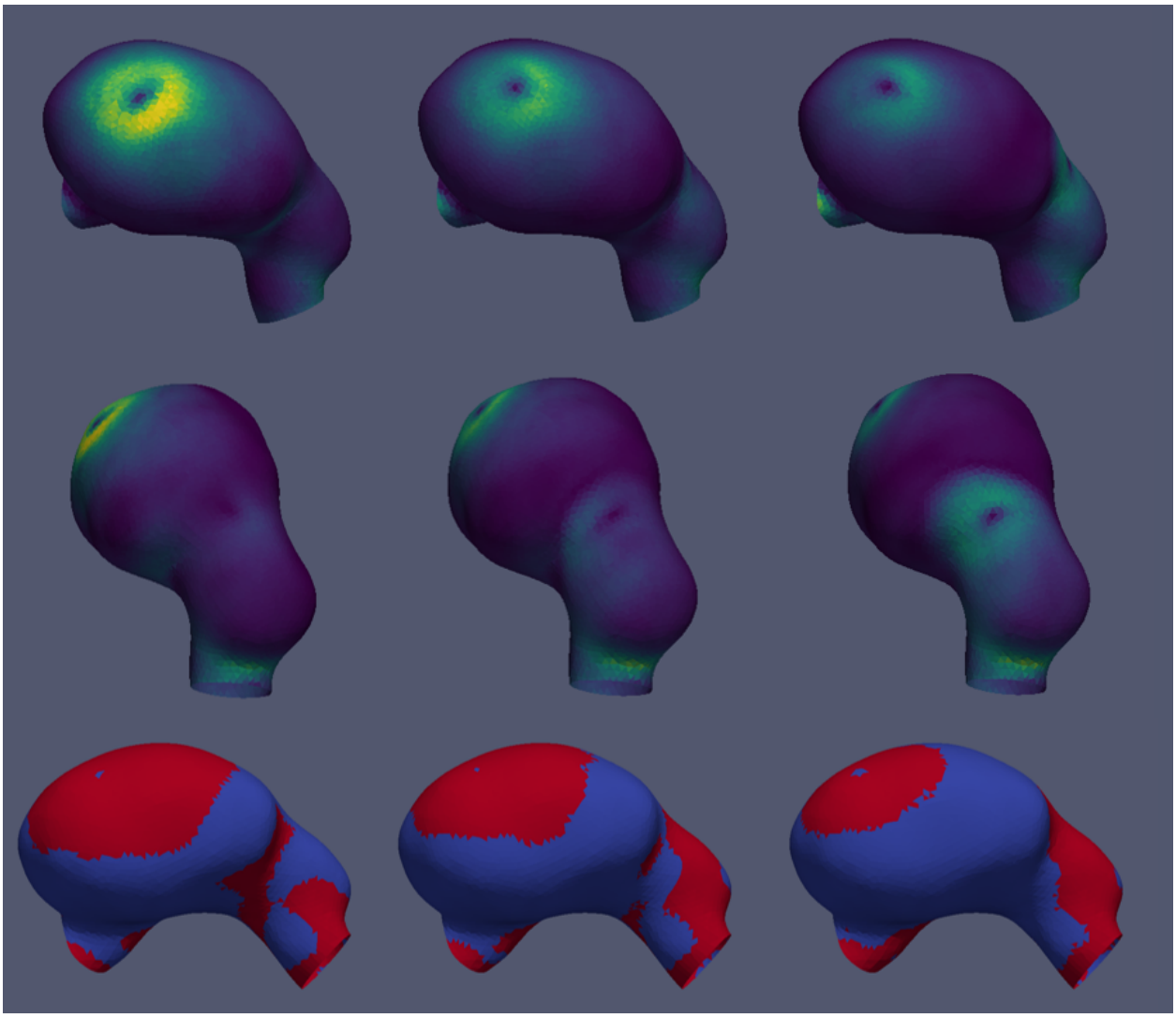

Figure 3.12: WSS patterns for simulations with varyiing flow ratio, in order of decreasing flow through "Inlet 1", corresponding to the streamlines in Figure 3.11. (*Top Row*) WSS distribution on the anuerysm wall, with the perspective focused on the impingement zone related to the jet incoming from Inlet 1. (*Middle Row*) WSS distribution on the aneurysm wall, with the perspective focused on the impingement zone related to the jet incoming from Inlet 2. (*Bottom Row*) Aneurysm wall separated into regions of low WSS and non-low WSS.

Condition	$\frac{Q_1}{Q_1+Q_2}$	$A_{\text{low WSS}}$ (mm)	$A_{\text{low WSS}}/A_{\text{Total}}$	ΔArea (%)
Low	0.46	899.8	0.736	1.2
Measured	0.56	888.7	0.727	
High	0.66	865.0	0.708	-2.7

Table 3.4: Changes in total $A_{\text{low WSS}}$ as a result of changes in the flow ratio between the two inlets.

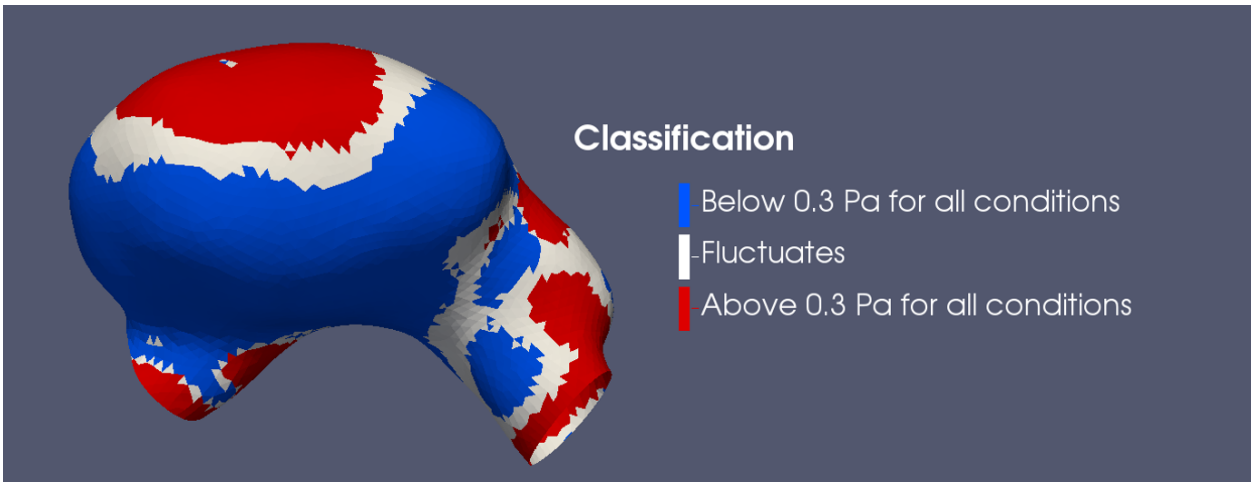

Figure 3.13: Classification of regions of WSS based on the set of simulations with varying flow ratio inlet boundary conditions.

Classification	Area (mm)	Area/Total
Below 0.3 Pa for all simulations	734.7	0.601
Above 0.3 Pa for all simulations	184.2	0.151
Fluctuates	303.4	0.248

Table 3.5: Table quantifying the areas shown in Figure 3.13.

3.4 Discussion

3.4.1 Sources of uncertainty in flow quantifcation

The data provided in Section 3.3 showcase several sources of uncertainty that can affect flow quantification. There appears to be a dependency on the positioning of the subject within the MR scanner due to the spatial variations in the imposed magnetic field. In practice, it is not possible to manipulate a live subject's position or to obtain multiple acquisitions, so if one wants to perform patient-specific studies, they can only estimate this error beforehand using phantoms as we did here. It may be possible to theoretically predict the positional dependence based on the spatial variation of the magnetic fields which is typically not available as it is image sequence dependent, nor is the calculation trivial.

2D-MR flow data is often used over 4D-MR data for flow quantification (and in turn for inflow or outflow boundary conditions in simulations) because the acquisition is much quicker and is generally taken at higher temporal resolution and in-plane resolution. However, here we found that flow rate extraction from 2D-MR data did in fact differ from flow rate obtained from 4D-MR by about 12% and from the true flow rate by about 24%. The low standard deviation relative to the average flow suggests a systemic issue with the flow quantification rather than an issue of accuracy. One possible source of error is scanner miscalibration which may cause MR measurements in this specific case to be greater than the true flow rate.

Another more likely potential source of error is partial voluming, typically at the vessel walls. Partial voluming effects occur because voxels near the wall contain contributions from signal outside the wall, which can provide false velocity magnitudes. Figure 3.8 shows the effect of partial voluming at the vessel walls. These effects can lead to errors in flow quantification and will affect simulations that use flow data for their boundary conditions.

3.4.2 Effect of uncertainty on simulation results

How much the MR flow measurements will affect the simulation results will depend on the aneurysm and the metric in question. Our eventual goal in this instance is to classify aneurysms into growers and non-growers based on the area of low WSS below a certain threshold. Relating growth to raw values of WSS on the aneurysm dome can be challenging, because WSS values have nonlinear dependencies on the geometry and the velocity gradient, which are both subject to errors (the latter of

which was explored here). However, a functional metric like the area of low WSS may be less sensitive to the inaccuracies of MRV.

According to Figures 3.10, 3.12, and 3.13, for the particular aneurym phantom and flow conditions investigated in this study, the fractional area of the aneurysm wall that experiences low WSS remains relatively unchanged (over 60% given a $\pm 15\%$ change in flow and $\pm 10\%$ change in flow ratio through an inlet). However, aneurysms with small or intermediate areas of low WSS may experience greater percentage changes in areas of low WSS with similar uncertainties in inlet flow.

One limitation of this analysis is the use of 0.3 Pa as a specific threshold for low WSS. While the basis for this is based on some preliminary results per Figure 3.4, the relationship to growth has not been established and may not be universal. Instead, future analyses may include the use of algorithms like K-Means Clustering to objectively choose the threshold, which may also limit the effect of potentially inaccurate boundary conditions on the measured area of low WSS.

Chapter 4

Characterization of flow in the cerebral venous outflow tract

A variety of imaging modalities are available to evaluate abnormalities of the intracranial venous circulation, including: CT Angiography; MR Angiography; and catheter-based diagnostic cerebral angiography. These methods afford detailed images of the geometric morphology of veins that are frequently tortuous with highly varying caliber. However, these anatomic studies provide little insight into the flow patterns of blood within these veins. Understanding flow patterns in the cerebral veins could provide important information about the pathophysiology of many clinical conditions.

The overall material, as well as all figure and tables in this chapter were adapted from Kefayati et al., 2017 [31], with permission from Elsevier.

4.1 Introduction

Multiple conditions have been linked to abnormalities in the cerebral venous outflow tract (CVOT) including: Multiple sclerosis (MS) [32][33], pulsatile tinnitus (PT) [50][54][34][35], intracranial hypertension (IIH) [36][37]. However, research has shown these links to be tenuous at best. For instance, some groups refute the association between MS and the internal jugular vein (IJV) [38][40]. Establishing evidence of such a link is challenging in the CVOT due to the broad range of vascular structures and shapes within this territory, making it difficult to correlate anatomy to pathology. Anomalies such as stenoses, diverticula, and fistulas can exist in asymptomatic and otherwise healthy subjects [39].

Previous medical research on the CVOT looked at the flow rates and pulsatility using Doppler ultrasound [41][42] and 4D-MR velocimetry [43][40]. In this chapter, we present work that expands upon MRI studies on the internal jugular vein (IJV) and its surrounding vessels by focusing on the vessel tortuosity and irregularity to categorize subjects into anatomic subgroups. Within each subgroup, a combination of 2D and 4D MR velocimetry is used not only to measure flow but to investigate the secondary flow patterns related to these geometries to provide additional insight and ways to focus research.

4.2 Methods

4.2.1 *in vivo* MR imaging

Subjects were imaged on a Siemens 3T Skyra scanner (Siemens Medical Systems, Erlangen, Germany) with protocols approved by our Instituational Review Board (IRB). To acquire the geometry, contrast-enhanced MR angiograms (CE-MRA) at 0.7mm isotropic resolution were obtained using a Gadolinium-based contrast agent (Gd-DTPA). To ensure that images were acquired at optimal contrast concentration in the vessels of interest, a timing bolus of 2cc Gd-DTPA was injected at 2cc/sec, followed by a 15cc saline flush injected at 2cc/sec. The full-resolution image was obtained using a bolus of 20cc Gd-DTPA injected at 2cc/sec. Parameters for the acquisition were: Matrix = 240 x 320, FOV = 167 x 223 mm^2, slice thickness = 0.7mm, Number of slices = 144, time of acquistion = 34sec.

2D flow data using cardiac-gated PC-MRI was acquired in the sigmoid sinus (SS) and internal jugular vein (IJV) on both the left and right sides. Parameters for the acquistion were: matrix=192 x 256, in-plane resolution = 0.78 x 0.78 mm^2, FOV = 150 x 200, slice thickness = 5mm, phase window >800 ms, VENC = 100cm/s.

4D-MR velocimetry was obtained with prospectively-gated PC-MRI for a total acquisition time of about 10 minutes. Subjects were selected using a VENC of about 100-150 cm/s for all three encoding directions. Parameters for the acquistion were: flip angle=8°, resolution = 1.3 mm^3 isotropic, in-plane matrix = 116 x 176, FOV = 151 x 230 mm^2, Number of slices=24-28, echo:repetition time = 4:80, acceleration factor=3.

4.2.2 Subject Selection

Eight total subjects from 38 were selected for futher analysis, to provide a range of anatomic presentation. All patients signed informed consent. Geometries were categorized into two overlapping groups: Irregular geometries with lumenal abnormalities (diverticula, out-pouchings, stenoses, filling defects) and smooth geometries without lumenal irregularities. The former group included five geometries from five different subjects, while the latter included six geometries from five subjects.

4.2.3 Image post-processing

DICOM images were post-processed using Python-based GUI's implementing the methods described in Chapter 2 including background correction, segmentation, masking, and denoising. Paraview (Kitware, Clifton Park, NY) was used to create streamline visualizations. Osirix (Pixmeo, Bernex, Switzerland) was used to obtain maximum intensity projections (MIP) from CE-MRA images.

For flow patterns derived from the smooth anatomy group, the helicity index (HI) was calculated:

$$HI = \frac{\mathbf{v} \cdot \boldsymbol{\omega}}{\|\mathbf{v}\|\|\boldsymbol{\omega}\|} \tag{4.1}$$

where $\mathbf{v}$ is velocity and $\boldsymbol{\omega}$ is the vorticity ($\nabla \times \mathbf{v}$).

$\|HI\| = 1$ represents flow that is equally axial and rotational. $HI = 0$ for purely straight flow and pure vortices (when $\boldsymbol{\omega}$ is perpendicular to $\mathbf{v}$). Therefore "tighter", more vortical flow correlates with lower HI. However, this may be counter-intuitive. Hence, the helical pitch ($HP = HI_{mean}^{-1}$) is used instead to quantify the overall intensity of vortex flow, where HI_{mean} includes the values of the HI found within the vessel of interest.

4.3 Results

4.3.1 2D flow analysis

Figure 4.1 shows the 2D PC-MRI-derived flow profiles of three subjects at four locations: Left SS, right SS, left IJV, and right IJV. Table 4.1 shows the corresponding mean flow rates and pulsatility indexes ($(Q_{max} - Q_{min})/Q_{mean}$). Flow and pulsatility within the CVOT can vary considerably between subjects. For instance, Subject H

exhibits high pulsatility in the right IJV (about 3-13 mLs^{-1}), while Subject C at the corresponding location exhibits relatively low pulsatility (3-5 mLs^{-1}).

Flow and pulsatility can vary markedly along the CVOT within the same subject. Referencing Subject H again, we see that flow in the right SS remains relatively constant at about 5 mLs^{-1} in contrast to the highly pulsatile flow in the right IJV directly downstream. Additionally, Subjects G and H demonstrate clear flow dominance of the right side over the left, but in Subject C, dominance is ambiguous; there are also other subjects (not shown) in which flow mainly drains on the left side.

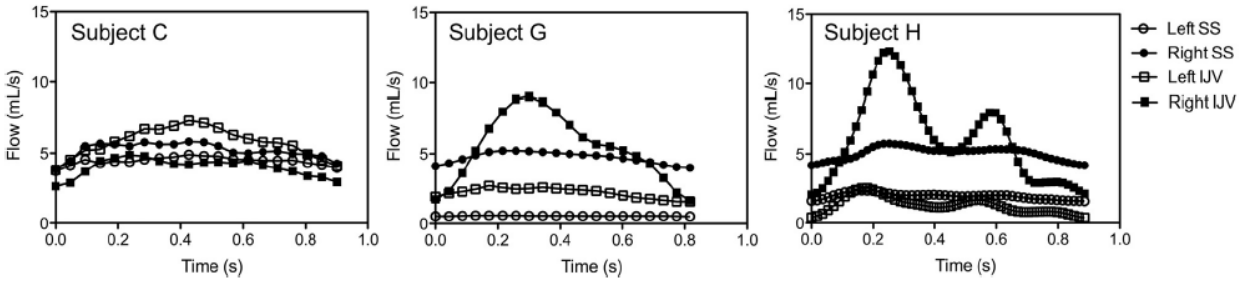

Figure 4.1: Flow profiles in the left and right CVOT derived from 2D-PC-MRI in three subjects.

	Mean Flow (mLs^{-1})				Pulsatility Index			
	LIJV	RIJV	LSS	RSS	LIJV	RIJV	LSS	RSS
Subject C	5.77	3.99	4.44	5.20	0.61	0.56	0.26	0.38
Subject G	2.21	5.41	0.55	4.72	0.52	1.37	0.13	0.26
Subject H	1.30	6.00	1.95	5.04	1.64	1.72	0.40	0.31

Table 4.1: Mean Flow and Pulsatility Index ($(Q_{max} - Q_{min})/Q_{mean}$) derived from the flow profiles in Figure 4.1.

4.3.2 Categorization of jugular geometries

Cerebral venous geometries can be first categorized by the presence or absense of lumenal abnormalities, such as stenoses and diverticula. These abnormalities can vary in location and severely disturb the mainstream flow by creating sharp jets or diverting flow into recirculation zones; such geometries can be broadly described as "irregular". By comparison, geometries that lack abnormalities can be generally described as "smooth". However, it is important to note that the two groups are not necessarily mutually exclusive. For example, a particularly common geometric

configuration can involve an upstream stenosis and diverticulum in the SS, while the IJV remains smooth.

4.3.2.1 Flow in smooth geometries

Figure 4.2 shows six smooth IJV geometries from five different subjects, which are ordered from left to right by increasing elevation of the jugular bulb relative to the sigmoid sinus. Figure 4.3 shows the corresponding streamlines representing flow within these geometries. There appears to be a correlation between jugular bulb height and the streamline helicity, which is emphasized in Figure 4.4 and quantified by the helical pitch.

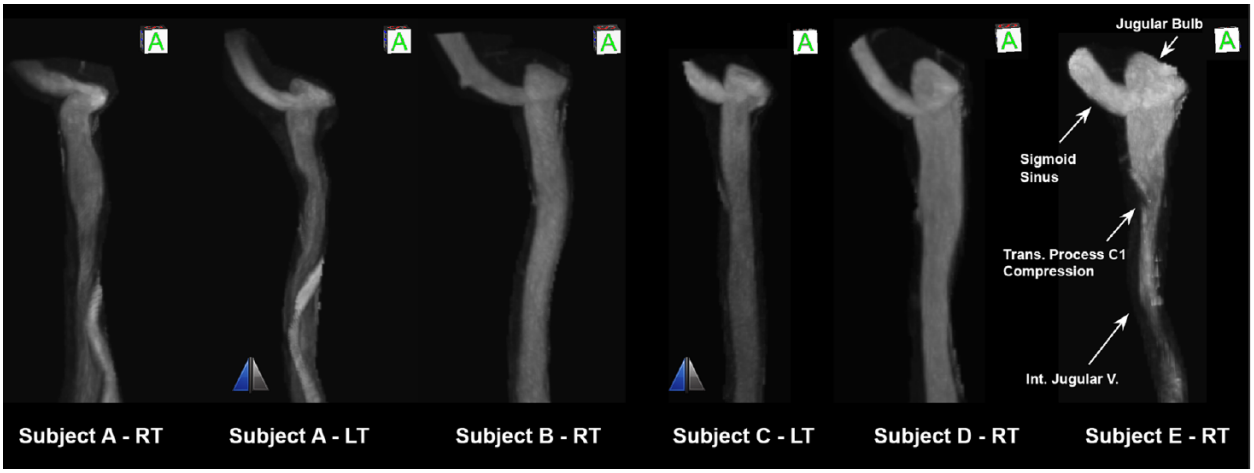

Figure 4.2: Maximum intensity projection (MIP) images of the IJV in smooth geometries.

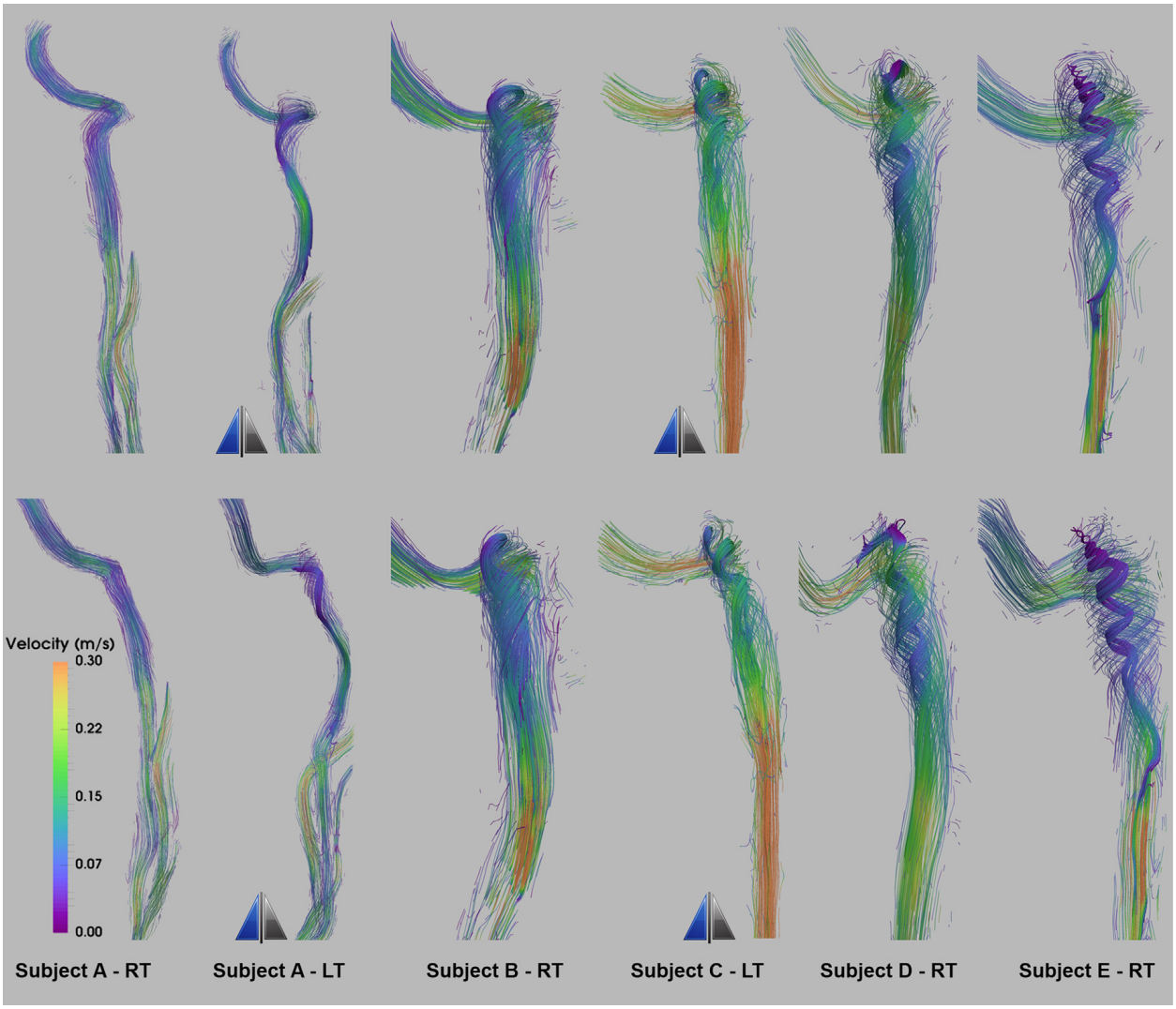

Figure 4.3: Streamlines corresponding to the geometries in Figure 4.2

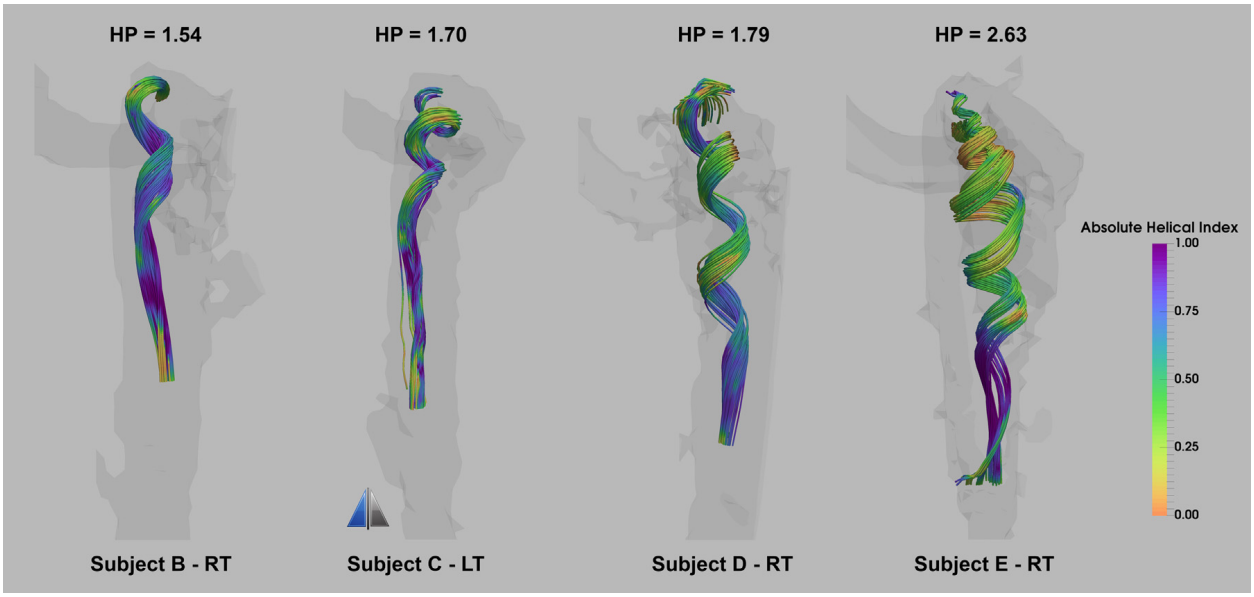

Figure 4.4: Selected streamlines emphasizing the shape of the vortical flow within the IJV for the latter four subjects from Figure 4.2. The degree of helical tightness is quantified by the helical pitch (HP).

4.3.2.2 Flow in irregular geometries

Figure 4.5 shows five irregular cerebral venous geometries with various lumenal abnormalities, while Figure 4.6 presents their corresponding velocity streamlines. Subject B has a diverticulum on the jugular bulb at the superior aspect of the IJV. In effect, it elevates the jugular bulb, producing a similar helical pattern to those found in Figures 4.3 and 4.4. Subject F has multiple diverticula on the jugular bulb, which results in a complex pattern involving multiple intersecting and interactive vortex cores.

Subjects G and H exhibit a stenosis in the SS, followed closely downstream by a diverticulum at the bend. This results in an upstream jet that pushes flow into the diverticulum. Despite the similar locations of their abnormalities, the flow patterns between Subject G and H in the upstream SS are still considerably different due to the differences in the shape of their diverticula; the divertculum of Subject G is flatter than that of Subject H, leading to more planar vortex flow. Subject G also has a filling defect due to an arachnoid granulation (protusions from the subarachnoid space that encompasses the brain into the space outside the skull). This splits the flow into two jets.

Subject C is characterized by a particularly prominent condylar vein, which typically drains blood from the IJV at the jugular bulb. As a result, most flow is instead directed through the condylar vein instead of the IJV, leading to a helical flow perpendicular to the IJV.

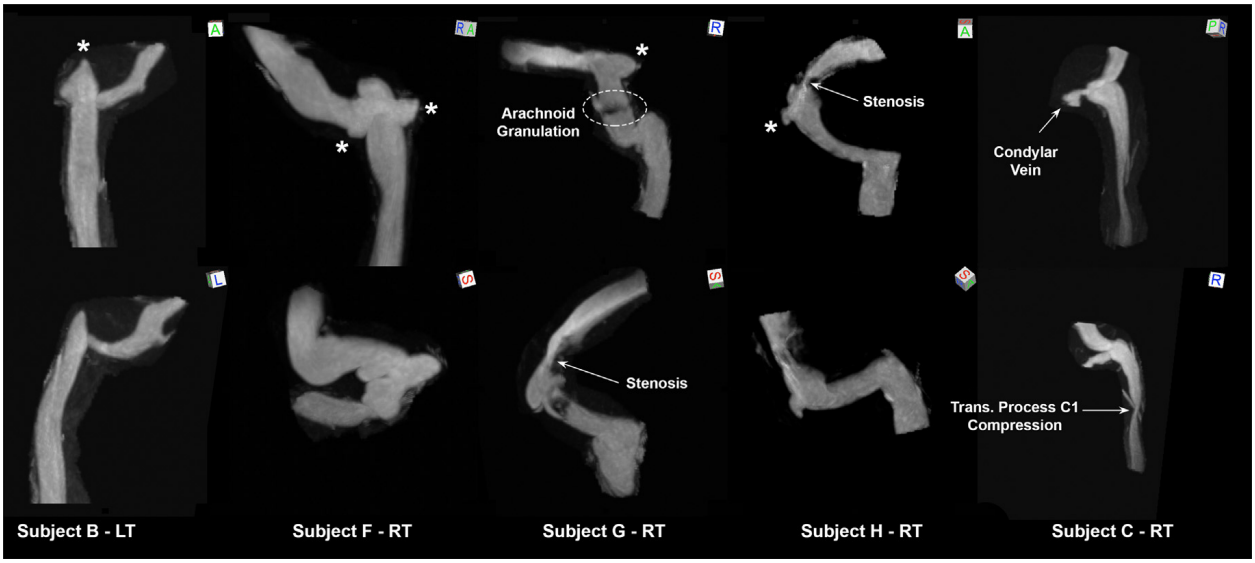

Figure 4.5: MIP images of irregular geometries of the CVOT.

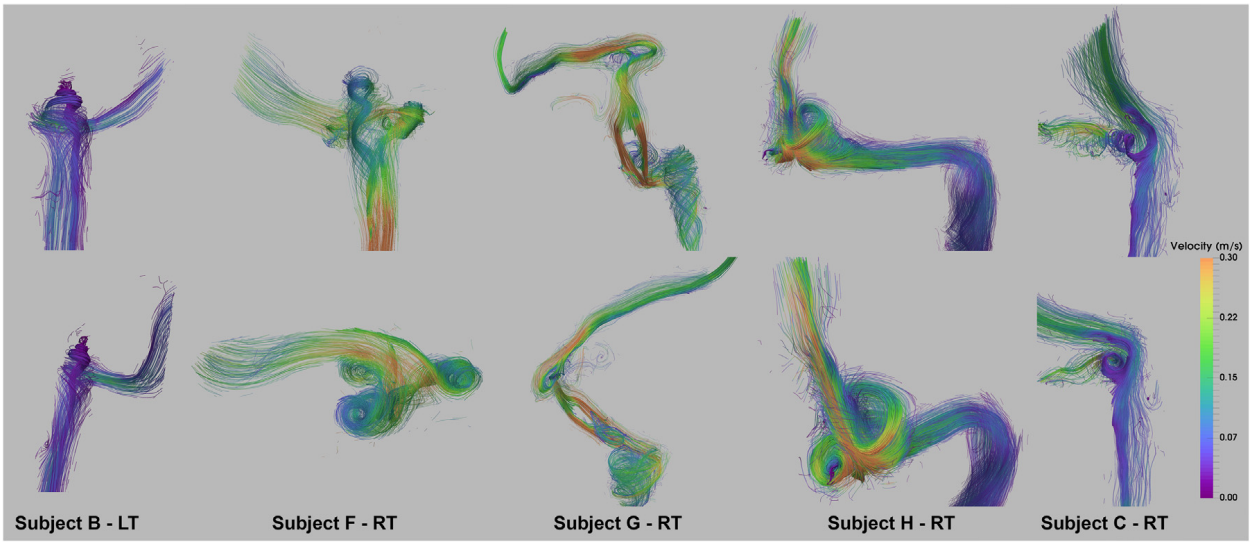

Figure 4.6: Streamlines corresponding to the geometries in Figure 4.5.

4.4 Discussion

The extreme variance of flow data in the CVOT obtained using 2D PC-MRI (Figure 4.1, Table 4.1) suggests the need for richer data sets using 4D PC-MRI to properly analyze flow within these vascular territories. The SS directly drains into the IJV, but flow is apparently not conserved, reflecting the presence of branch vessels. Whether flow increases or decreases and by how much also varies from person to person, likely due to unpredictable patterns of accessory veins that drain from or feed into the IJV; these accessory veins are unfortunately very difficult to capture using MRI under conventional spatial resolutions. The flow volume and pulsatility is also complicated by the high venous compliance, wave reflections, and expansion resistance from the surrounding bone and tissue. Furthermore, flow in the venous return is known to be mediated by respiratory pressure variation. Additionally, the vortex patterns are difficult to capture with 2D-flow, which has low resolution in the through-plane direction, and which would require prohibitively long and complicated acquisitions.

The helical flow pattern and its relationship to elevated jugular bulbs is tentatively connected to pulsatile tinnitus (PT) by both indirect observation (correlating the presence of elevated bulbs with the presence of PT) and direct observation (successful surgical treatment on cerebral venous abnormalities in PT patients). This relationship between geometry, flow, and symptom is examined in more detail in Chapter 5 using CFD.

The correlation between the sinus stenosis and sinus diverticulum as exhibited in Subjects G and H in Figures 4.5 and 4.6 (as well as other subjects not pictured here) suggest a potential site of vessel remodeling. It is possible that constant dynamic pressure from the jet resulting from the stenosis onto the sinus vessel wall may lead to development of the diverticulum, though this link is entirely speculative.

Stenoses in the SS are thought to be related to idiopathic intracranial hypertension (IIH), though it is unclear as to whether it is a symptom or a cause, especially because many subjects with sinus stenoses remain asymptomatic. An examination of anatomy alone is unlikely to distinguish pathological sinus stenoses from benign ones. Advances in 4D-Flow MRI analysis which allow the derivation of pressure, WSS, and turbulence from the measured velocity field may help provide additional insight.

Chapter 5

Flow patterns in the jugular veins of patients with pulsatile tinnitus

Extending upon our exploration of jugular venous pathophysiology and flow in Chapter 4, we explore a possible association between flow patterns and a specific symptom, pulsatile tinnitus (PT). We focus specifically on jugular bulb geometries (Section 4.3.2.1) and their potential as a source of sound generation in PT patients, ignoring "irregular" geometries (Section 4.3.2.2) in order to reduce variations between symptomatic and asymptomatic subject groups.

The text as well as most of the figures and tables in this chapter were adapted from Kao et al., 2017 [44], with permission from Elsevier.

5.1 Introduction

Tinnitus is the auditory perception of sound in the absence of an external source. It affects more than 50 million Americans [54], often severely. It is not uncommon for patients to suffer from insomnia, depression, or even suicidal ideations [52][62]. A small subset, Pulsatile Tinnitus (PT), is pulsatile and is often described as a whooshing sound that is synchronized with the cardiac cycle. PT accounts for 5-10% of tinnitus patients [55][51] and is often related to abnormal flow in vascular structures near the cochlea [54][56]. Vascular structures with aberrant flow can be either venous or arterial. PT etiologies can be venous (40%), arterial (35%), or undetermined (25%) [59].

While controversial, abnormal internal jugular vein (IJV) geometries, such as enlarged or high-riding jugular bulbs (HJB), have been suggested as a source of

pulsatile tinnitus in a subset of patients. A study by Sonmez et al., 2007 [65] found that subset to be roughly 30% of PT patients, though we note that their study did not correlate laterality of PT with the side of the venous abnormality. Case studies by Adler and Ropper, 1986 [46], Buckwalter et al., 1983 [48] and Chandler, 1983 [49] proposed that blood flow through the anatomic aberration may contribute to PT. Patients reported changes in PT with changes in flow through the jugular vein; for example, decreased flow with ipsilateral neck compression led to decreased symptoms, while increased flow in high-flow states (e.g. exercise or pregnancy) has been linked to increased pulsatile tinnitus strength [48].

Despite those observations, we emphasize that an association between PT and abnormal jugular bulbs is only tentative. Both Buckwalter et al., 1983 and Chandler, 1983 promoted jugular vein ligation as a treatment for PT, which has since been determined ineffective [53]. Additionally, the presence of a HJB alone is not itself predictive of PT; Marsot-Dupuch, 2001 [58] determined that only 4.5% of patients with an enlarged jugular bulb present PT in their late adult life, while Park et al., 2015 found that in a large patient population, selected for afflictions not limited to PT, about 35% of their jugular veins had HJB [61]. The ambiguity of the role of abnormal jugular vein geometries and flow rate in PT pathology suggests that a link between flow, shape, and sound, if it exists, must be complex; simply observing the flow rate and bulb shape is not enough to identify the origin of venous PT.

This study was motivated by our preliminary observations of complex flow patterns within the jugular vein [45][31]. Those studies reveal a pronounced vortex core surrounded by a peripheral circulating flow pattern (Figure 5.1). Similar geometries and flow patterns have been noted by others to be a source of sound [68]. We believe more detailed and subcategorized analyses are needed to define the relationship between the morphology of the cerebral venous system and flow patterns which in turn may help elucidate the source of PT.

Bony structures overlying the draining veins limits the use of Doppler Ultrasound, the conventional *in vivo* approach for measuring velocities. MR velocimetry overcomes this limitation and is able to define the full velocity vector in three-dimensional space through the pulsatile cycle - a method referred to as 4D MR Velocimetry (4D MRV) [57][60]. 4D MRV has been explored in application to the cerebral venous sinuses in both *in vivo* and *in vitro* models. However, 4D MRV is restricted in both spatial and temporal resolution. Furthermore, *in vivo* measurement only evaluates the specific physiologic condition presenting at time of examination, and cannot readily explore flow field variations in response to different physiological

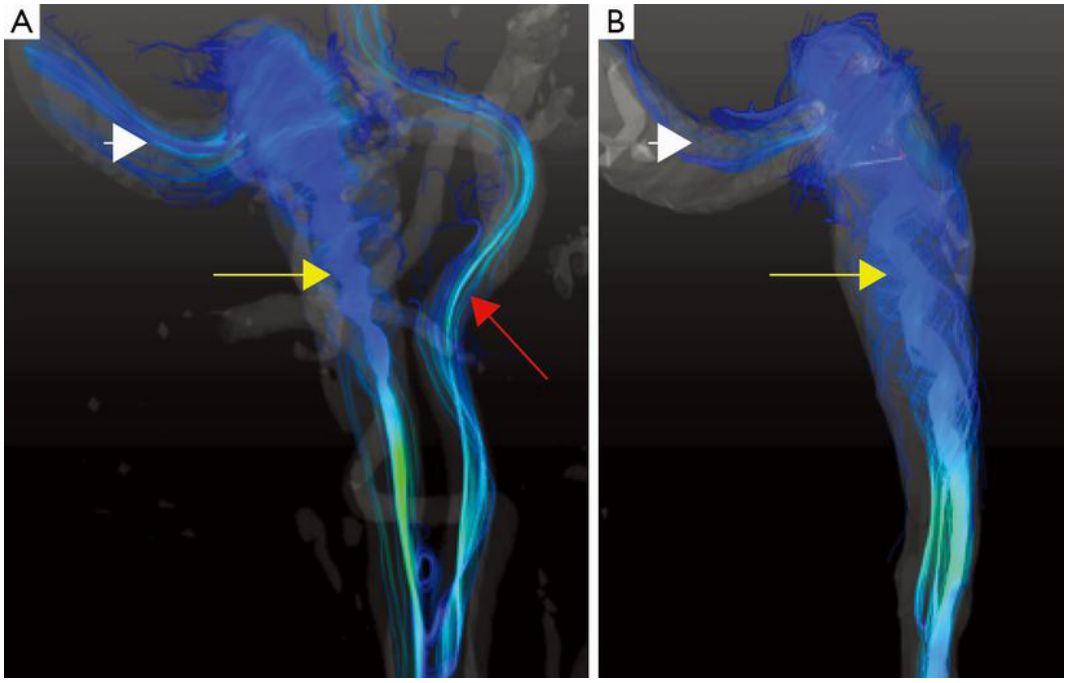

Figure 5.1: Streamlines representing *in vivo* flow within the jugular vein (reprinted from [45] with permission from AME Publishing Company).

conditions, such as heart rate or exercise, that might alter total volume flow.

Compared to *in vivo* MRV, Computational Fluid Dynamics (CFD) provides higher spatial and temporal resolution, and parameters can be adjusted to explore physiologic limits. We therefore employed CFD to provide controlled simulations in the complex anatomic geometries of the transverse sinus (TS), SS, and IJV. This work utilized subject-specific CFD based on lumenal geometries, from contrast-enhanced MR Venography, and inlet flow waveforms, from 2D through-plane MR velocimetry, measured for each individual. As a starting point, we investigated the relationship between jugular geometry and flow by comparing the velocity fields in "elevated" jugular bulbs, which were prevalent in our symptomatic population, to those in "rounded" bulbs, which were prevalent in our asymptomatic subjects.

5.2 Methods

5.2.1 Subject Recruitment

Subjects were recruited from the UCSF Pulsatile Tinnitus Clinic and provided informed consent for participation in accordance with the procedures approved by our Institutional Review Board. Subjects with unrelated pathology known to cause PT were excluded (Table 5.1).

5.2.2 Image Acquisition

All imaging was performed on a 3T Siemens Skyra (Siemens Medical Systems, Erlangen, Germany) and consisted of a high resolution MR venogram to define the venous lumenal geometry, and MR flow studies to define the inlet volume flow through each sigmoid sinus.

The MR venograph consisted of a large volume 3D Contrast-Enhanced MR Angiography (CE-MRA) study acquired at 0.7mm isotropic resolution. A timing run using a 2cc bolus of GdDTPA delivered at 2cc s^{-1} followed by a 15cc saline flush at 2cc s^{-1} was performed. Injection was initiated simultaneously with low-resolution 3D volume studies acquisition at 1 second intervals. The time delay, $\mathbf{T_{delay}}$, between injection and arrival of the contrast in the jugular vein was determined from visual inspection of the resulting maximum intensity projection images. The full contrast bolus of 20cc Gd followed by a 15cc saline flush, all injected at 2cc s^{-1}, was then delivered and the high-resolution 3D CE-MRA was acquired beginning at $\mathbf{T_{delay}}$ after the start of injection. The 3D volume consisted of a coronal slab, 124 mm thick using a total acquisition time of 45 seconds. Imaging parameters were: TR = 3.66 s; TE = 1.4 s; Flip angle = 20°; FOV = 200 mm; Matrix = 320 x 240; number of slices = 172; acceleration factor = 3.

Inlet flow waveforms were measured using retrospective, pulse gated, 2D Phase-Contrast (PC)-MR Velocimetry. Through-plane velocities were measured for planes prescribed transverse to each sigmoid sinus. Parameters of the 2D PC MR were: slice thickness = 5 mm; TR = 37 s; TE = 3.6 ms; Flip angle = 20; cardiac phase length = 40 ms; VENC = 100 cm s^{-1}; FOV = 200 mm; Matrix = 256 x 154; acceleration factor = 2.

5.2.3 Jugular Bulb Classification

The geometry of each subject's jugular bulb on the symptomatic side was classified by a board certified Neuroradiologist. In symptomatic patients the index side was defined as the side where symptoms of PT were most acutely perceived. For the asymptomatic "control" subjects, the index side was defined as that of the dominant draining vein based on mean flow measured by 2D PC MR. The geometry was categorized as either "elevated" or "rounded" (Figure 5.2). "Elevated" was defined as the apex of the jugular bulb raised above the level of the sigmoid sinus at its inlet into the jugular vein, whereas "rounded" was defined by the absence of any pronounced ascent in the proximal jugular bulb and a smoother transition into the jugular vein. We note that our definition for elevated geometries does not follow the standard clinical definition for HJB. When assignment to one of those two categories was ambiguous, the anatomy was categorized as "neither".

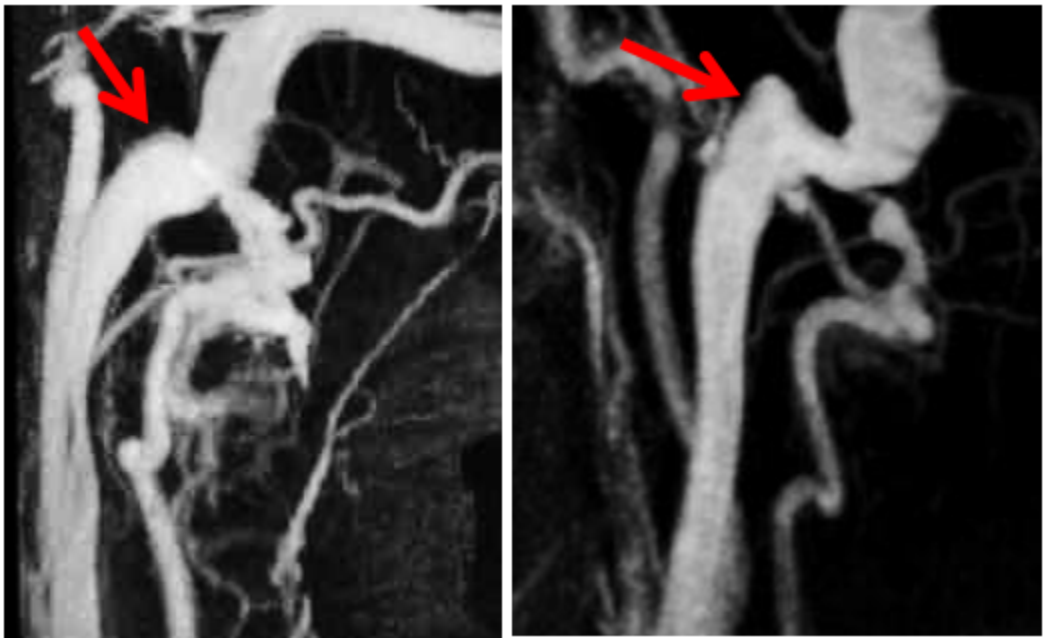

Figure 5.2: MIP images of the vasculature around the internal jugular vein. The arrows point to the geometry of interest, the jugular bulb, for a rounded bulb (*Left*) and a raised bulb (*Right*).

5.2.4 Simulation

For each subject, a surface representation of the SS and IJV from the relevant side was segmented from the CE-MRA data using the Vascular Modeling Toolkit (VMTK)

	Subjects	Controls
Known underlying PT pathology	2	0
Deafness	1	0
Neither	6	0
Elevated	3	1
Rounded	0	3
Total Recruited	*12*	*4*

Table 5.1: Number of subjects recruited and the distributions into subgroups. Only the subgroups shaded in green (Elevated, Rounded) were included in the CFD analysis and compared to one another.

(Orobix, Bergamo, Italy) and Geomagic Design X (Geomagic, Rock Hill, USA). Flow extensions were provided at the inlets (the entrance to the sigmoid sinus) to ensure developed flow. Tetrahedral meshes from the surfaces were generated (also in VMTK) with a targeted edgelength of 0.6mm, resulting in meshes of approximately 200,000 nodes and 1,000,000 cells. The edgelength was chosen by repeating simulations for edgelengths varying from 0.4mm to 1.0mm for one selected jugular geometry. Flowfields were unchanged for values less than 0.6mm and that was then used in subsequent simulations.

Simulations were performed using FLUENT (ANSYS, Canonsburg, USA). Assumptions included rigid walls, Newtonian fluid, and laminar flow. A coupled solver was used with second-order pressure and second-order momentum discretization schemes. The fluid material was defined to resemble blood at body temperature, with a density of 1060 kgm^{-3} and a viscosity of 0.0035 $kgm^{-1}s^{-1}$. A zero-pressure condition was prescribed at the outlet. Flow profiles were extracted from the 2D-MRV data using Segment (Medviso AB, Lund, Sweden) [47]. Simulations were performed for pulsatile flow using the measured flow waveform, and for steady flow using the peak flow value for two representative cases from each geometric group. Those results demonstrated that the dominant flow features found for pulsatile flow were noted at peak systole, and that the steady flow simulation reflected the same features. For clarity, we therefore limited our analyses to steady flow at peak systole.

5.2.5 Flow Pattern Analysis

Initial inspection of the velocity fields indicate that the flow patterns of elevated and rounded jugular bulbs differed in the presence and extent of downstream helical flow and by the presentation of vortex cores. In order to visualize the vortex cores, swirling

strength values were calculated throughout the volume and displayed in Paraview (Kitware, New York, USA). The flows were quantified by calculating the length-averaged streamline curvatures within the proximal jugular vein to provide a well-defined single parameter indicative of flow shape.

The streamlines were generated forwards and backwards in time and visualized in Paraview, using seed points dispersed throughout the geometry. For each streamline, the curvature at each point was numerically calculated according to

$$\kappa = \left\| \frac{\partial \mathbf{T}}{\partial s} \right\| \tag{5.1}$$

where the curvature κ, is defined as the derivative of the tangent vector $\mathbf{T}$ with respect to the line's parameterization s. Streamlines were manually cut to a region of interest of approximately 1.5 cm along the length of the vessel's centerline that included the jugular bulb and the proximal jugular vein (Figure 5.3).

The length-averaged streamline curvatures were then calculated as

$$C = \frac{1}{L} \sum_{i}^{N} \int_{l_i} \kappa_i(s) ds, \quad L = \sum_{i}^{N} l_i \tag{5.2}$$

where the curvatures for all streamlines are integrated with respect to length and divided by L, the total length of all streamlines. The number of streamlines N is chosen to provide a value of C that is insensitive to changes in N (Figure 5.4).

5.2.6 Statistical Analysis

Statistical significance between two subject groups was determined using Welch's t-test which is more reliable than the Student's t-test when comparing groups with different sample sizes and variances.

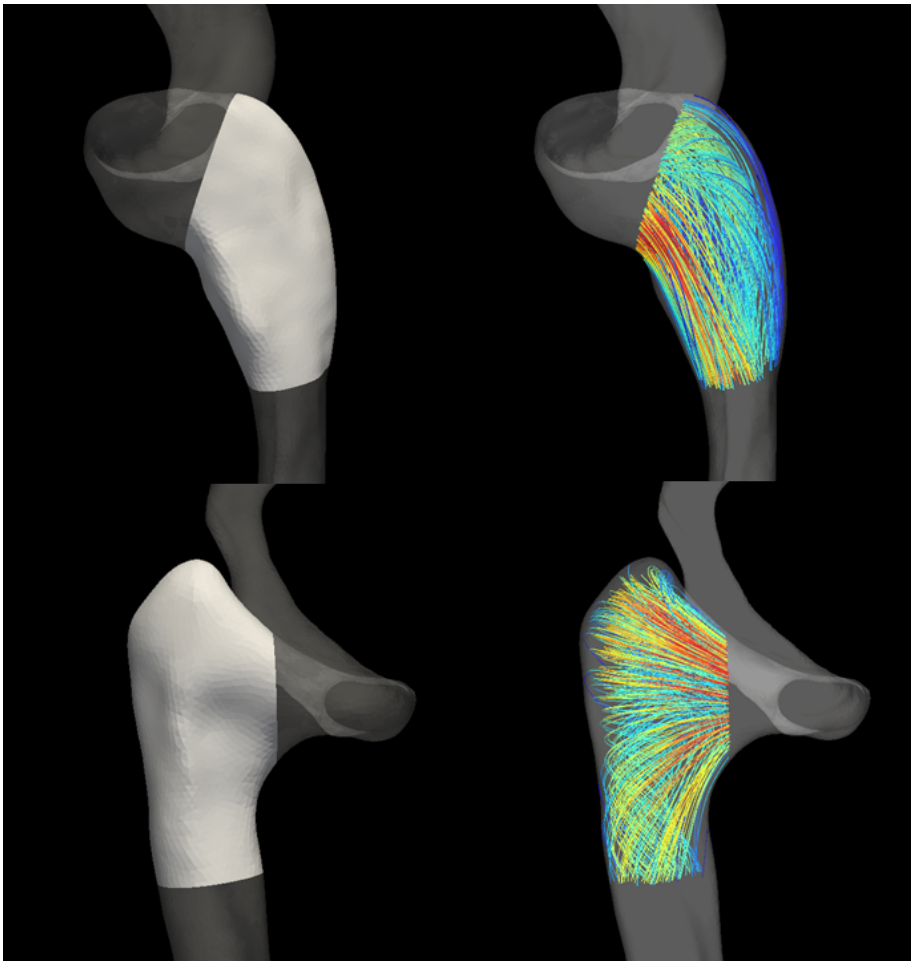

Figure 5.3: Regions from which streamlines were extracted for calculating the length-averaged streamline curvature (about 1.5 cm along the centerline). These regions were carefully chosen to include only the flow within the proximal internal jugular vein. *Top Row*: A rounded bulb geometry. *Bottom Row*: An elevated bulb geometry.

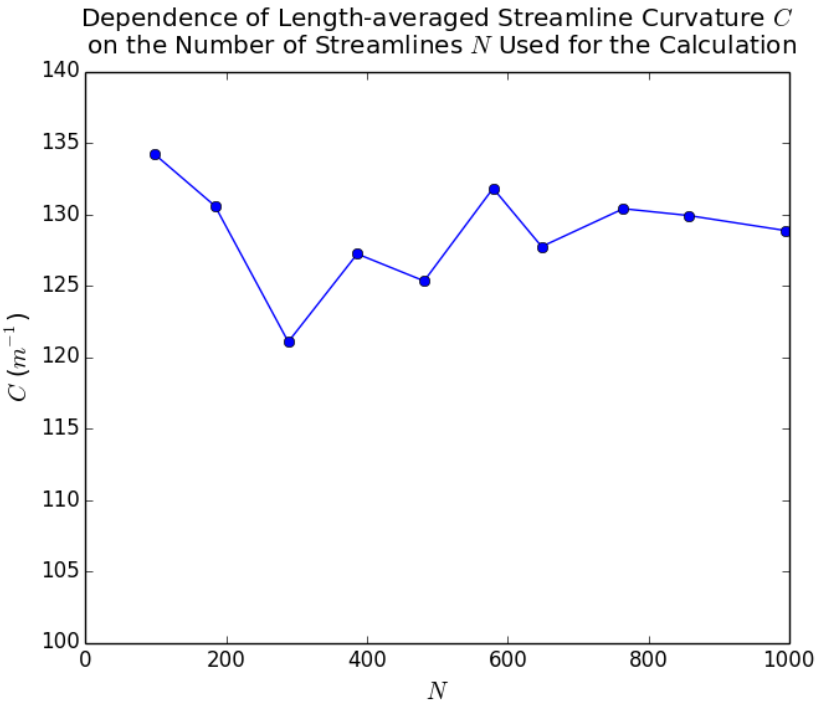

Figure 5.4: Calculated values of C for specific values of N for a single subject. In this study, N was typically chosen to be in the range of 800-1000 in order to reduce the effect that random streamline seed points had on the value of C.

5.3 Results

16 individuals were recruited: 12 subjects who reported symptoms of pulsatile tinnitus and 4 controls. Of the symptomatic subjects, two were excluded due to underlying pathology known to cause PT (namely fistulas and sigmoid sinus diverticulum). One PT patient reported congenital unilateral deafness, and was excluded from further analysis due to inability to reliably lateralize the symptomatic side. Of the remaining nine PT patients, six were classified as having "neither" geometry, three had elevated bulbs, and none had rounded bulbs. Of the four controls, one had elevated bulb and three had rounded bulbs. The numbers for subject exclusion and inclusion as well as the distributions of geometries are summarized in Table 5.1.

Mean and peak flows for the patient and control groups are provided in Table 5.2. Also included are Reynolds numbers calculated at the junction between the sigmoid sinus and the jugular bulb.

	Controls	Subjects	P
Number of Subjects	4	3	
Area (m^2)	$6.47 \pm 3.12 \times 10^{-5}$	$5.91 \pm 2.85 \times 10^{-5}$	
Perimeter (m)	$2.87 \pm 0.78 \times 10^{-3}$	$2.79 \pm 0.81 \times 10^{-3}$	
Hydraulic Diameter (m)	$8.54 \pm 2.53 \times 10^{-3}$	$8.06 \pm 2.15 \times 10^{-3}$	
Mean Flow (mLs^{-1})	4.53 ± 0.74	4.61 ± 2.11	0.953
Peak Flow (mLs^{-1})	5.63 ± 1.26	5.95 ± 2.24	0.834
$\mathrm{Re}_{\mathrm{mean}}$	205 ± 75	199 ± 59	0.914
$\mathrm{Re}_{\mathrm{peak}}$	254 ± 100	267 ± 91	0.871

Table 5.2: A comparison of flow-related parameters between the control and patient groups. Only subjects that were included per Table 1 were used in these calculations. The hydraulic diameter was calculated as 4*Area/Perimeter. P-values show that the mean and systolic flow values as well as the corresponding Reynolds numbers between the two groups were not statistically significant.

5.3.1 Characterizing flow patterns by visualizing vortex cores

Flow patterns for all rounded and elevated geometries are provided in Figures 5.5 and 5.6. Flow patterns in rounded geometries are characterized by a strong component of flow that travels from the sigmoid sinus directly down the center of the proximal jugular vein. Remaining flow that enters from the sigmoid sinus creates prominent vortex cores in the dilated proximal jugular bulb that propagate along the walls of the bulb parallel to the central stream. Those vortex cores typically increase in

strength distally in the jugular vein where the vein narrows. For elevated geometries, the presence of the arch of the jugular bulb above the sigmoid sinus results in a small component of flow being directed to the apex of the jugular bulb that then subsequently spirals down the center of the bulb. The remaining major component of flow enters the proximal jugular vein at a right angle from the sigmoid sinus, creating a large helical flow structure that rotates about the central spiral.

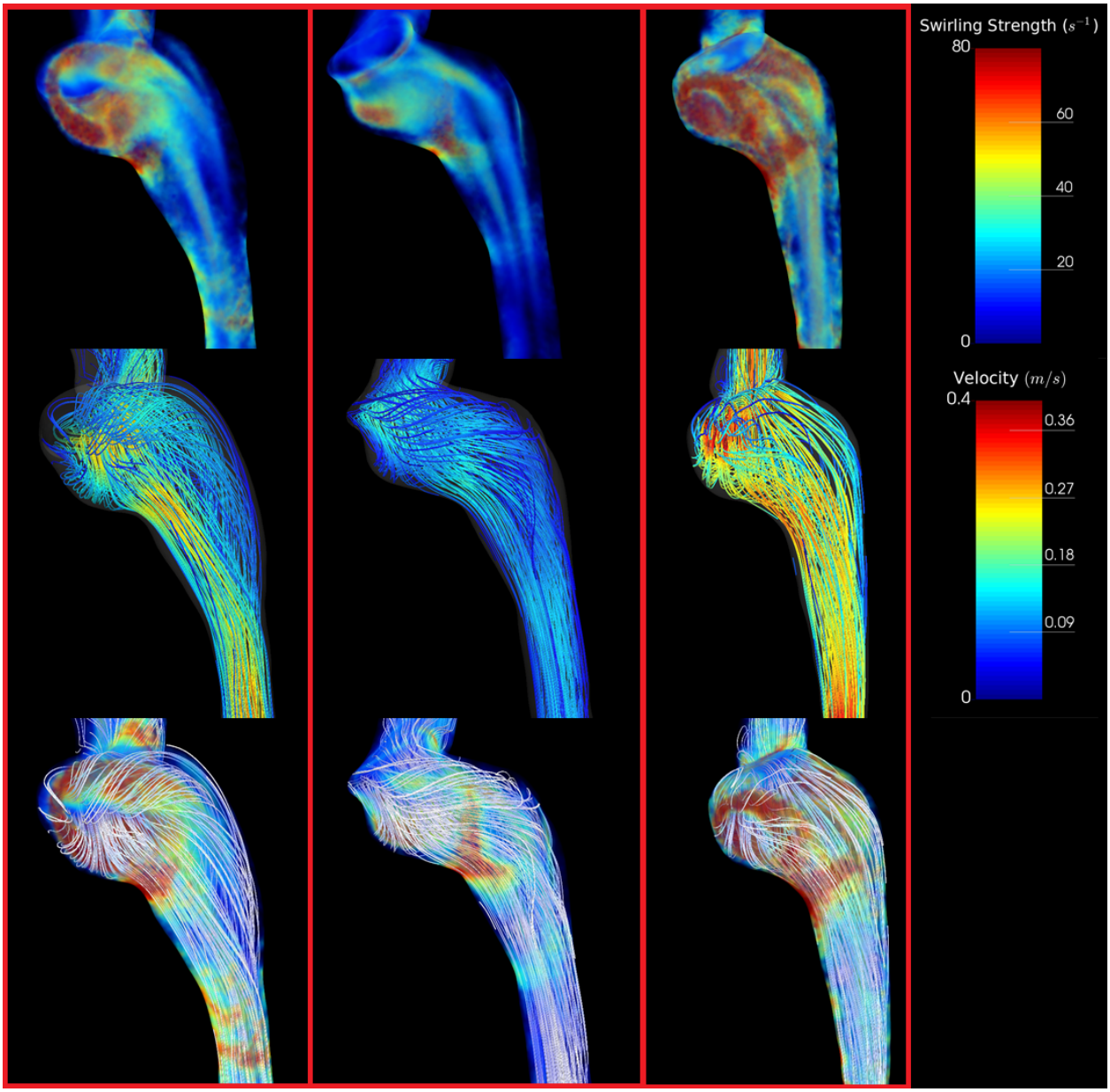

Figure 5.5: Simulation results depicting swirling strength and streamlines for all subjects with rounded jugular bulbs. **Top Row**: Swirling strength distributions throughout the jugular vein representing regions of vortical flow. Note the presence of strong (red) vortex cores in the jugular bulb parallel to flow. **Middle Row**: Streamlines representing the flow field within the jugular vein. Note that most streamlines from the sigmoid sinus fall straight into the internal jugular vein. **Bottom Row**: Streamlines visualized with swirling strength. Streamlines are uncolored to emphasize secondary flow structures.

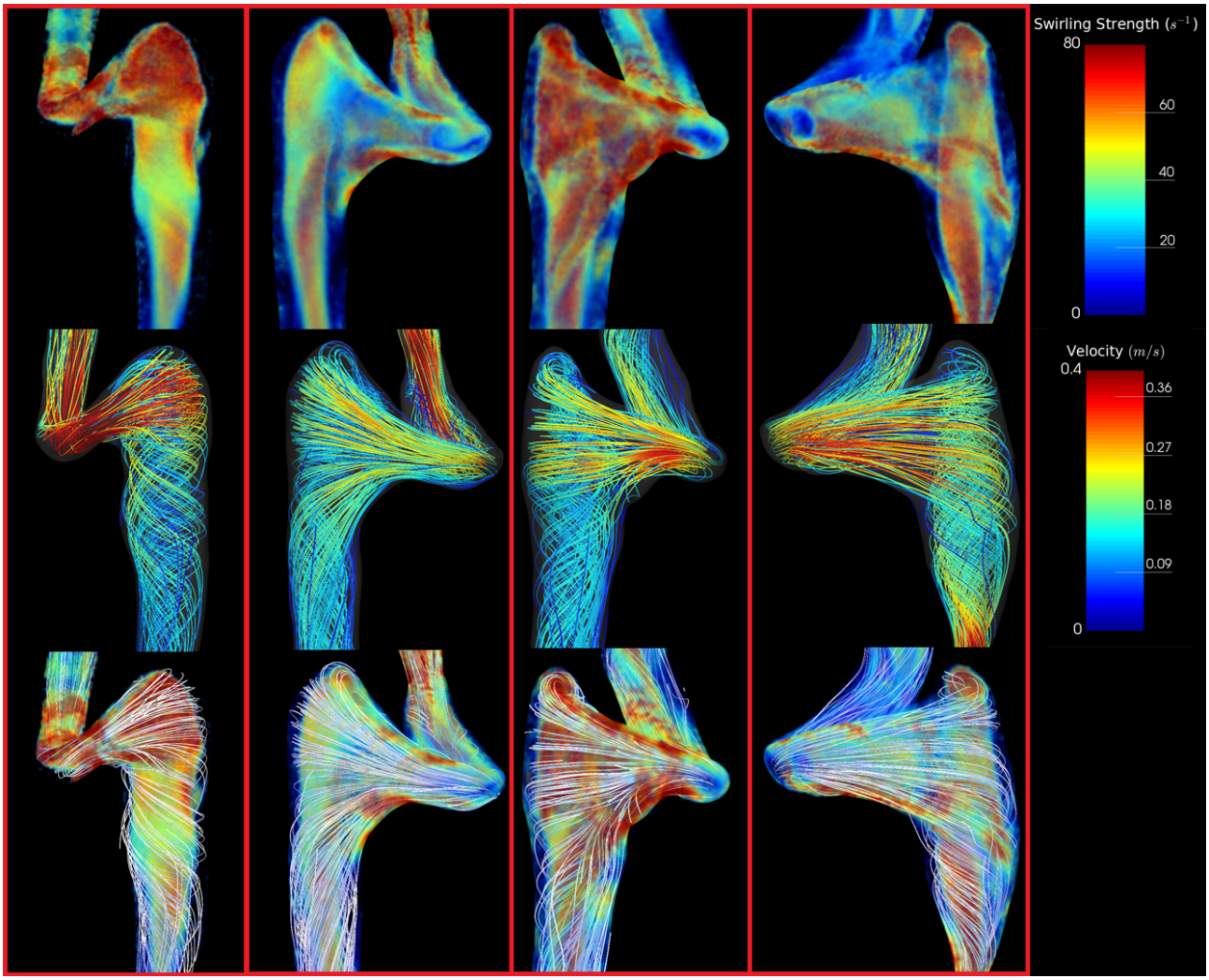

Figure 5.6: Simulation results depicting swirling strength and streamlines for all subjects with elevated jugular bulbs. **Top Row**: Swirling strength distributions throughout the jugular vein representing regions of vortical flow. Note the presence of a large vortex core encompassing the nearly the entire volume of the proximal jugular vein. **Middle Row**: Streamlines representing the flow field within the jugular vein. Note that most streamlines have a significant component that is perpendicular to the direction of flow. **Bottom Row**: Streamlines visualized with swirling strength. Note the outermost streamlines encircling the prominent vortex core.

5.3.2 Quantifying flow patterns by length-averaged streamline curvature

Evaluation of the quantitative metrics of the velocity fields for all subjects with elevated jugular bulb anatomies and for subjects with rounded jugular bulbs also reflected these differences. Inspection of the streamlines and swirling strength distributions reveal that their values are strongly associated with each type of geometry.

The presence or absence of the two flow patterns can be differentiated quantitatively by calculating the length-averaged streamline curvature within the proximal jugular vein, essentially marking the presence (greater curvature) or absence (lesser curvature) of the characteristic helical flow pattern previously described. Figure 5.7 provides the length-averaged streamline curvatures for both types of jugular bulb shapes, while Figure 5.8 depicts the relevant streamlines colored by local streamline curvature for all subjects. Rounded bulbs lead to flows with length-averaged streamline curvatures of $130.3 \pm 8.12m^{-1}$, while elevated bulbs have length-averaged streamline curvatures of $260.7 \pm 29.44m^{-1}$. These values are statistically significant for $P < 0.005$.

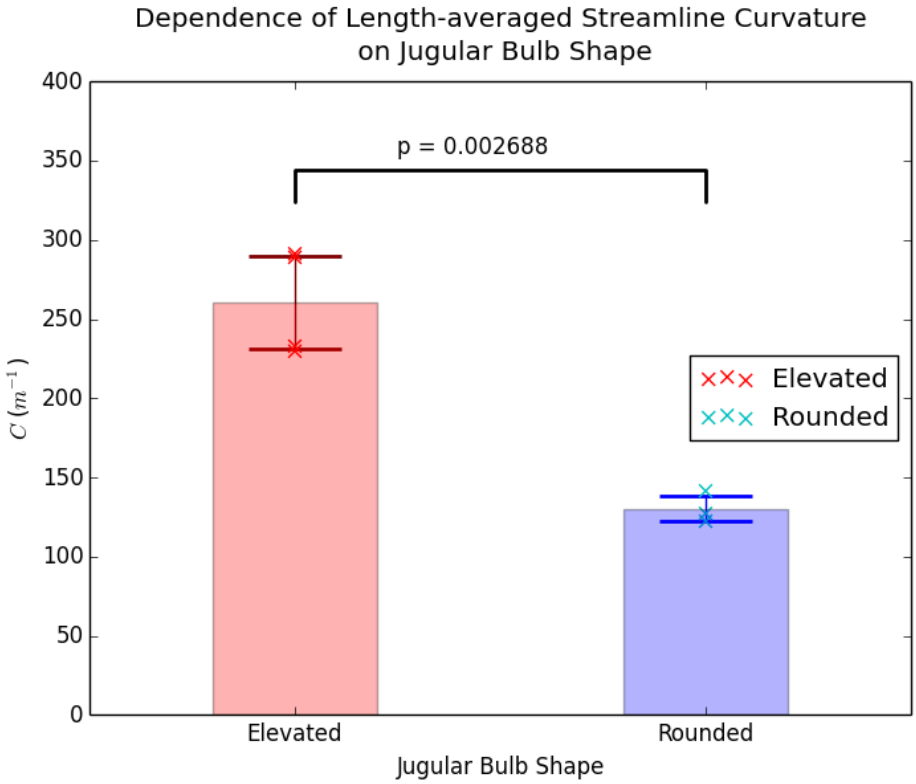

Figure 5.7: Comparison of C for Elevated and Rounded geometries. The cross marks represent values of C for individual subjects, while the transparent bars and associated error bars represent the mean and standard deviation, respectively.

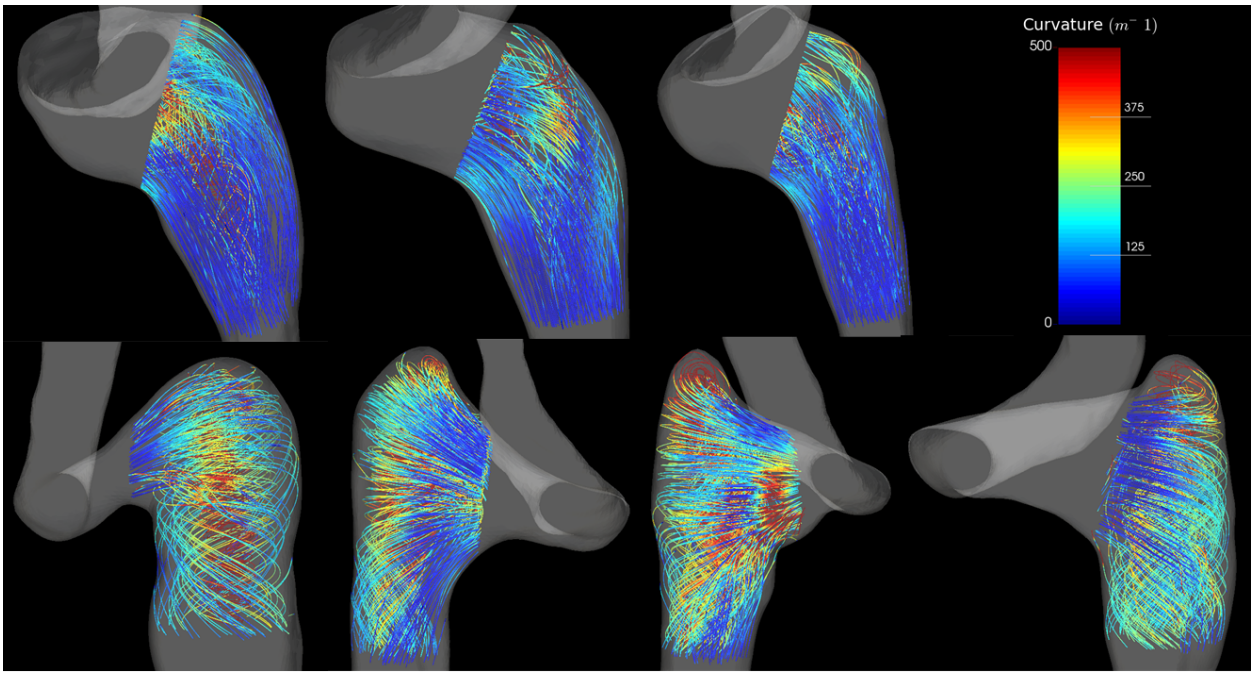

Figure 5.8: Streamlines in the region of interest colored by curvature. **Top Row**: Rounded jugular bulbs. **Bottom Row**: Elevated jugular bulbs.

5.4 Discussion

5.4.1 Image-based velocity field evaluation

This study expands on findings from an in vivo imaging study of the velocity field patterns in the jugular veins of patients with PT [45], but the current work includes a greater number of patients and utilizes CFD. Similar to the work of Acevedo-Bolton and colleagues, we also found the velocity field in patients with PT to be extremely complex with pronounced vortical components. We demonstrate differences in the vortical component of flow between symptomatic and asymptomatic jugular veins that can be both observed and quantified. We hypothesize the vortical component to be critical to sound generation in PT.

The methods outlined by this work are minimally invasive, requiring a small injection of contrast agent during MRI to provide images with sufficient resolution to construct a computational mesh for accurate CFD simulation of important flow features. The approach described here suggests *in vivo* MR imaging can be used across a broad range of venous anatomies and provide the boundary conditions required for detailed CFD analysis of velocity fields on a patient-specific basis.

5.4.2 Pathophysiology of pulsatile tinnitus in the jugular vein

Our study is an exploratory step toward investigating the possible impact of the blood flow velocity field on the pathophysiology of PT thought to originate in the jugular vein. Our results suggest a relationship between geometry, flow, and PT. The differences in flow in the jugular veins of symptomatic and asymptomatic subjects can be distinguished both visually and quantitatively.

High-riding jugular bulb is an established clinical entity that has been proposed to cause PT [50][56][64][65][67]. In our work, symptomatic subjects had a higher incidence of elevated jugular bulb geometries. This study indicates that elevated jugular bulbs can result in a distinct flow pattern that has a large component of vortical flow in the proximal jugular bulb.

Audible bruits are detected in stenotic carotid arteries where downstream vortices shed from turbulent flow are thought to be the source of the flow-induced sound. Similarly, vortical instabilities and pressure fluctuations induced near the lumen wall have been described as the source of audible sound that can be auscultated at the aortic root [63]. While arterial stenoses and the work in [63] explicitly reference unstable flow, the results we present here are for steady flow only. Nevertheless, several

considerations argue that flow in these territories, while generally steady, might have associated unsteady fluctuations, and that the resultant pressure fluctuations would be related to the same geometrical factors that determine the extent of vorticity in the flow that is revealed in our simulations. The high riding bulb anatomy is similar to that of the vortex whistle described by Vonnegut, 1955 [68] and investigated by Chanaud, 1963 [70] (Figure 5.9). Those studies showed that even steady flow in that geometry resulted in a rotating asymmetric vortex that generated a characteristic whistle. Additionally, physiological flow is never perfectly stable, and physiological variability, e.g. breathing and cardiac pulsatility, may perturb total flow and induce pressure fluctuations on the wall. Furthermore, in the elevated bulb anatomy, expansion of the sigmoid sinus into the jugular bulb (with or without a stenotic distal sigmoid sinus segment) would not only result in vortical flow but would likely generate vibrations in the structured flow and pressure fields, particularly in the apex of the bulb. These considerations indicate that the conditions that result in vortical flow will similarly predispose for related instabilities that result in audible sound. These sources of sound remain speculative and identifying acoustic sources is a subject of ongoing study.

Sound generation in the jugular bulb could be amplified by the physiology of the jugular bulb. The jugular bulb is the only portion along the sigmoid sinus and jugular vein that lacks adventitia and it lies near the inner ear space, which contains the cochlea [48]. Raised jugular bulbs are in close apposition to the temporal bone and the middle ear space. The temporal bone is structured for optimal sound transmission, and waves emanating from the jugular bulb could pass directly into the temporal bone and be readily transmitted to the cochlea. The low amplitude of sound waves generated may account for the difficulty examiners have in appreciating venous PT on auscultation.

5.4.3 Limitations

Conclusions are limited by the small sample size. Furthermore, in this initial analysis, we have simplified the distribution of anatomical presentations to either elevated or rounded. While this analysis serves to clearly differentiate velocity patterns between these two presentations, there is a much broader variation found in the general population. Furthermore, subject inclusion into the "elevated" geometry did not require meeting typical definitions of high-riding jugular bulb to the level of the floor of the internal auditory canal [66]. The relationship of pulsatile tinnitus to jugular bulb morphology is likely to be more complex than binary anatomic divisions as we and

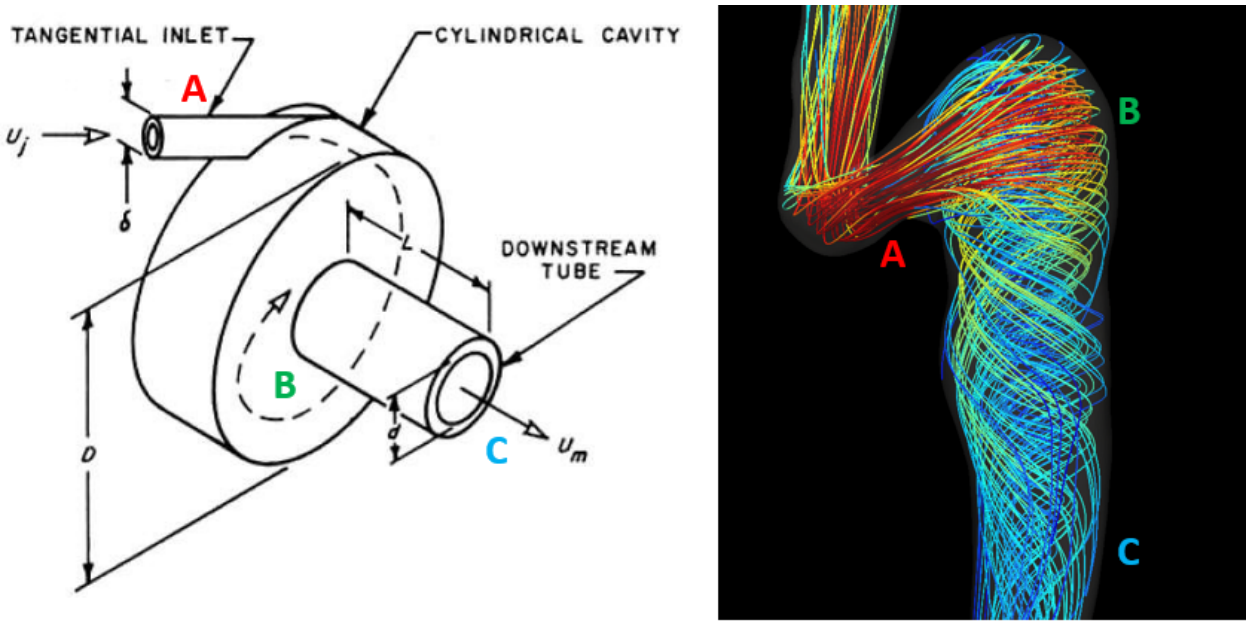

Figure 5.9: Comparison of an elevated jugular bulb geometry (*Right*) to the vortex whistle (*Left*) (adapted from Chanaud 1963, with the permission of the Acoustic Society of America) [70]. The whistle's geometry can be described by three key components: A tangential inlet (A) that introduces flow into a relatively large cylindrical cavity (B), which drains into a smaller cylinder (C). A direct analogy to the elevated bulb can be drawn: The sigmoid sinus narrowing (A) followed by the geometric expansion of the bulb (B) that drains into the distal jugular vein, which is typically much narrower (C).

others have noted.

This study presents a correlation between highly vortical flow and elevated bulb geometry, but does not establish that the vortical flow is directly responsible for PT. The purpose of this study was to investigate whether a relationship exists between jugular bulb anatomy and the presence of a strong vortex component of flow. Further studies are required to determine if the relationship is causal in nature.

The CFD simulations performed here were based on several assumptions. We did not include models of non-laminar flow. Although that is quite reasonable for the large caliber jugular bulb it could fail in stenosed veins. Imposing rigid walls could also affect the flow field. Distension along the sigmoid sinus is limited by the dura, skull, and intracranial pressure. The jugular bulb is often partly surrounded by bone that limits distension. Time resolved cine images from the 2D-MRV data at 0.5 mm in-plane spatial resolution and 40ms temporal resolution revealed no discernable distension of the wall over the cardiac cycle in our region of interest (the SS and proximal IJV). However, *in vivo* imaging does reveal some distension in the cervical jugular vein. One approach to assess the effect of wall motion would be to compare

velocity fields computed by CFD with *in vivo* cardiac cycle time-resolved 4D MR flow measurement, a study we are pursuing at this time.

Another limitation of our study is that we did not consider the effects of patient posture (e.g., lying or standing) on the geometry of the jugular vein, which could be important due to vessel compressibility. However that is partially mitigated in this study, since both subject groups were lying supine during imaging.

5.5 Conclusions

Our study identifies a strong correlation between anatomic morphology of the jugular bulb and resulting flow patterns. Elevated jugular bulbs present with a pronounced vortex. A possible connection between conditions that promote that type of vortical flow and the generation of sound is postulated, but a definitive causal mechanism remains to be established.

Chapter 6

Concluding Remarks

6.1 Summary of Contributions

In this work, we present a pipeline for parallel 4D-MR and CFD analyses of patient imaging data, which together can provide more information than either analysis alone. This pipeline was applied toward the investigation of flow within a cerebral aneurysm phantom and a set of patient cerebral venous outflow tracts.

In Chapter 2, we described our methodology in detail. In-house tools were developed in Python to process 4D-MR flow data. The major steps include image segmentation to mask the data and background correction to minimize the eddy current effects. Flow was measured by taking cross sections of the blood vessel orthogonal to its centerline and numerically integrating the velocity over the area. For CFD simulations, tetrahedral meshes were generated from segmentations of contrast-enhanced MR angiography data. Inflow boundary conditions were based on flow time profiles measured using 2D-MR flow data.

In Chapter 3, we compared flow measurements from 2D-MR, 4D-MR, and CFD in a cerebral aneurysm phantom. In comparing results between 4D-MR and CFD, we found the greatest discrepancies at the vessel wall, where partial voluming effects may severely impact the 4D-flow velocity measurements. We estimated the errors in flow quantification to be about 15%. We applied those errors to CFD simulations by varying the inlet boundary conditions accordingly, and examined their impact on the resultant WSS distributions. We found that aneurysms with a large area of low WSS were less affected by the propagated MR results than those that experienced small or moderately-sized areas of low WSS.

In Chapter 4, we categorized a set of patient CVOT into two major groups:

smooth and irregular geometries. Smooth geometries are mainly characterized by the height of the jugular bulb relative to the sigmoid sinus. They exhibit a helical flow pattern in the internal jugular vein. The degree of helicity correlates with juguar bulb height. Irregular geometries are mainly characterized by sudden geometric abnormalities, mainly diverticula and stenoses. These abnormalities lead to recirculation zones and jets.

In Chapter 5, we took a subset of smooth geometries from patients who exhibited PT and used CFD to quantify their flow patterns. Our results suggested that PT subjects tended to have a elevated jugular bulbs, which resulted in strong helical flow patterns in the internal jugular vein.

6.2 Future Directions

The major sources of error for flow quantification in 4D-MR include positioning effects within the scanner, partial voluming, and scanner calibrations. Future work to improve 4D flow analyses would attempt to reduce the uncertainty from these errors by taking steps to improve reproducibility. Additionally, some techniques have been proposed to account for partial voluming [71].

Our current 4D flow processing workflow uses a rigid segmentation for masking time-dependent data. However, there are many vasculatures in which vessels deform and shift over time. The next step would be to implement time-dependent masks, perhaps by using atlas registration techniques [72].

Chapter 3 examined the effects of MR flow velocimetry errors on WSS distributions. Further work would investigate the effects of geometric or image segmentation errors on simulation results.

In Chapter 5, our conclusions about flow patterns in PT patients were severely limited by our sample size. Additional patient recruitment and simulations are necessary to confirm our results. Potentially, acoustic simulations might be used to investigate how pressure patterns generated on the jugular wall may translate into sound. Furthermore, while we focused on smooth jugular geometries in Chapter 5, future CFD studies may switch focus to sound generation and turbulence in irregular geometries.

Bibliography

[1] Etminan E, Dreier R, Buchholz BA, Beseoglu K, Bruckner P, Matzenauer C, Torner JC, Brown RD, Steiger HJ, Hnggi D, Macdonald RL. Age of Collagen in Intracranial Saccular Aneurysms. Stroke. 45: 1757-1763, 2014

[2] Withers K, Carolan-Rees G, Dale M. Pipeline^{TM} Embolization Device for the Treatment of Complex Intracranial Aneurysms. Applied Health Economics and Health Policy. 11(1): 5-13, 2013.

[3] The UCAS Japan Investigators. The Natural Course of Unruptured Cerebral Aneruysms in a Japanese Cohort. N Engl J Med. 366:2474-2482, 2012.

[4] Villablanca JP, Duckwiler GR, Jahan R, Tateshima S, Martin NA, Frazee J, Gonzalez NR, Sayre J, Vinuela FV. Natural History of Asymptotic Unruptured Cerebral Aneruysms Evaluated at CT Angiography: Growth and Rupture Incidence and Correlation with Epidemiological Risk Factors. Radiology. 269(1): 258-265, 2013.

[5] King JT Jr, Berlin JA, Flamm ES. Morbidity and mortality from elective surgery for asymptomatic, unruptured, intracranial aneurysms: a meta-analysis. J Neurosurg. 81(6): 837-42, 1994.

[6] Raaymakers TW, Rinkel GJ, Limburg M, et al. Mortality and morbidity of surgery for unruptured intracranial aneurysms: a meta-analysis. Stroke. 29(8): 1531-8, 1998.

[7] Solomon RA, Fink ME, Pile-Spellman J. Surgical management of unruptured intracranial aneurysms. J Neurosurg. 80(3):440-6, 1994.

[8] Frydrychowicz A, Winterer JT, Zaitsev M, Jung B, Hennig J, Langer M, et al. Visualization of iliac and proximal femoral artery hemodynamics using timeresolved 3D phase contrast MRI at 3T. J Magn Reson Imaging. 25:1085-92, 2007.

[9] Sigovan M, Hope MD, Dyverfeldt P, Saloner D. Comparison of four-dimensional flow parameters for quantification of flow eccentricity in the ascending aorta. J Magn Reson Imaging. 34:1226-30, 2011.

[10] Bolger AF, Heiberg E, Karlsson M, Wigstrom L, Engvall J, Sigfridsson A, et al. Transit of blood flow through the human left ventricle mapped by cardiovascular magnetic resonance. J Cardiovasc Magn Reson. 9:741-7, 2007.

[11] Stalder AF, Russe MF, Frydrychowicz A, Bock J, Hennig J, Markl M. Quantitative 2D and 3D phase contrast MRI: optimized analysis of blood flow and vessel wall parameters. Magn Reson Med. 60:1218-31, 2008.

[12] Meckel S, Stalder AF, Santini F, Radü E, Rüfenacht DA, Markl M, Wetzel SG. In vivo visualization and analysis of 3-D hemodynamics in cerebral aneurysms with flow-sensitized 4-D MR imaging at 3T. Neuroradiology. 50(6):473-484, 2008.

[13] Isoda H, Ohkura Y, Kosuki T, Hirano M, Takeda H, Hiramatsu H, et al. In vivo hemodynamic analysis of intracranial aneurysms obtained by magnetic resonance fluid dynamics (MRFD) based on time-resolved three-dimensional phase-contrast MRI. Neuroradiology. 52:921-8, 2010.

[14] Zhao X, Zhao M, Amin-Hanjani S, Du X, Ruland S, Charbel FT. Wall Shear Stress in Major Cerebral Arteries as a Function of Age and Gender A Study of 301 Healthy Volunteers. Neuroimaging. 25(3): 403-407, 2014.

[15] Boussel L, Rayz V, Martin A, Acevedo-Bolton G, Lawton MT, Higashida R, Smith WS, Young WL, Saloner D. Phase-Contrast MRI measurements in intracranial aneurysms in-vivo of flow patterns, velocity fields and wall shear stress: A comparison with CFD. Magn Reson Med. 61(2): 409-147, 2009.

[16] Petersson S, Dyverfeldt P, Ebbers T. Assessment of the Accuracy of MRI Wall Shear Stress Estimation Using Numerical Simulations. J Magn Reson Imaging. 36:128-138, 2012.

[17] Markl M, Wegent F, Zech T, Bauer S, Strecker C, Schumacher M, et al. In Vivo Wall Shear Stress Distribution in the Carotid Artery: Effect of Bifurcation Geometry, Internal Carotid Artery Stenosis, and Recanalization Therapy. Circ Cardiovasc Imaging. 3:647-55, 2010.

[18] Dyverfeldt P, Hope MD, Tseng EE, Saloner D. Magnetic Resonance measurement of turbulent kinetic energy for the estimation of irreversible pressure loss in aortic stenosis. JACC Cardiovasc Imaging. 6:64-71, 2013.

[19] Yang GZ, Kilner PJ, Wood NB, Underwood SR, Firmin DN. Computation of flow pressure fields from magnetic resonance velocity mapping. Magn Reson Med. 36:520-6, 1996.

[20] Boussel L, Rayz V, McCulloch C, Martin A, Acevedo-Bolton G, Lawton M, Higashida R, Smith WR, Young WL, Saloner D. Aneurysm Growht Occurs at Region of Low Wall Shear Stress. Stroke. 39: 2997-3002, 2008.

[21] Jou LD, Lee DH, Morsi H, Mawad ME. Wall Shear Stress on Ruptured and Unruptured Intracranial Aneurysms at the Internal Carotid Artery. American Journal of Neuroradiology. 29(9): 1761-1767, 2008.

[22] Castro MA, Putman CM, Sheridan MJ, Cebral JR. Hemodynamic Patterns of Anterior Communicating Artery Aneurysms: A Possible Assocation with Rupture. American Journal of Neuroradiology. 30(2): 297-302, 2009.

[23] Mut F, Lühner R, Chien A, Tateshima S, Viñuela F, Putman C, Cebral JR. Computational hemodynamics framework for the analysis of cerebral aneurysms. Int J Numer Meth Biomed Engng. 27: 822-839, 2011.

[24] Levitt MR, McGah PM, Moon K, Albuquerque FC, McDougall CG, Kalani MYS, Kim LJ, Aliseda A. Computational Modeling of Venous Sinus Stenosis in Idiopathic Intracranial Hypertension. American Journal of Neuroradiology. 37(10): 1876-1882, 2016.

[25] Lotz J, Meier C, Leppert A, Galanski M. Cardiovascular Flow Meaurement with Phase-Contrast MR Imaging: Basic Facts and Implementation. 22(3): 651-671, 2002.

[26] Ebbers T, Haraldsson H, Dyverfeldt P, Sigfridsson A, Warntjes M, Wigström. Higher Order Weighted Least-Squares Phase Offset Correction for Improved Accuracy in Phase-Contrast MRI. ISMRM 16th Annual Scientific Meeting; 2008, May 3-9, Toronto, Ontario, Canada.

[27] Berstein MA, Zhou XJ, Polzin JA, King KF, Gania A, Pelc NJ, Glover GH. Concomitant gradient terms in phase contrast MR: Analysis and correction. Magnetic Resonance in Medicine. 39(2): 300-308, 1998.

[28] Lombaert, H. (2006, March 1). Level set method: Explanation. Retrieved from https://profs.etsmtl.ca/hlombaert/levelset/.

[29] Antica, L. (1999). Patient-Specific Modeling of Geometry and Blood Flow in Large Arteries (Doctoral Dissertation). Retrieved from http://lantiga.github.io/media/AntigaPhDThesis.pdf.

[30] Chong MS, Perry AE, Cantwell BJ. A general classification of three-dimensional flow fields. Physics of Fluids A. 2: 765-777, 1990.

[31] Kefayati S, Amans M, Faraji F, Ballweber M, Kao E, Ahn S, Meisel K, Halbach V, Saloner D. The manifestation of vortical and secondary flow in the cerebral venous outflow tract: An *in vivo* MR velocimetry study. J Biomech. 50: 180-187, 2017.

[32] Khan O, Filippi M, Freedman MS, Barkhof F, Dore-Duffy P, Lassmann H, Trapp B, Bar-Or A, Zak I, Siegel MJ, Lisak R. Chronic cerebrospinal venous insufficiency and multiple sclerosis. Ann Neurol. 67: 286-290, 2010.

[33] Weir B. Multiple sclerosis - a vascular etiology? Can J Neuro Sci. 37: 745-757, 2010.

[34] Mehall CJ, Wilner HI, Larouere MJ. Pulsatile tinnitus associated with a laterally placed sigmoid sinus. Am J Neuroradiol. 16: 905-907, 1995.

[35] Weissman JL, Hirsch BE. Imaging of tinnitus: a review. Radiology. 216: 342-349, 2000.

[36] Satti SR, Leishangthem L, Chaudry MI. Meta-analysis of CSF diversion procedures and dural venous sinus stenting in the setting of medically refractory idiopathic and dural venous sinus stenting in the setting of medically refractory idiopathic intracranial hypertension. Am J Neuroradiol. 36: 1899-1904, 2015.

[37] Starke RM, Wang T, Ding D, Durst CR, Crowley RW, Chalouhi N, Hasan DM, Dumont AS, Jabbour P, Liu KC. Endovascular treatment of venous sinus stenosis in idiopathic intracranial hypertension: complications, neurological outcomes, and radiographic results. Sci World J. 2015, 140408.

[38] Sundstrom P, Wahlin A, Ambarki K, Birgander R, Eklund A, Malm J. Venous and cerebrospinal fluid flow in multiple sclerosis: a case-control study. Ann Neurol. 68: 255-259, 2010.

[39] Durst CR, Ornan DA, Reardon MA, Mehndiratta P, Mukherjee S, Starke RM, Wintermark M, Evans A, Jensen ME, Crowley RW, Gaughen J, Liu KC. Prevalence of dural venous sinus stenosis and hypoplasia in a generalized population. J Neurointerv Surg. dx.doi.org/10.1136/neurintsurg-2015-012147

[40] Wattjes MP, van Oosten BW, de Graaf WL, Seewann A, Bot JCJ, van den Berg R, Uitdehaag BMJ, Polman CH, Barkhof F. No association of abnormal cranial venous drainage with multiple sclerosis: a magnetic resonance venography and flow-quantification study. J Neurol Neurosurg Psychiatry. 82: 29-435, 2011.

[41] Baracchini C, Perini P, Calabrese M, Causin F, Rinaldi F, Gallo P. No evidence of chronic cerebrospinal venous insufficiency at multple sclerosis onset. Ann Neurol. 69: 90-99, 2011.

[42] Zamboni P, Galeotti R, Menegatti E, Malagoni AM, Tacconi G, Dall'Ara S, Bartolomei I, Salvi F. Chronic cerebrospinal venous insufficiency in patients with multiple sclerosis. J Neurol Neurosurg Psychiatry. 80: 392-399, 2009.

[43] Feng W, Ultriainen D, Trifan G, Sethi S, Hubbard D, Haacke EM. Quantitative flow measurements in the internal jugular veins of multiple sclerosis patients using magnetic resonance imaging. Rev Recent Clin Trials. 7: 117-126, 2012.

[44] Kao E, Kefayati S, Amans MR, Faraji F, Ballweber M, Halbach V, Saloner D. Flow patterns in the jugular veins of pulsatile tinnitus patients. J Biomech. 52: 61-67, 2017.

[45] Acevedo-Bolton G, Amans MR, Kefayati S, Halbach V, Saloner D. Four dimensional magnetic resonance velocimetry for complex flow in the jugular vein. Quant Imaging Med Surg. 5(4): 635-7, 2015.

[46] Adler JR, Ropper AH. Self-Audible Venous Bruits and High Jugular Bulbs. Arch Neurol. 43(3): 257-259, 1986.

[47] Bidhult S, Carlsson M, steding-Ehrenborg K, Arheden H, Heiberg E. A new method for vessel segmentation based on a priori input from medical expertise in cine phase-contrast Magnetic Resonance Imaging. In Proceedings of Seventeenth Annual SCMR Scientific Sessions, New Orleans, USA, 2014.

[48] Buckwalter JA, Sasaki CT, Virapongse C, Kier EL, Bauman N. Pulsatile Tinnitus arising from jugular megabulb deformity. Laryngoscope. 93(12): 1534-1539, 1983.

[49] Chandler JR. Diagnosis and cure of venous hum tinnitus. Laryngoscope. 93(7): 892-895, 1983.

[50] Dietz RR, Davis WL, Harnsberger HR, Jacobs JM, Blatter DD. MR imaging and MR angiography in the evaluation of pulsatile tinnitus. AJNR. American journal of neuroradiology. 15(5): 879-89, 1994.

[51] Harvey RS, Hertzano R, Kelman SE, Eisenman DJ. Pulse-synchronous tinnitus and sigmoid sinus wall anamolies: descriptive epidemiology and the idiopathic intracranial hypertension patient population. Otol Neurotol. 35(1): 7-15, 2014.

[52] Jacques D, Nozeret Y, Zdanowicz N, Reynaert C, Garin P, Gilain C. Tinnitus and psychiatric comorbidities in liaison psychiatry analysis of three years in an audiophonology center. Psychiatr Danub. 25 Suppl 2: S102-4, 2013.

[53] Jin L, Wang Y. Management of venous pulsatile tinnitus with normal otoscopic findings. Ear Nose Throat J. 94(9): 386, 388, 390, 392. 2015.

[54] Krishnan A, Mattox DE, Fountain AJ, Hudgins PA. CE arteriography and venography in pulsatile tinnitus: preliminary results. AJNR. American journal of neuroradiology. 27(8): 1635-8, 2006.

[55] Liyanage SH, Singh A, Savundra P, Kalan A. Pulsatile tinnitus. J Laryngol otol. 120(2): 93-7, 2006.

[56] Madani G, Connor SE. Imaging in pulsatile tinnitus. Clin Radiol. 64(3): 319-28, 2009.

[57] Markl M, Frydrychowicz A, Kozerke S, Hope M, Wieben O. 4D flow MRI. J Magn Reson Imaging. 36: 1015, 2012.

[58] Marsot-Dupuch K. Pulsatile and non-pulsatile tinnitus: a systemic approach. Seminars in Ultrasound, CT and MRI. 22(3): 250-270, 2001.

[59] Mattox DE, Hudgins P. Algorithm for evaluation of pulsatile tinnitus. Acta Otolaryngol. 128(4): 427-31, 2008.

[60] Nayak KS, Nielsen JF, Bernstein MA, Markl M, Botnar RM, Gatehouse PD, Saloner D, Lorenz C, Wen H, Hu BS, Epstein FH, Oshinski JN, Raman SV. Cardiovascular magnetic resonance phase contrast imaging. J Cardiovasc Magn Reson. 17:71, 2015.

[61] Park JJH, Shen A, Loberg C, Westhofen M. The relationship between jugular bulb position and jugular bulb related inner ear dehiscience: a retrospective analysis. Am J Otolaryngol. 36(3): 347-351, 2015.

[62] Pridmore S, Walter G, Friedland P. Tinnitus and suicide: recent cases on the public record give cause for reconsideration. Otolaryngol Head Neck Surg. 147(2): 193-5, 2012.

[63] Seo JH, Vedula V, Abraham T, Mittal R. Multiphysics computational models for cardiac flow and virtual cardiography. Int. J. Numer. Meth. Biomed. Enging. 29(8): 850-869, 2013.

[64] Sismanis A. Pulsatile Tinnitus. Otolaryngol Clin North Am. 36(2): 389-402, viii, 2003.

[65] Sonmez G, Basekim CC, Ozturk E, Gungor A, Kizilkaya E. Imaging of pulsatile tinniuts: a review of 74 patients. Clinical Imaging. 31(2): 102-108, 2007.

[66] Vachata P, Petrovicky P, Sames M. An anatomical and radiological study of the high jugular bulb on high-resolution CT scans and alcohol-fixed skulls of adults. J Chin Neurosci. 17(4): 473-478, 2010.

[67] Vattoth S, Shah R, Curé JK. A compartment-based approach for the imaging evaluation of tinnitus. AJNR. American journal of neuroradiology. 31(2): 211-8, 2010.

[68] Vonnegut, B. The Vortex Whistle. Jo Acost Soc Am. 26: 16-20, 1955.

[69] The Vascular Modeling Toolkit. Retrieved May 2, 2016 from www.vmtk.org.

[70] Chanaud RC. Experiments concerning the Vortex Whistle. The Journal of the Acoustic Society of America. 35: 953-960, 1963. doi: http://dx.doi.org/10.1121/1.1918639

[71] Tang C, Blatter DD, Parker DL. Correction of partial-volume effects in phase-contrast flow measurements. J Magn Reson Imaging. 5: 175180, 1995. doi:10.1002/jmri.1880050212

[72] Bustamante M, Petersson S, Eriksson J, Alehagen U, Dyverfeldt P, Carhall C-J, Ebbers T. Atlas-based analysis of 4D flow CMR: Automated vessel segmentation and flow quantification. Journal of Cardiovascular Magnetic Resonance. 17:87, 2015. doi: 10.1186/s12968-015-0190-5